NTNU

Norwegian University of
Science and Technology

First-Principles Calculations of Oxygen Vacancy Formation in Epitaxially Strained $La_{1-x}Ca_xMnO_3$

Rasmus Vester Thøgersen

Preface

This Master's thesis was carried out at the Department of Materials Science and Engineering at the Norwegian University of Science and Technology during Spring 2016. It is part of the author's Master of Science degree in nanotechnology for materials, energy and the environment. The reader is expected to have prior knowledge of basic concepts within solid state physics and quantum mechanics.

All calculations have been done within plane-wave density functional theory as implemented in VASP [1, 2, 3, 4]. The calculations have been carried out on the computer cluster Abel located at the University of Oslo. All visualization of crystal structures has been done in VESTA [5].

Trondheim, 15.06.2016

Rasmus Vester Thøgersen

Acknowledgment

I would like to extend my appreciation towards my supervisor, associate professor Sverre Magnus Selbach, for guidance during the duration of my thesis work. The project has proven to be both interesting and challenging, and has been accordingly rewarding. My co-supervisor, Ph.D. candidate Astrid Marthinsen, whose door has always stayed open, and with whom I've had several fruitful discussions with along the way, also deserves a big thanks. The weekly meetings in the ferroelectrics group have provided a useful arena for feedback, and the members of the DFT group have always been helpful when computational challenges has arisen.

I would like to thank my brother, Mikkel Vester Thøgersen, for taking time from his busy family life, and to my roommate Marte Orderud Skare, for help with the proofreading of my thesis and finding the mistakes that I've grown blind to.

Lastly, I'd like to thank all classmates in the graduating class of 2016 of the nanotechnology study program, with whom I have had the pleasure of spending the last five years.

R.V.T.

I stand at the seashore, alone, and start to think.

There are the rushing waves

mountains of molecules

each stupidly minding its own business

trillions apart

yet forming white surf in unison.

RICHARD P. FEYNMAN

Abstract

Using epitaxial strain as a degree of freedom is a promising way to tailor the properties in thin films of transition metal oxides. Since the ground state of such materials tend to have many competing low-energy states they are susceptible to small perturbations, potentially inducing new phenomena. Due to the choice of different substrates and growth orientations, a wide range of strain can be applied in the thin films, giving researchers the ability to fine-tune the material properties.

In this work, the effect of epitaxial strain on the oxygen vacancy formation energies in different compositions of $La_{1-x}Ca_xMnO_3$ is calculated from first-principles within the DFT + U framework using the PBEsol functional. Due to the different spatial orientation of the Mn-O-bonds, it is possible to distinguish between two chemically inequivalent oxygen anions with a differing reponse to biaxial strain. This difference is reflected in the oxygen vacancy formation energies, which for all composition exhibit a different strain response.

A displacement of oxygen anions towards the La/Ca-cations was found. For the intermediate compounds, the formation energies are largely influenced by which cation the oxygen is displaced towards. In combination with the reported phenomenon of surface segregation of cations, this could potentially be utilized in creating oxygen vacancy concentration gradients for use in novel electronics design.

Sammendrag

Å bruke epitaksiell tøyning som en frihetsgrad er en lovende strategi for å skreddersy egenskaper i tynnfilmer av transisjonsmetalloksider. Fordi grunntilstanden i slike materialer som regel har flere konkurrerende lavenergitilstander, er de lett påvirket av små perturbasjoner, som potensielt kan lede til nye fenomener. På grunn av mulighetene i valg av ulike substrat og orientering av vekst, kan man indusere et vidt spekter av tøyning, som gir forskere muligheten til å finjustere materialegenskapene.

I dette arbeidet blir effekten av epitaksiell tøyning på dannelsesenergien til oksygenvakanser i ulike komposisjoner av $La_{1-x}Ca_xMnO_3$ regnet ut fra grunnprinsipper i et DFT + U-rammeverk ved bruk av PBEsol-funksjonalet. På grunn av ulik romlig orientering av Mn-O-bindingene, er det mulig å skille mellom to kjemisk inekvivalente oksygenanioner med ulik respons på biaksiell tøyning. Denne forskjellen er reflektert i dannelsesenergien til oksygenvakansene, som for alle komposisjoner utviste en ulik respons til tøyning.

En forskyvning av oksygenanionene mot La/Ca-kationene ble funnet. For intermediære komposisjoner er vakansenergiene i stor grad påvirket av hvilket kation oksygenanionet er forskjøvet mot. Sammen med det rapporterte fenomenet av overflatesegregering av kationer, kan dette potensielt bli utnyttet til å lage konsentrasjonsgradienter av oksygenvakanser for bruk i design av ny elektronikk.

Contents

Chapter 1

Introduction

Strain engineering is a promising way for materials scientists to fine-tune the material properties. When thin films of a material is grown epitaxially on an underlying substrate, strain is induced at the growth interface due to a mismatch between the thin film and substrate lattice parameters. By varying the type of substrate or the growth orientation, the strain can be tuned across a wide range of strains ranging from compressive to tensile. One class of materials that is especially interesting for strain engineering, are the transition metal oxides. In these materials there is a strong electron correlation, where each valence electron influences the behavior of every other valence electron. Due to this, there is a plethora of low lying energy states, which means these materials are very susceptible to small, external perturbations, and in some cases even new phenomena can arise [6]. By studying and gaining control of the strain induced effects, strain engineering could potentially become a very powerful tool in tailoring useful material properties to be used across many different fields of research and industries.

One family of transition metal oxides are the mixed-valence manganites, such as $La_{1-x}Ca_xMnO_3$. These materials have been the topic of much research since studies began in the 1950s with the seminal papers on doped $LaMnO_3$ by van Santen and Jonker [7, 8], and especially since the discovery of the colossal magnetoresistance effect (CMR)[1] in the 1990s [9], the research has intensified. These materials exhibit rich phase diagrams as a function of dopant concentration, x, owing to a delicate competition between the orbital, spin and lattice degrees of freedom, making them very interesting from a fundamental physics point of view. For intermediate ranges of x, $La_{1-x}Ca_xMnO_3$ exhibits a ferromagnetic metallic domain in which it behaves as a half-metal which only conduct electrons of one spin polarization, opening up the possibility for use in spin injection devices in spintronics [10].

In the transition metal oxides, the defect profile is also very important [11]. Oxygen vacancies are for instance known to be essential for superconductivity in high-temperature superconductors [12, 13] and for enabling ionic conductivity in cathodes in solid oxide fuel cells [14] and oxygen gas sensors [15]. Reports of strain-induced vacancy ordering promises that the defect profiles can be controlled using epitaxial strain [16].

The effects of strain are however not so easy to isolate in experiments in the lab. Since the substrate has another chemical composition than the thin film, there are also chemical effects involved at the interface, and there could also be differences in structure that impose changes in the thin film. In addition, one must

---

[1]Colossal magnetoresistance is an effect where a colossal change in resistivity is induced by an external magnetic field.

also devise a way to probe the desired properties, which is not always that easy. Theoretical quantum chemistry studies is one way to isolate these effects, and techniques such as density functional theory (DFT) have become increasingly popular as a complementary tool in the materials scientist's toolbox. With increasing computational power, the use of such methods will probably continue to become an even more essential part of materials science in the decades to come.

1.1   Aim of work

In this work, DFT is applied to calculate oxygen vacancy formation energies in four compositions of $La_{1-x}Ca_xMnO_3$ (x = 0, 0.125, 0.25, 0.375) under epitaxial strain in the (001)-plane from first-principles. Calculations are first performed on the bulk phase of the compositions, before strain is applied on the stoichiometric cells. The oxygen deficient cells are then simulated in order to calculate the formation energies. The work is inspired by earlier work by Aschauer *et al.* [16], who performed similar calculations on the parent compound $CaMnO_3$ (x = 1). In his work, it was found that strain affected the formation energies of inequivalent oxygen anions differently, which leads to the prediction of vacancy ordering in strained films.

These calculations require a rigorously tested model system in order to provide accurate results. A part of this project has thus been to test and tweak computational parameters, and making sure the chosen parameters give well-converged results.

1.2   Thesis organization

The underlying theory is presented in chapters 2, 3 and 4. In chapter 2 the materials system, $La_{1-x}Ca_xMnO_3$, is presented, in chapter 3 the concept of strain engineering and defect chemistry is treated, while a theoretical introduction to DFT is given in chapter 4 along with a discussion of practical considerations when doing such simulations. In chapter 5 the computational details are given, and results from convergence testing is shown and discussed. The methods of simulation are also elaborated here. In chapter 6 the results are presented, and a discussion of trends and other findings is given in chapter 7, along with suggestions for further work. Chapter 8 summarizes and concludes the work.

There are two appendices. Appendix A is a short list of abbreviations used in the thesis, and can be used for reference by the reader. Appendix B is a collection of input files used in the calculations.

Chapter 2

Calcium-Doped Lanthanum Manganite

Compounds of the type $R_{1-x}A_x MnO_3$, where R is a trivalent rare earth metal and A is a divalent alkali earth metal, have been a topic of research since the 1950s, when Jonker and van Santen first reported different magnetic and conductive properties of doped $LaMnO_3$ (LMO) compared to its parent compounds [7]. Later work showed that these compounds exhibited a multitude of different magnetic phases, and phenomena such as charge ordering, orbital ordering, and metal-insulator transitions. An especially interesting property is the colossal magnetoresistance effect (CMR), that occurs at the metal-insulator transitions, where there is a dramatic increase in the resistivity under the influence of an external magnetic field.

These materials, due to the complex interplay of interactions, provide an exciting playground to explore new physics, and achieve a better understanding of the solid state at the nanoscale. These materials are also promising candidates in some future energy applications [14], and also in the design of novel spintronics [10].

2.1   Mixed-valence manganites

The interest in the mixed-valence manganites started with papers by Jonker and Van Santen from 1950 [7]. In this work, the insulating LMO was doped with divalent alkali earth metals (Ca^{2+}, Sr^{2+} and Ba^{2+}). This causes the oxidation of one of the Mn^{3+}-ions to Mn^{4+}, hence the name mixed-valence manganites. These compounds were found to exhibit a ferromagnetic ordering of spins of the Mn-electrons. Later work also found that this phase showed high values of conductivity [7]. This was curious, as both parent compounds exhibited insulating and antiferromagnetic properties. In work by Zener, the simultaneous ferromagnetism and conductivity was explained by a mechanism coined double exchange [17, 18]. This mechanism involves the simultaneous hopping of an electron from a Mn^{3+} to a Mn^{4+}, through an oxygen ion, and ensures both a ferromagnetic exchange between the two Mn-ions and a transfer of the electron (see section 2.2.1). In later work by Volger in 1954, the first signs of a magnetoresistive effect was found, when he showed that the resistance of Sr-doped LMO (LSMO) decreased upon application of a magnetic field [19].

In 1955 an extensive neutron diffraction study by Wollan and Kohler revealed a multitude of different magnetic phases that depends on the relative tetra- and trivalent manganese ion content [20]. Simultaneously, a theoretical elucidation of the results by Goodenough was published, where the existence of these phases was described by a theory of semicovalence between the manganese cations and oxygen anions [21].

Interest in these materials resurged in the 1990s when a giant magnetoresistance-

effect (GMR) of ~60% was discovered in thin films of Ba-doped LMO in 1993 by von Helmholt *et al.* [22] and Chahara *et al.* [23]. A year later, a change in resistivity of more than three orders of magnitude, coined colossal magnetoresistance (CMR) to distinguish it from GMR, was discovered by Jin *et al.* [9], which really renewed the interest in these materials. This magnetoresistive effect was intrinsic to the material, and not the result of a heterostructure, such as the devices used to read magnetic storage media, and could potentially be used in next generation read-out heads. However, the large magnitude of the magnetic field necessary to induce this effect (several teslas) has so far made them impractical for such applications.

However, the interest in understanding the nature of the CMR-effect persists, and much remains to be understood of the underlying physics governing the material. The interplay between these effects make this class of materials very complex, and also very interesting for fundamental solid state physics.

2.2 The La$_{1-x}$Ca$_x$MnO$_3$-system

The compound dealt with in this work, is Ca-doped LMO (LCMO). The parent compounds, LMO and CaMnO$_3$ (CMO) both crystallize as the mineral perovskite, with orthorhombic (*Pnma*) symmetry (figure 2.1). Both are antiferromagnetic insulators, but exhibit different types of antiferromagnetic ordering. LMO has A-type antiferromagnetic ordering (A-AFM), where the Mn^{3+} ions are coupled ferromagnetically in planes, and antiferromagnetically between planes. CMO has G-type antiferromagnetic ordering (G-AFM), where all nearest neigh-
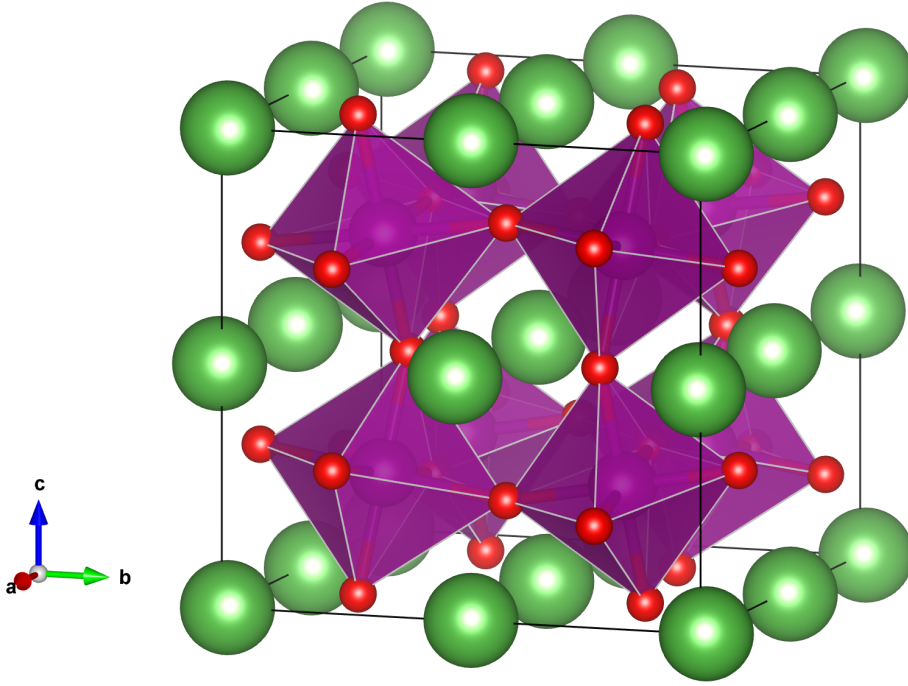
Figure 2.1: The pseudocubic 2x2x2 unit cell of $LaMnO_3$. Color codes: green (La), purple (Mn), red (O).

bors of each Mn^{4+}-ion has opposite spin. Upon doping LMO, divalent Ca^{2+} takes the place of the trivalent La^{3+}, resulting in an oxidation of the Mn^{3+}. This gives solutions with the formula $La_{1-x}Ca_xMn^{3+}_{1-x}Mn^{4+}_xO_3$, where x is the fraction of Ca. It forms a solid solution for all compositions [7].

The free $3d$-orbitals of Mn have a five-fold degeneracy, but when surrounded by six oxygen anions, such as in the octahedral configuration seen in figure 2.1, the five orbitals exhibit an energy splitting due to the crystal field effects of the surrounding anions. Some orbitals point directly at the oxygen anions, and experience a higher Coulomb repulsion, while others are oriented away from the oxygen anions. This leads to three lower lying energy states, termed t_{2g}-states, and two higher lying states, termed e_g. For the Mn^{3+}-ions, which has a d^4-electron configuration, three of the d-electrons are placed in each of the lower
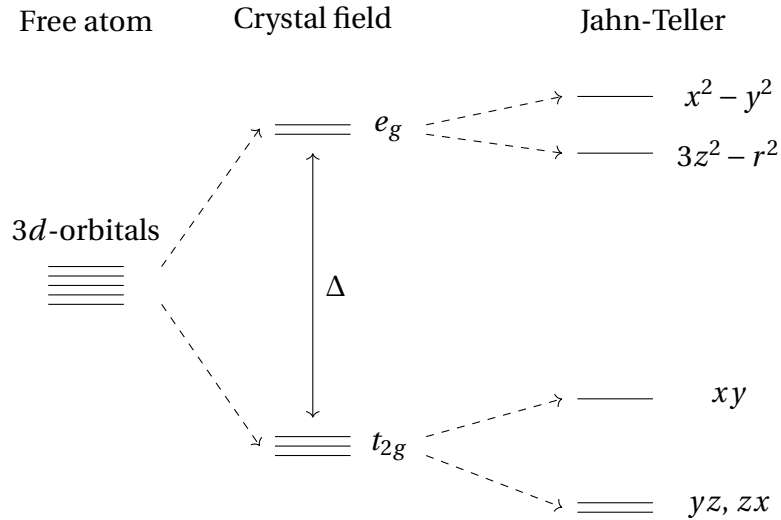
Figure 2.2: A schematic view of the splitting of the 3d-orbital energy levels. First the splitting due to the crystal field, separated by the crystal field splitting energy Δ, followed by the splitting due to the Jahn-Teller effect, where the orbital degeneracy of the e_g-orbital is lifted to accommodate one electron at an energetic gain.

lying t_{2g}-orbitals, according to the Aufbau principle. Due to strong Hund's exchange, there is a tendency towards a high-spin configuration, so that the last electron goes into the higher lying e_g-orbitals instead of filling the other spin states of the t_{2g}-orbitals. Since the e_g-orbitals are doubly degenerate, an energetic gain can be obtained by splitting the energy level, as only the lower lying level will be filled. This is known as the Jahn-Teller-effect [24] and is realized by a distortion of the octahedron. The energy splitting is drawn schematically in figure 2.2. This effect is said to be cooperative because distortion in one octahedra affects neighboring octahedra, which is obvious as each oxygen anion in the octahedron is also part of a neighboring octahedron.

The phase diagram of LCMO is very rich, and is shown in figure 2.3, taken from Dagotto *et al.* [25] who reproduced it from Cheong and Hwang [26]. Moving towards more Ca-content from the purely antiferromagnetic parent compound

LMO, a canted antiferromagnetic phase (CAFM) is found where the spins are aligned antiferromagnetically, but slightly canted to give a net magnetic moment. Moving towards more Ca-content, for $0.075 < x < 0.175$, a ferromagnetic insulating phase (FM-I) is found, a phase that also exhibits charge ordering with a peak at $x = 1/8$. The existence of the CAFM and FM-I phases has been disputed, and it is rather believed that these compositions exhibit a phase separation of antiferromagnetic (AFM) and FM phases [25]. This is further discussed in section 2.2.2. At around $x = 0.175$, a metal-insulator transition is found, and the material exhibits metallicity with FM ordering, with a peak in Curie-temperature (T_C) at $x = 3/8$. At $x = 4/8$, another metal-insulator transition is found, and the magnetic ordering changes to a complex hybrid CE-type AFM ordering. This region also exhibits charge ordering that peaks at $x = 5/8$. Another CAFM phase (or phase separated AFM and FM phases) occurs at $x = 7/8$, and G-type AFM ordering is found at $x = 1$. Above the Curie- and Néel-temperatures, the compounds are paramagnetic insulators (PM-I) for all values of x.

2.2.1 Double exchange and semicovalence

Early models to explain the rich phase diagram of LCMO were presented by Zener and Goodenough in the 1950s [17, 18, 21]. Zener first explained the simultaneous ferromagnetic coupling between adjacent Mn-ions by a mechanism he coined double exchange. It involves the actual simultaneous transfer of an electron from an Mn^{3+}-ion to an oxygen anion, and an electron from the oxygen anion to the Mn^{4+}-ion, hence the name. This is not to be confused with the
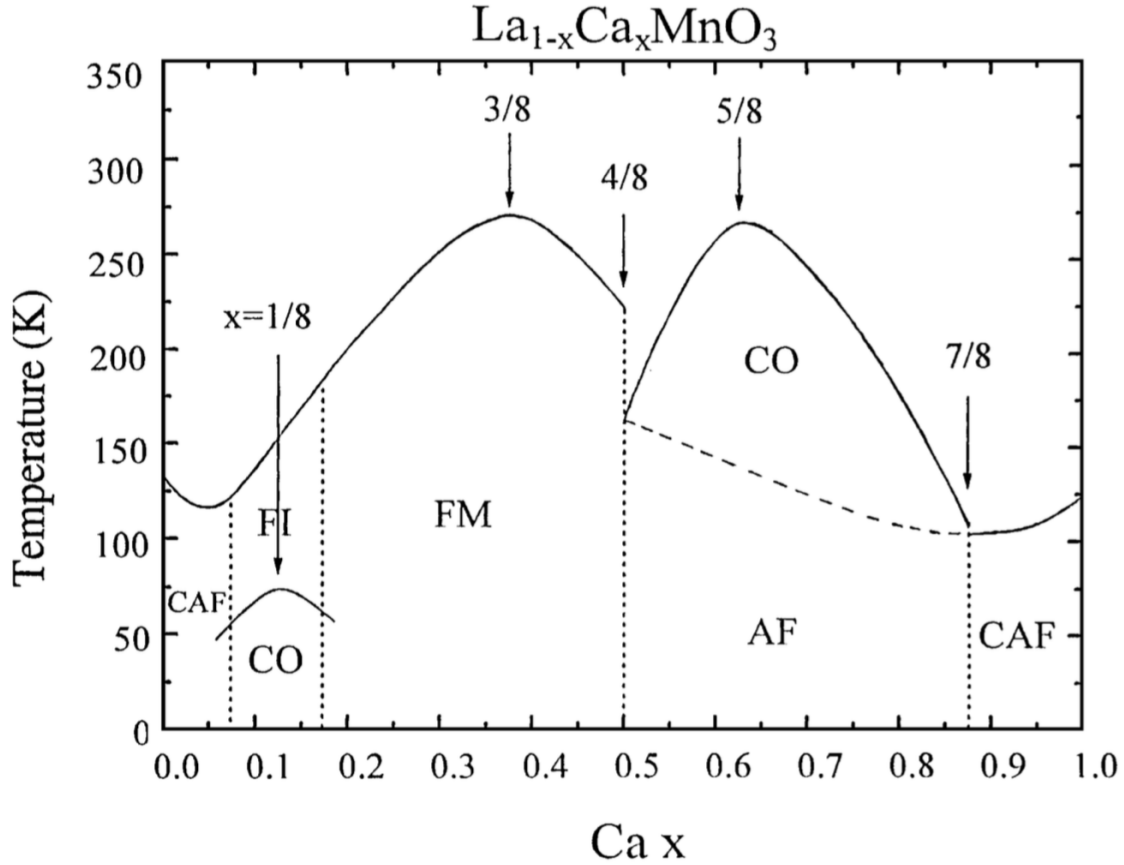
Figure 2.3: Phase diagram of La$_{1-x}$Ca$_x$MnO$_3$ as a function of Ca-content. FM: ferromagnetic metal, FI: ferromagnetic insulator, CO: charge ordering, CAF: canted antiferromagnetic, AF: antiferromagnetic. Figure taken from Dagotto *et al.*[25], who reproduced it from Cheong and Hwang[26].

similar (and usually antiferromagnetic) superexchange mechanism, where the indirect exchange involves no actual electron transfer [27]. Two Mn-ions of different valence bridged by an oxygen anion makes up a degenerate state that can be written

$$\psi_1 : \text{Mn}^{3+} - \text{O}^{2-} - \text{Mn}^{4+} \qquad\qquad \psi_2 : \text{Mn}^{4+} - \text{O}^{2-} - \text{Mn}^{3+}. \qquad (2.1)$$

The electron in the e_g-orbital of the Mn^{3+} is transferred to the O $2p$-orbital, but
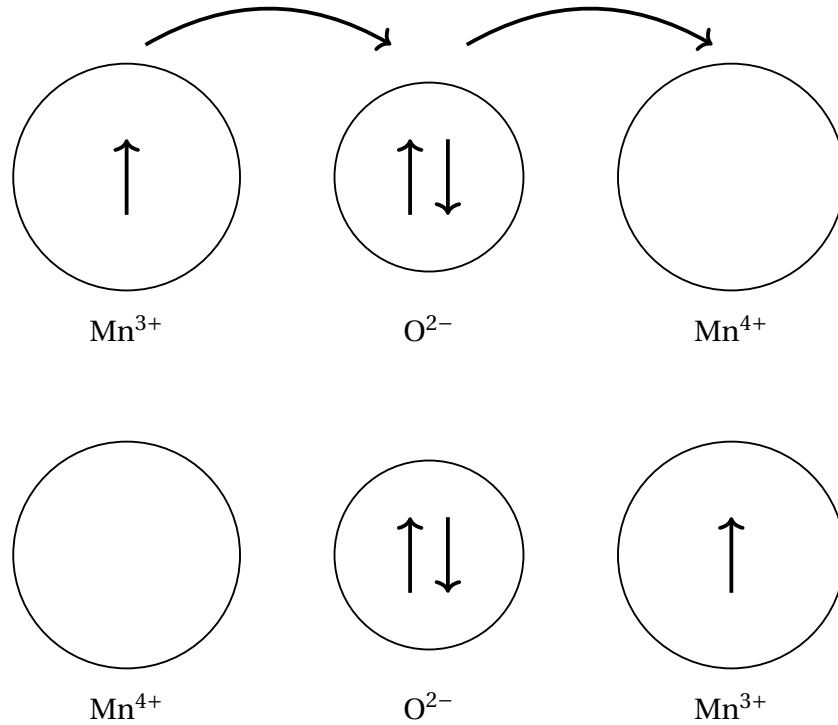
Figure 2.4: Schematic view of the double exchange mechanism. An e_g-electron from Mn^{3+} is transferred to the $2p$-orbital of the intermediate O^{2-}, at the same time that an electron of the same spin is transferred from the $2p$-orbital to the empty e_g-orbital of the Mn^{4+}-ion.

since this orbital already has this state filled, the electron of the same spin in the $2p$-orbital is simultaneously transferred to the empty e_g-orbital of the adjacent Mn^{4+}-ion. Since a large Hund's exchange ensures the intraorbital ferromagnetic coupling in the Mn^{3+}-ion, and the electron transferred from the oxygen $2p$-orbital must have the same spin as the electron being transferred to the $2p$-orbital, the spins in the accepting Mn^{4+}-ion must also be oriented the same way, which ensures ferromagnetic coupling between the Mn-ions. This is drawn schematically in figure 2.4.

This theory was further developed by Anderson and Hasegawa [28]. In their work, they related the effective hopping integral to the angle between the classical spins ($t \propto \cos(\theta/2)$). This can be related to the Mn-O-Mn-bond angles, and

a larger deviation from the ideal 180°-angle essentially means that the double exchange-mechanism is weaker. This can also be seen as the reduced overlap of the 2p-orbitals with the Mn e_g-orbitals as the bond angle deviates from the ideal linear case. An O 2p-orbital can't have full overlap with one of the Mn e_g-orbitals at the same time as the other, if there is an angle between the two bonds. This underlines the importance of the Goldschmidt tolerance factor, which is a measure of how much a structure deviates from the ideal perovskite structure, and depends on the relative sizes of the A- and B-cations [29]. It is defined as

$$t = \frac{r_A + r_O}{\sqrt{2}(r_B + r_O)}, \tag{2.2}$$

where r_A, r_B and r_O denotes the radii of the A, B and O-ions respectively. In general, if a perovskite has a lower tolerance factor than 1, due to the A-cation being too small, the symmetry is expected to go from an ideal cubic symmetry with linear Mn-O-Mn-bonds, to rhombohedral or orthorhombic symmetry, where the BO$_6$-octahedra are tilted. The larger deviation from the ideal perovskite structure, the larger tilt can be expected, and this decreases the double exchange hopping integral.

In 1955, John B. Goodenough published his work on semicovalence, and this theory was able to rationalize much of the findings of Wollan and Kohler [21]. The theory described the semi-covalent nature of the Mn-O-bonds, and is based on an assumption that the empty orbitals in Mn^{3+} hybridizes in square planar dsp^2-lattice orbitals, and the orbitals in Mn^{4+} hybridizes empty octahedral d^2sp^3-lattice orbitals, which point towards all oxygen anions in the octa-

hedral configuration. These hybridized orbitals give rise to three different types of bonding between the Mn-cations and oxygen: the semicovalent case where an empty Mn-orbital points towards a $2p$-orbital, which exhibits the shortest bond distance, the case where empty dsp^2-orbitals points away from the oxygen, which exhibits the longest bond distance and is also the least stable, and a metallic-like bond due to a lattice of disordered Mn^{3+} and Mn^{4+}, explained by double exchange. The degeneracy in equation 2.1 is lifted if there is a charge ordering of Mn^{3+} and Mn^{4+}, and in this case double exchange disappears.

The different configurations of the Mn-O-Mn-bonds yield the different magnetic coupling between the Mn-ions, shown in figure 2.5. In the case where both bonds are semi-covalent, the $2p$-electrons will spend most of the time close to the cations. Due to Hund's exchange, the electrons will prefer to be in the vicinity of a Mn-ion with a parallel spin. This leads to an antiferromagnetic coupling between the two Mn-ions.

In the case where one of the bonds is semicovalently bonded, and the other is ionically bonded, there once again is a ferromagnetic coupling between the electron participating in the semicovalent bond and the Mn-ion. The electron not participating in this semi-covalent bond will be antiparallel to the Mn-ion, and more localized on the oxygen anion, such that a net magnetic moment is associated with the oxygen. There is a direct exchange between the oxygen anion and the ionically bonded cation, such that there is an antiferromagnetic coupling. This results in a net ferromagnetic coupling between the two cations.

These types of coupling can be used to describe the magnetic ordering of sev-

a) Antiferromagnetic

Mn^{4+} or Mn^{3+} O^{2-} Mn^{4+} or Mn^{3+}

b) Ferromagnetic

Mn^{4+} or Mn^{3+} O^{2-} Mn^{3+}
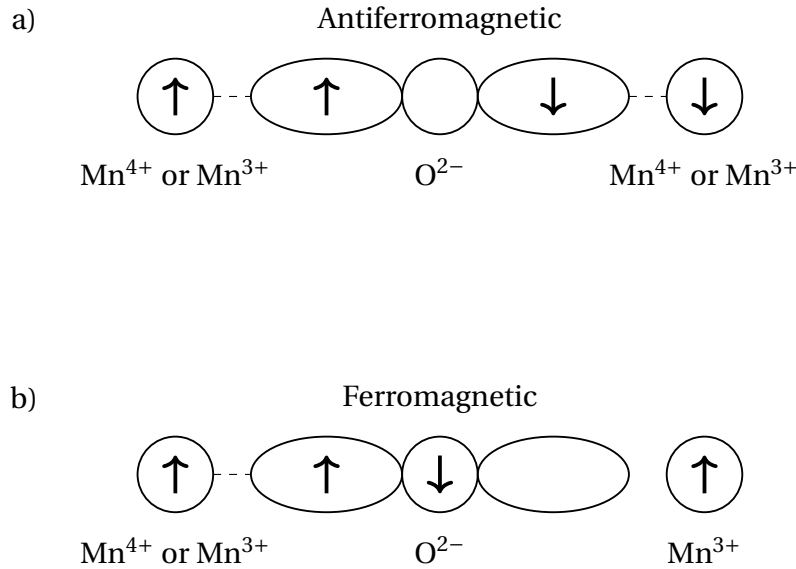
Figure 2.5: A schematic view of the different types of Mn-O-Mn-bonds. Dashed lines indicate semicovalent bonding, no line indicate ionic bonding. a) Semicovalent bonding between O $2p$-orbitals and empty lattice orbitals of Mn^{4+} or Mn^{3+} pointing towards the oxygen on both sides of the oxygen. This results in an antiferromagnetic coupling between the cations. b) Only semi-covalent bonding on one of the sides, and ionic on the other. This results in a net ferromagnetic coupling.

eral of the compositions. For pure CMO, all Mn-ions are Mn^{4+}, and there is anti-ferromagnetic bonding between all cations, resulting in G-AFM (see figure 2.6). For pure LMO, only four of the six Mn-O-bonds per octahedron can bond cova-lently. These bonds will order in such a way to reduce the elastic strain arising from the different bond lengths. The most stable configuration is seen to be one where all O^{2-} are bonded with at least one covalent bond in such a way that all bonds in the (001)-plane corresponds to figure 2.5b, and all the bonds between the (001)-planes correspond to figure 2.5, resulting in A-AFM. Goodenough fur-ther argues that the Mn^{4+}-ions are randomly distributed in the compositions $0.25 < x < 0.375$, and calculates the concentration of Mn^{4+} for the maximum T_C and lowest resistivity to be $x \approx 0.31$. The compositions $0.1 < x < 0.25$, he argues, must be two-phase, consisting of both A-AFM and FM. Lastly he argues that for
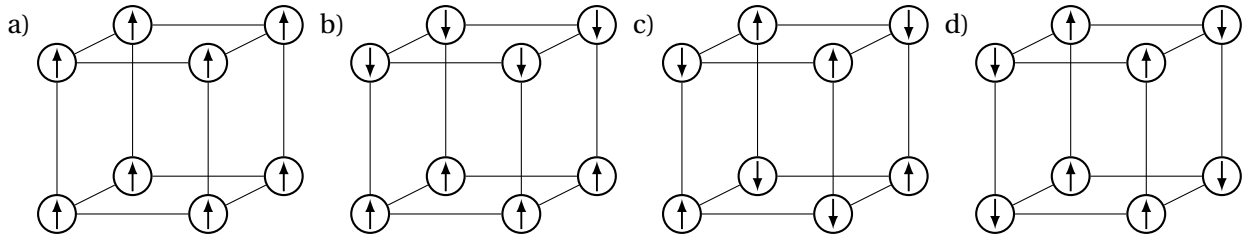
Figure 2.6: The a) ferromagnetic (FM), b) A-type antiferromagnetic (A-AFM), c) G-type antiferromagnetic (G-AFM) and d) C-type antiferromagnetic (C-AFM) ordering of the Mn $3d$-spins.

the composition $x = 0.5$, the configuration must be a hybrid CE-configuration, which consists of alternating C- and E-type AFM ordering.

While double exchange and semicovalence provide good explanations for some of the physics in the mixed-valence manganites, these models do not provide the full picture. For instance, using double exchange only, the calculations of T_C is wrong, and Goodenough predicted that the maximum value of T_C should be at $x \approx 0.31$ based on the theory of semicovalence, while it has been measured to be at higher values of x. In order to explain phenomena such as metal-insulator transitions and the CMR-effect, extensions to the theory must be made, and small polarons[1] have for instance been introduced in an attempt to explain some of the physics that the aforementioned models have been unable to explain. For the purpose of this work, the double exchange and theory of semicovalence are sufficient in order to rationalize the magnetic ordering and the mechanism of conduction. For more information on the underlying physics, the reader is referred to extensive reviews by Ramirez *et al.* [30], Rao *et al.* [31], Coey *et al.* [32], Salamon *et al.* [33], Dagotto *et al.* [25] and Tokura *et al.*[34].

---

[1]A small polaron is a quasiparticle consisting of a localized electron and the lattice distortion associated with it, that can move from site to site by thermally activating hopping.

2.2.2 Inhomogeneous phases in manganites

Another topic of importance with regards to mixed-valence manganites is the role of phase separation. As mentioned above, the nature of the canted anti-ferromagnetic phases ($0 < x < 0.075$, $0.875 < x < 1.00$) and the ferromagnetic insulating phase ($0.075 < x < 0.175$) has been disputed, and evidence of phase separation has accumulated over the last two decades [25]. First, such a separation is already predicted by the theory of semicovalence, where coexisting A-AFM- and FM-phases are predicted in the $0.1 < x < 0.25$ interval. In the review by Dagotto, a detailed analysis of theoretical work is presented that predicts the formation of nanoscale phases due to the competing effects, as well as a review of the experimental evidence for such separation, even in the ferromagnetic metallic region ($0.175 < x < 0.5$), as seen in a scanning tunneling spectroscopy-study by Fäth *et al.* [35]. In the framework of phase separation, the metal-insulator transition can be seen as a percolative effect, occurring at a percolation threshold where FM domains form a continuous network through the material. There are still things that remain unclear regarding the phase separation in manganites [36].

Chapter 3

Strain Engineering And The Role Of Defect Chemistry

The transition metal oxides form an interesting group of materials, as they exhibit a wide range of interactions that are of similar magnitude, and thus form several competing low energy phases in addition to the ground state phase. This large interplay is attributed to the strong electron correlation of the transition metal d-electrons and the nature of the metal-oxygen bond. This points to the idea that small, controlled perturbations can influence the properties of the materials, and detailed knowledge of how this influence manifests itself could give materials scientists a way to tailor properties to a specific application. This is also true for the manganites, where the plethora of different competing phases due to the lattice, orbital, charge and spin degrees of freedom make them susceptible to external perturbations.

As there has been much progress in making high-quality oxide thin films the last decades, gaining control over the small perturbations of these materials

$a > a'$ = tensile strain
$a < a'$ = compressive strain

Epitaxial growth
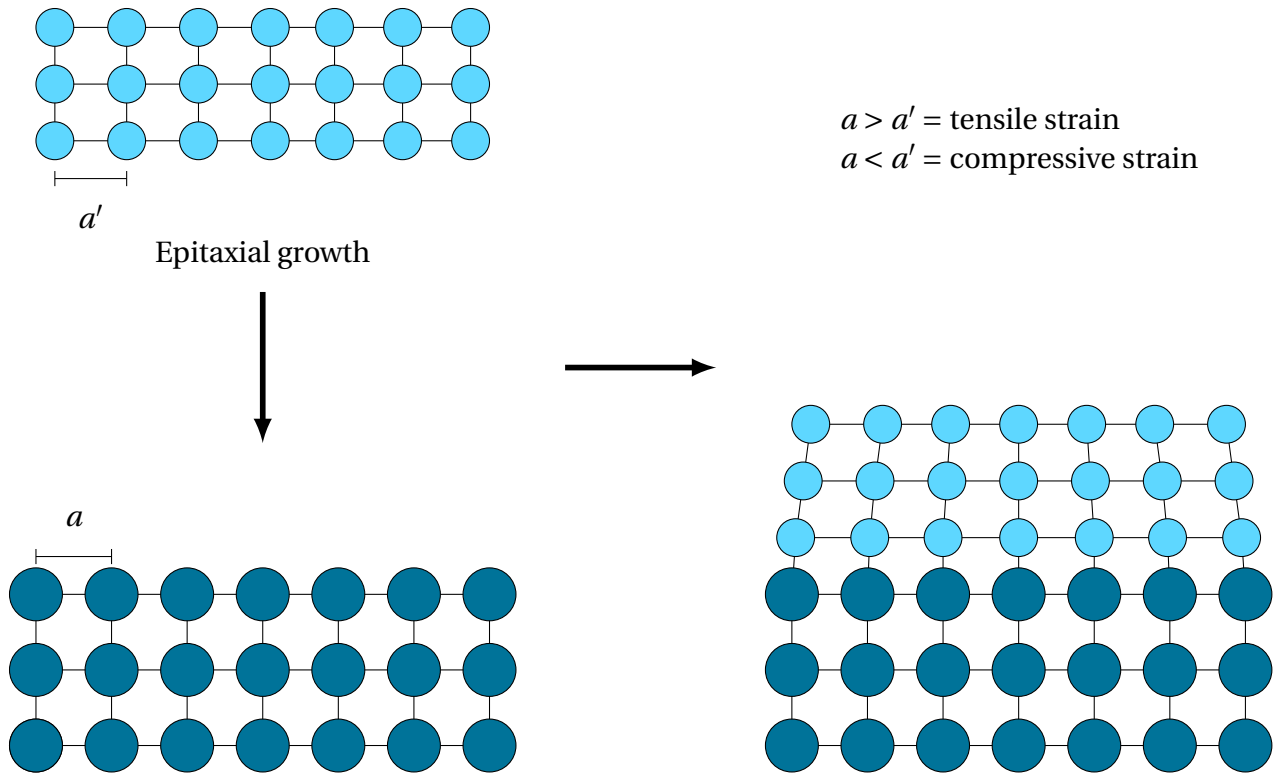
Figure 3.1: Schematic view of a material where there is a mismatch between the lattice parameters. The lattice parameter a' of the top material is smaller than the lattice parameter a of the substrate, and tensile strain is induced at the interface. This strain is relaxed further up in the thin film. In the case where $a' > a$, there is a compressive strain induced.

promises many novel functionalities.

3.1   Strain engineering

One way to tune the properties of these transition metal oxides, is to vary the degree of strain it is subjected to under growth. Thin films that are grown epitaxially, will be subjected to strain at the growth interface due to a lattice mismatch between its bulk structure and the lattice of the underlying substrate (see figure 3.1). By varying the substrate material, or the orientation of the growth, the amount of strain can be tuned across a wide range of both compressive and

tensile strain. Since there are so many low energy states, imposing strain may change which state is the energetically most favorable, and the properties can then be tuned.

It can be hard to experimentally determine the role strain has on the properties, as growing a material heteroepitaxially[1] introduces other chemical effects in addition to strain. First-principles calculations have been useful in doing this however, as it is then possible to exclude the chemical effects of the substrate, and also tune the strain precisely across all possible values of strain. Gaining a thorough understanding of what happens when strain is introduced can open up a powerful way to tailor material properties to specific applications.

3.1.1 Strain accommodation in perovskite oxides

There are several ways that perovskite oxide thin films, such as LCMO, can accommodate the elastic strain induced from the underlying substrate. This is summarized in figure 3.2. One way is the change in internal bond lengths. When the material is subjected to biaxial compressive strain, the bond lengths perpendicular to the strained plane will increase, and for biaxial tensile strain, the opposite is true. Together with the change in the perpendicular axis, the tilting of the BO_6-octahedra can also change in order to accommodate the strain: for compressive strain and increasing length of c-parameter, the octahedral tilt (β) decreases, and for tensile strain the tilting increases. The opposite is true for the in-plane rotation (α) of the BO_6-octahedra.

---

[1]Heteroepitaxy is the epitaxial growth of one compound onto another of different chemical composition.
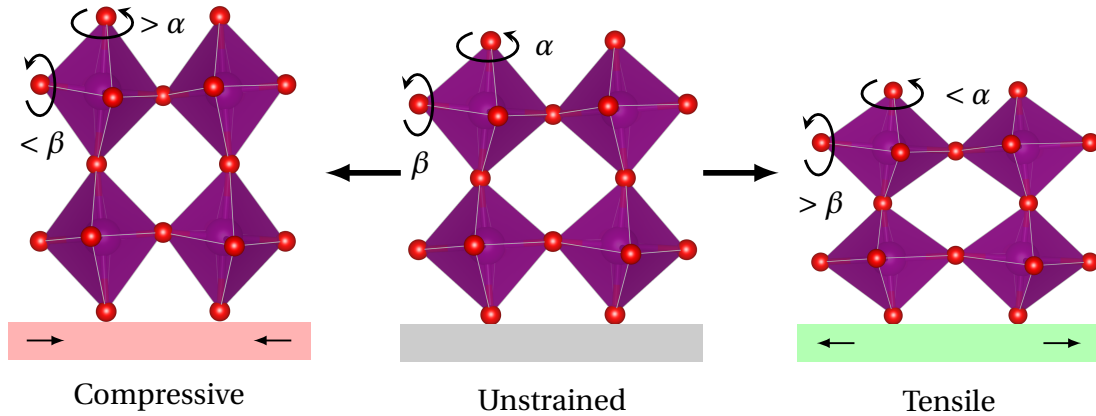
Figure 3.2: A summary of typical strain accommodation in perovskite oxides. The first to notice is the elongation (shortening) of the out-of-plane c-lattice parameter for compressive (tensile) strain. This is accommodated by longer (shorter) bond lengths along this direction, and shorter (longer) bond lengths in the strained plane. Also associated with strain accommodation is the rotation and tilting of the BO_6-octahedra. The angle α denotes the rotation of the BO_6-octahedra in the strained ab-plane, while β denotes the rotation in the ac and bc-planes, or conversely the tilting of the octahedra along the c-direction. With compressive (tensile) strain, α increases (decreases) and β decreases (increases). Based on figure in Aschauer *et al.* [16]

In this work, the octahedral tilt is defined as the average deviation from the ideal $180°$ Mn-O-Mn-bond angles along the c-axis. The octahedral rotation is defined as the average rotation of the Mn-O-bonds in the ab-plane w.r.t. a lattice vector in the same plane.

Poisson's ratio

A value associated with strain is Poisson's ratio, defined for biaxial strain as

$$\nu = \frac{1}{1 - 2\varepsilon_{xx}/\varepsilon_{yy}}, \tag{3.1}$$

where ε_{xx} denotes the strain in the x-direction (or along the a-lattice vector) and $\varepsilon_{xx} = \varepsilon_{yy}$. ε_{yy} is the strain in the y-direction (or along the b-lattice vector). Poisson's ratio has an ideal value of 0.5, where the unit cell volume is kept constant

under strain. Most materials however, have values ranging from 0.2-0.4 [37]. A value lower than 0.5 indicates that there is a volume increase associated with tensile strain and a volume decrease associated with compressive strain.

3.1.2 Effects of strain in $La_{1-x}Ca_xMnO_3$

There have been many studies of epitaxial strain in LCMO, and its effect on the magnetic and transport properties. A common substrate to induce tensile strain in LCMO is $SrTiO_3$ (STO) which induces ~1% tensile biaxial strain. For compressive strain, $LaAlO_3$ (LAO) is commonly used, which results in ~2% compressive biaxial strain, and $NdGaO_3$ (NGO) is commonly used as a reference structure, inducing only ~0.1 % compressive strain.

There has been reports that tensile strain destabilizes the ferromagnetic coupling for compounds $x = 0.33$ [38, 39]. This destabilization is attributed by the authors to a strain induced orbital ordering, but an increase in octahedral tilt could also destabilize the double exchange-mechanism.

Other researchers argue that the destabilization instead is an inherent effect of thin film thickness, and not strain [40].

3.2 Defect chemistry

A material never forms a perfect crystal. The crystal structure deviates from perfect crystallinity by containing point defects, such as vacancies, interstitials and substitutions, or line defects such as screw dislocations.

Such defects are very important for the material properties, and many exciting physical phenomena in materials, such as high-temperature superconduction, can be directly related to the defect chemistry of the material [12, 13].

3.2.1 Functional defects in transition metal oxides

The importance of defect chemistry on material properties are well known from the field of semiconductor physics, but the defect profile of transition metal oxides is perhaps even more important for the material properties [41, 11]. For cuprates that exhibit high-temperature superconductivity the effects of point defects are essential, and oxygen vacancies are important for enabling ionic conductivity in cathodes used for solid oxide fuel cells [14], conducting membranes [42] or oxygen sensors [15]. They also play an important part in the emergence of multiferrocity in certain materials [43].

As discussed in chapter 2, the introduction of substitutional defects can also have profound effects on the magnetic and transport properties of a material, giving rise to different magnetic orderings and changing the transport properties drastically.

The more these effects are understood and controlled, the more sophisticated devices can be designed enabling the era of ionotronics.

3.2.2 Oxygen stoichiometry in La$_{1-x}$Ca$_x$MnO$_3$

The oxygen stoichiometry is not always ideal in oxides, and there can be a tendency towards an under- or overstoichiometry of oxygen. This is the case for LCMO, shown in a study by Rørmark *et al.* [44]. In this work, a series of solid solutions were prepared for which the oxygen stoichiometry was measured. The oxygen stoichiometry as a function of Ca-content at different temperatures from this study is given in figure 3.3. Pure LMO is seen to have a large oxygen excess, or rather cation deficiency, while pure CMO was found to be fairly oxygen deficient under growth conditions in an O$_2$-atmosphere. This means that the oxygen vacancies are readily formed for CMO, while they are not as readily formed in LMO. In other words, higher oxygen vacancy formation energies are expected for LMO than for CMO. In CMO, earlier work by Rørmark *et al.* determined the vacancy formation enthalpy to be 1.89 ± 0.04 eV [45], which was fairly well reproduced with first-principles calculations by Aschauer *et al.* [16] LMO on the other hand has reported formation values of 4.29 ± 0.66 eV calculated from defect-disorder models based on experimental non-stoichiometry data [46], which indeed is considerably higher than CMO.

The oxygen vacancies leaves behind two electrons when formed. In the insulating LMO, the extra electrons would be localized on two Mn^{3+} reducing them to Mn^{2+}, while for the conducting LCMO 0.25 and LCMO 0.375, the electrons could also be delocalized and smeared out over all the Mn^{3+}-ions. In Kröger-Vink notation, oxygen vacancy formation in LMO can be written
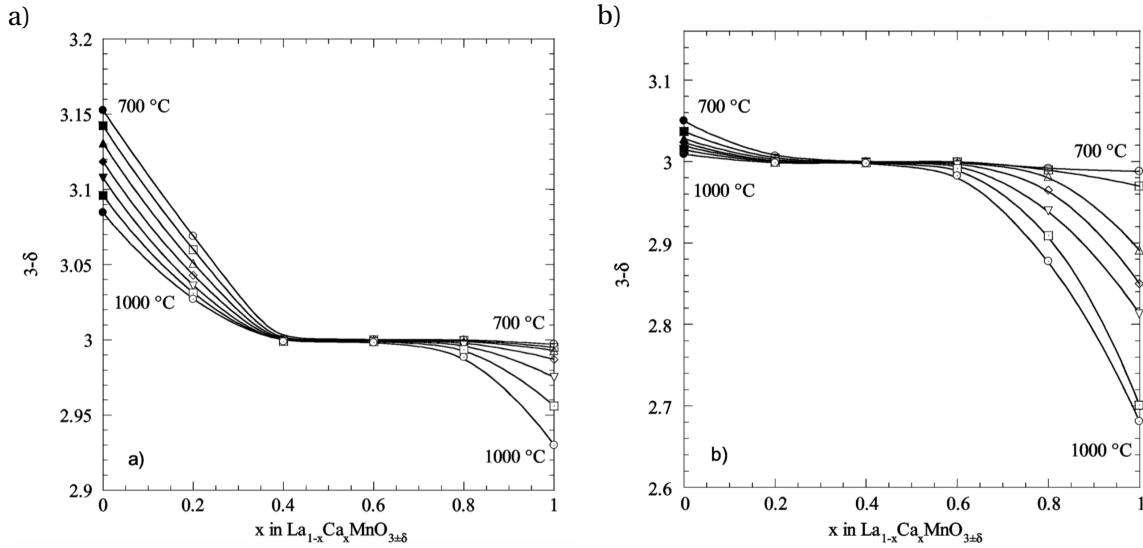
Figure 3.3: Oxygen stoichiometry as a function of Ca-content at temperatures ranging from 700°C - 1000°C in a) air and b) N_2-atomsphere. Plots taken from Rørmark *et al.* [44]

$$2Mn_{Mn}^{\times} + O_O^{\times} \longleftrightarrow 2Mn_{Mn}' + V_O^{\bullet\bullet} + \frac{1}{2}O_2, \tag{3.2}$$
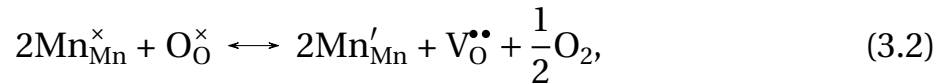
where $Mn_{Mn}^{\times}$ is a Mn^{3+} on a Mn^{3+} site, $O_O^{\times}$ is an O on an O-site, Mn_{Mn}' is an Mn^{2+} on an Mn^{3+}-site.

3.2.3   Vacancy ordering

In work by Aschauer *et al.* [16], a strain dependence was found for the oxygen vacancy formation enthalpies in $CaMnO_3$. A strain dependence was expected, since the oxygen vacancies are associated with a chemical expansion due to the two electrons from the oxygen anion left in non-bonding orbitals [47]. Since tensile strain leads to an increase in unit cell volume, an increase in oxygen vacancy concentration could be used as a means to accommodate the strain instead.

It was also found that the oxygen vacancy formation enthalpies of inequivalent oxygens were different, depending on whether the broken Mn-O-Mn-bonds lie in the strained plane, or out of it. The in-plane oxygen vacancies were found to be more stabilized than the out-of-plane oxygen vacancies with tensile strain, which lead to very different equilibrium vacancy concentrations for the two different vacancy types, inducing vacancy ordering.

Chapter 4

Density Functional Theory

Ever since its conception in the 1960s by Walter Kohn and co-workers, density functional theory (DFT) has become increasingly used by researchers as a workhorse across several research fields. Especially in the last couple of decades, much due to the rapid increase in computational power and further developments of the method, it is a now an essential part of modern materials science, and goes hand-in-hand with experimental work in investigations into nanoscopic phenomena and properties. DFT allows researchers to isolate and directly explore effects that experimentalists are unable to probe, and can give valuable insights and elucidate experimental findings. Together with experimental verifications in the lab, DFT has been important and will continue to be even more so in the future as the process power available to researchers increase.

This chapter seeks to explain the underlying theory of DFT, how this is applied to the solid state and how this is applied in practice.

4.1   The Schrödinger equation

First published by Erwin Schrödinger in 1926, the Schrödinger equation describes the quantum state of a quantum system as it changes over time [48]. In its most general form, it is written

$$\hat{E}\Psi(\vec{r}, t) = \hat{\mathscr{H}}\Psi(\vec{r}, t), \tag{4.1}$$

where $\hat{E} = i\hbar\frac{\partial}{\partial t}$ is the energy operator, $\Psi(\vec{r}, t)$ is the wavefunction of the quantum system and $\hat{\mathscr{H}}$ is the Hamiltonian operator. The Hamiltonian describes the kinetic and potential energy terms of the system, and is tailored to fit the system under scrutiny. For a single non-relativistic particle moving in some potential field, the Hamiltonian would contain one term for the kinetic energy associated with the movement of the particle, and one spatially and temporal dependent term for the potential field. This is the time-dependent Schrödinger equation, but for systems where the Hamiltonian has no temporal dependence, the time-independent Schrödinger equation is used,

$$E\psi(\vec{r}) = \hat{\mathscr{H}}\psi(\vec{r}). \tag{4.2}$$

This is an eigenvalue problem, which means that for every stationary state $\psi(\vec{r})$, there only exists a solution for certain values of the energy, E.

In principle equation 4.1 can be applied to any system given a suitable Hamiltonian. In practice it is not quite as simple[1]. There are only a few systems that

---

[1]According to the Nobel lecture given by Walter Kohn [49] after he received the 1998 Nobel Prize in Chemistry for

allow an analytical solution, such as the the particle-in-a-box or the hydrogen atom. Complications arise when more than one electron is introduced to the system. In addition to a kinetic energy term and an electron-nuclei potential term, there also is a electron-electron repulsion term arising from the Coulombic interaction between these particles. This interaction causes the electron movements to be correlated, and the resulting wavefunction becomes incredibly complicated. This is a case of a many-body problem, which doesn't allow an analytical solution, and thus requires numerical approaches to be solvable. The sheer complexity of the problem also requires certain approximations to be made, in order to make the calculations practically feasible. Among the methods used to do this are the so-called post-Hartree-Fock-methods and perturbation theory, but this text will deal only with DFT.

4.2 The Hohenberg-Kohn theorems

In 1964, Pierre Hohenberg and Walter Kohn formulated two theorems known as the Hohenberg-Kohn theorems [50]. They are, as formulated by Sholl and Steckel [51]:

1. The ground state energy from the Schrödinger equation is a unique functional[2] of the electron density.

2. The electron density that minimizes the energy of the overall functional is

---

his development of density functional theory, the famous physicist Paul A.M. Dirac, with whom Erwin Schrödinger shared his 1933 Nobel Prize in Physics, supposedly said shortly after the publication of the Schrödinger equation: "Chemistry has come to an end. Everything there is to know is contained within this one equation. Too bad, that in almost all cases it is far too complex to allow solution"

[2]A functional is a mathematical concept that describes a function that instead of a number takes another function as its argument. A typical example of a functional is an integral, $F[f(x)] = \int f(x) \mathrm{d}x$.

the true electron density corresponding to the full solution of the Schrödinger equation.

The first theorem means that one can map the ground state electron density to the ground state wavefunction, and that the system is uniquely described by this electron density. The remarkable with this theorem, is that it essentially proves that the problem is reduced from the $3N$-dimensional space of the wavefunction to the 3-dimensional space of the electron density without losing any information. While the theorem proves that such a functional of the electron density exists, it says nothing about how one can obtain it.

The second theorem gives us a way to find the ground state electron density. It says that if we have the exact functional, we can apply a variational method where the electron density is varied until an energy minimum is found.

The Born-Oppenheimer approximation assumes that since the electrostatic forces acting on the electrons must be of similar magnitude to the forces acting on the nuclei, and since the nuclei are much more massive than the electrons, the motions of the electrons are much more rapid than that of the ions [52]. The electrons can therefore be assumed to equilibrate instantly with respect to the movement of the ions. The consequence is that the wavefunction of the system can be split into an electron part and a nuclear part, and we can solve for the electronic ground state first, independent of the movement of the nuclei. The total electronic energy of a system, in terms of the electron density can be written

$$E_{\text{tot}}[\rho(\vec{r})] = T[\rho(\vec{r})] + E_{\text{ee}}[\rho(\vec{r})] + E_{\text{eN}}[\rho(\vec{r})], \tag{4.3}$$

where $T[\rho(\vec{r})]$ is the kinetic energy of the system, $E_{\text{ee}}[\rho(\vec{r})]$ is the energy from the electron-electron interactions and $E_{\text{eN}}[\rho(\vec{r})]$ is the energy associated with the electron-nuclei interactions. Since it is assumed that the nuclei are fixed in space, the last term can be written as a Coulombic interaction between the nuclei and the electron density, [3]

$$E_{\text{eN}}[\rho(\vec{r})] = -\sum_A \int \frac{Z_A \rho(\vec{r})}{|\vec{R}_A - \vec{r}|} \mathrm{d}\vec{r}, \tag{4.4}$$

where A denotes the nuclei, Z_A is the charge of ion A and $\vec{R}_A$ is the position vector of ion A. The minus sign comes from the fact that this is an attractive force, and will contribute to lowering the system energy.

The second term on the right hand side in equation 4.3 can also be treated as a Coulombic interaction, where the electron density of one point in space interacts with the electron density of another point in space. This is written

$$J[\rho(\vec{r})] = \frac{1}{2} \int \int \frac{\rho(\vec{r})\rho(\vec{r}')}{|\vec{r} - \vec{r}'|} \mathrm{d}\vec{r}\mathrm{d}\vec{r}'. \tag{4.5}$$

The factor $\frac{1}{2}$ is added to avoid double counting.

The first term of equation 4.3, the kinetic energy of the electrons, is not quite as

---

[3]The observant reader would immediately notice the lack of the factor $\frac{1}{4\pi\epsilon}$. In quantum chemistry, the electron mass, elementary charge, the reduced Planck's constant as well as the aforementioned Coulomb's constant, are by default set to unity in a system known as atomic units. This gives rise to new units of length, the bohr ($a_0 = 0.5292$Å), and energy, the hartree ($E_{\text{h}} = 27.211$eV). This is done out of computational convenience.

straightforward, and again we look to Walter Kohn for guidance.

4.3   The Kohn-Sham approach

In 1965 Walter Kohn developed, together with Lu Jeu Sham, an approach to take advantage of the Hohenberg-Kohn theorems in practice [53]. This is known as the Kohn-Sham approach (KS-DFT). It essentially describes a system of non-interacting electrons under influence of an external potential that gives the correct electron density of the interacting system. In order to write an expression for the kinetic energy of the electrons, single-electron orbitals are introduced, so that the kinetic energy can be written as

$$\hat{T}_s = \sum_{i=1}^{N} \langle \phi_i | -\frac{1}{2}\nabla | \phi_i \rangle. \tag{4.6}$$

The orbitals are obtained from the Kohn-Sham equations,

$$\hat{h}_{\mathrm{KS}}\phi_i(\vec{r}) = \varepsilon_i \phi_i(\vec{r}), \tag{4.7}$$

where $\hat{h}_{\mathrm{KS}}$ is the Kohn-Sham Hamiltonian and ε_i is the orbital energy for orbital i. The Kohn-Sham Hamiltonian is given by

$$\hat{h}_{\mathrm{KS}} = \left(-\frac{1}{2}\nabla + v_{\mathrm{eff}}(\vec{r}) \right), \tag{4.8}$$

where the effective potential is given by

$$v_{\text{eff}}(\vec{r}) = v_{eN} + v_H + v_{XC}$$

$$= -\sum_A \frac{Z_A \rho(\vec{r})}{|\vec{R}_A - \vec{r}|} + \int \frac{\rho(\vec{r})\rho(\vec{r}')}{|\vec{r} - \vec{r}'|} \mathrm{d}\vec{r}' + \frac{\partial E_{\text{XC}}[\rho(\vec{r})]}{\partial \rho(\vec{r})}, \qquad (4.9)$$

and the electron density is given by

$$\rho(\vec{r}) = \sum_{i=1}^{N} \langle \phi_i | \phi_i \rangle = \sum_{i=1}^{N} |\phi_i|^2. \qquad (4.10)$$

This leads to a loop, where we need the orbitals to find the correct electron density, and we need the electron density to find the orbitals. Thus a trial electron density is fed into equations 4.7-4.8 to obtain the single-electron wavefunctions, which is then fed into equation 4.10 to calculate the electron density. If the electron density is the same as the density we started with, the ground state electron density is found, and the ground state energy can be calculated. If not, the electron density must be updated in some manner, and the process must be repeated until a self-consistent solution is found.

4.4 Exchange-correlation functional

The Coulombic term (equation 4.5) does not take the exchange interaction [4] into account. In addition, the non-interacting system of electrons used to calculate the kinetic energy (equation 4.6) are not in reality non-interacting, and there is

---

[4]This exchange interaction is also known as Pauli repulsion, and comes from the requirement that the fermion wavefunctions have to be antisymmetric, that is $\psi(1,2) = -\psi(2,1)$. Normally this is stated as the fact that each quantum state can accommodate two electrons of opposite spin, but not the same.

an energy contribution arising from the correlation between the electrons that is not included. These two effects must be corrected for, and they are lumped together in the exchange-correlation functional, E_{XC}. The total energy is then written as

$$E_{\text{tot}}[\rho(\vec{r})] = \hat{T}_s[\rho(\vec{r})] + J[\rho(\vec{r})] + E_{\text{eN}}[\rho(\vec{r})] + E_{\text{XC}}[\rho(\vec{r})]. \tag{4.11}$$

The functional derivative of E_{XC},

$$v_{\text{XC}}[\rho(\vec{r})] = \frac{\partial E_{\text{XC}}[\rho(\vec{r})]}{\partial \rho(\vec{r})}, \tag{4.12}$$

is the exchange-correlation potential that goes into the Kohn-Sham effective potential in equation 4.9.

The exchange-correlation functional is now the only part we can't calculate, and it is in expressing this we find the heart of DFT. There are several different ways of constructing the exchange-correlation functional, and a brief discussion of the most common methods is given below.

4.4.1 Local Density Approximation (LDA)

The exact exchange-correlation energy is only known for one system: the uniform electron gas at 0K. The Local Density Approximation (LDA) takes advantage of this, and sets the exchange-correlation potential equal to the exchange-

correlation potential of a uniform electron gas of the same density, that is

$$V_{\text{XC}}^{\text{LDA}}(\vec{r}) = V_{\text{XC}}^{\text{UEG}}[\rho(\vec{r})]. \tag{4.13}$$

Thus, the exchange-correlation energy depends only on the local density at $\vec{r}$, hence the name.

This idea can be extended to include spin polarization, $\sigma(\vec{r}) = \rho_\uparrow(\vec{r}) + \rho_\downarrow(\vec{r})$, in what is known as the Local Spin Density Approximation (LSDA).

4.4.2   Generalized Gradient Approximation (GGA)

Taking LDA one step further, the Generalized Gradient Approximation (GGA) also includes the gradient of the density at $\vec{r}$, that is

$$V_{\text{XC}}^{\text{GGA}}(\vec{r}) = V_{\text{XC}}[\rho(\vec{r}), \nabla\rho(\vec{r})]. \tag{4.14}$$

In this work, a version of GGA developed by Perdew, Burke and Ernzerhof and optimized for solid state calculations, PBEsol, is used [54].

4.5   Plane-wave DFT and pseudopotentials

To construct the aforementioned orbitals, there is more than one way to go about. For DFT-calculations on molecules, one would use atomic orbitals for each atom combined linearly to make up molecular orbitals (LCAO, or linear combination of atomic orbitals). This is known as a localized basis set. When

doing DFT-calculations on a periodic structure with periodic boundary conditions, plane-wave DFT is a more convenient way to go about. Plane-wave DFT applies Bloch's theorem [55]: that the wavefunction of a periodic system can be written as

$$\psi(\vec{r}) = e^{i\vec{k}\cdot\vec{r}} u(\vec{r}), \tag{4.15}$$

where $e^{i\vec{k}\cdot\vec{r}}$ is a plane wave and $u(\vec{r})$ is a function with the same periodicity as the crystal. Using a Fourier expansion of the periodic function, we obtain

$$u(\vec{r}) = \sum_{\vec{G}} u_{\vec{G}} e^{i\vec{G}\cdot\vec{r}} \tag{4.16}$$

and

$$\begin{aligned}
\psi(\vec{r}) &= e^{i\vec{k}\cdot\vec{r}} \sum_{\vec{G}} u_{\vec{G}} e^{i\vec{G}\cdot\vec{r}} \\
&= \sum_{\vec{G}} u_{\vec{k}+\vec{G}} e^{i(\vec{k}+\vec{G})\cdot\vec{r}}
\end{aligned} \tag{4.17}$$

In theory, an unlimited number of plane waves can be used. This is not feasible in practice, so a cutoff must be determined. Equation 4.17 is a solution to the Schrödinger equation with an energy

$$E = \frac{\hbar^2}{2m} |\vec{k} + \vec{G}|^2. \tag{4.18}$$

As there is a limit to how high in energy the electrons treated are, only reciprocal vectors up to a threshold corresponding to an energetic upper limit needs to be included, so that we are left with the finite sum

$$\psi(\vec{r}) = \sum_{|\vec{k}+\vec{G}|<\vec{G}_{\text{cut}}} u_{\vec{k}+\vec{G}} e^{i(\vec{k}+\vec{G}\cdot)\vec{r}}. \tag{4.19}$$

The choice of the cutoff energy depends on the number of electrons treated. As the core electrons oscillates with a small wavelength, and thus requires larger values of $\vec{k}$, a higher energy cutoff is needed in order to treat them. It is however usually the valence electrons that contribute to the interesting physical properties of a material, and there is therefore no need to explicitly treat the core electrons. Instead, these are modeled with a effective core potential, or pseudopotentials, where the electron density from these electrons are represented with a smooth electron density to match the actual properties of the core. The pseudopotentials used in this work is the projector augmented wave method (PAW) developed by Blöchl [56].

4.6 DFT+U

Materials in which ions have very localized electrons, such as transition metal ions with localized d-electrons or lanthanides with very localized f-electrons, are said to be strongly correlated. DFT has an inherent issue dealing with these kinds of systems, which comes from an erroneous self-interaction between an electron and itself. If the exchange-correlation functional was exact, this self-

interaction would cancel itself, but due to its approximate nature it doesn't. This leads to a tendency of delocalization of the electrons to minimize the self-interaction, and yields erroneous results.

A way to correct this is by applying the DFT+U method, where a Hubbard-like term is added to treat the on-site Coulombic interaction more correctly. The strength of this interaction is described by a Coulombic term, U and an exchange term, J. There are two prominent ways of doing this: either by the method of Dudarev *et al.* [57], where the effects of the exchange is averaged out and included in an effective term, $U_{\text{eff}} = U - J$, or the scheme introduced by Liechtenstein *et al.* [58], where both the Coulomb and exchange interactions enters as independent corrections.

Mellan *et al.* showed that LMO is poorly described by the scheme of Dudarev, as it can't reproduce the magnetic configuration, band gap and structure simultaneously [59]. At low values of U_{eff} the correct magnetic configuration is stabilized (A-AFM), while the band gap and structural dimensions are underestimated. For higher values of U_{eff} the band gap and structure is better reproduced, while the superexchange is destabilized, favoring a FM configuration of spins. This is due to exchange anisotropy in LMO, where the effects of the exchange is dependent on the polarization of the e_g-orbitals, arising from the Jahn-Teller splitting of these orbitals.

4.7 Convergence testing

As DFT-calculations are fairly heavy calculations, it is a goal to reduce the computational requirements of each simulation at the same time as one maintains the numerical accuracy. This is done by testing how the energy changes as the input parameters become increasingly stricter, and finding where the total energy only changes marginally when increasing the computational requirements further. At this point, the calculations are said to be well converged, and imposing stricter input parameters only causes the calculations to require more processing power, while yielding only negligible improvements.

In a DFT-calculation, there are several integrals that are computed in k-space. Since it is not possible to calculate over an infinite amount of k-points, one must divide k-space into discreet points. This is defined by a k-point mesh, and a golden rule is that a less finely divided k-point mesh is needed for larger supercells[5]. This k-point mesh should always be tested for convergence, both in order to make sure that the results are well converged, and in order to check that you are not spending an unnecessary amount of computational power on superfluous integrals in k-space.

The energy cutoff, defined in equation 4.19, must also be determined and tested for convergence. The energy must be set high enough to include all the electrons of importance, but the high-energy core electrons are usually uninteresting.

---

[5]Remember from basic solid state physics that a lengthening in real space corresponds to a shortening in reciprocal space.

Due to the Born-Oppenheimer approximation, the electron density can be found by solving the Kohn-Sham equations self-consistently, and then calculate the Hellman-Feynman forces[6] on the ions and move them accordingly. This introduces parameters for when the self-consistent electronic and ionic loops are considered converged. These convergence criterion must also be tested for convergence.

4.8   Limitations of DFT

Due to the approximate nature of the exchange-correlation functional, the solutions that are obtained from DFT is not the exact same as what we would get if we solved the Schrödinger equation. The approximations made by DFT are often very good nonetheless, but there are certain limitations that one must be aware of [51, 61, 54]:

- The electronic band gap tends to be underestimated, due to the inaccurate description of the on-site repulsion of strongly correlated systems. This can be improved by using the DFT+U-framework described in section 4.6.

- van der Waals-interactions are untreated within the LDA and GGA-functionals.

- Since the Hohenberg-Kohn theorems only applies to ground state energy, calculations of excited electronic states are often inaccurate.

- Reaction barriers of chemical reactions are often underestimated, due to the self-interaction error.

---

[6]The Hellman-Feynman theorem states that once the spatial distribution of electrons is determined from quantum mechanics, the forces acting on the nuclei are determined from classical electrostatics [60].

- The binding energies also tend to be either overestimated or underestimated, depending on the functional used. This leads to errors in the descriptions of the lattice parameters.

4.9 Vienna ab initio Simulation Package

There exists several implementations of DFT, and in this work the Vienna ab initio Simulation Package (VASP) has been used for all calculations [1, 2, 3, 4]. It is a software that implements several first-principles techniques to approximate the Schrödinger equation, such as DFT, the Hartree-Fock approach or pertubation theory (2nd order Møller-Plesset), and even quantum mechanical molecular dynamics. DFT is implemented using plane-wave basis sets (section 4.5), and norm-conserving or ultrasoft pseudopotentials or the projector augmented-wave method (PAW) [62].

The basic algorithm implemented in VASP can be summarized as such:

1. Accept starting geometry, pseudopotentials, exchange-correlation functional, definition of k-point mesh and convergence criteria. Guess a trial electron density.

2. Solve the Kohn-Sham equations self-consistently until electronic convergence criterion is reached.

3. If relaxation is performed, calculate forces on ions, and shift ion positions accordingly.

4. Repeat until ionic convergence criterion is reached.

The user has control over whether to perform a static calculation, only allow ions to change positions (fixed relaxation) or also allow lattice parameters to change (full relaxation). VASP uses symmetry considerations to speed up calculations. This means that the symmetry will not move towards lower symmetry during the calculations.

The most common files in VASP are listed below. More information on the different files can be found in appendix B.

- **INCAR**: The input file where all input parameters/tags are set. Some of the important input parameters are the cutoff energy (ENCUT), the electronic loop convergence criterion (EDIFF), the ionic loop convergence criterion (EDIFFG), the type of relaxation (ISIF), the magnetic moment (MAGMOM), the parameters that toggles the Hubbard U-correction on and off (LDAU), the type of Hubbard U-correction scheme (LDAUTYPE), values for the Hubbard U-correction (LDAUU, LDAUJ) and the exchange-correlation functional to be used (GGA).

- **KPOINTS**: Input file that defines the k-point mesh.

- **POTCAR**: Input file that specifies the pseudopotentials for the different ions.

- **POSCAR**: Input file that specifies the starting geometry, with both lattice parameters and individual ion positions.

- **OUTCAR**: Output file that summarizes the calculation.

- **CHGCAR**: Output file that contains the spatial charge density. This is also

used as input for density of states-calculations.

- **CONTCAR**: Output file that contains the resulting geometry after the calculation.

- **PROCAR**: Output file that contains the site-projected wavefunction character of each band.

- **DOSCAR**: Output file that contains the density of states and integrated density of states.

Chapter 5

Computational Details

All calculations have been performed within plane-wave DFT as implemented in Vienna *ab initio* Simulation Package (VASP) [1, 2, 3, 4], using the PBEsol functional [54]. The energy cutoff was set to 550 eV. The projector augmented-wave-method (PAW) [56, 62] was used to describe the electron-core interactions, using the pseudopotentials $La\,(5s^2p^65d^16s^2)$, $Ca\_sv\,(3s^23p^64s^2)$, $Mn\_sv\,(3s^23p^63d^54s^2)$ and $O\,(1s^22s^22p^4)$, where the explicitly treated electrons are denoted in parenthesis. In all cases the pseudopotentials with the most valence electrons have been chosen in order to treat the electronic structure most accurately and as this has been the choice in similar calculations reported in the literature [63, 59]. A Hubbard U-correction was added to the Mn d-orbitals according to the Liechtenstein-scheme [58] for $LaMnO_3$ with $U = 8$ eV and $J = 1.9$ eV, with $U = 10$ eV and $J = 2$ eV for $La_{1-x}Ca_xMnO_3$ with x = 0.125, and according to the Dudarev-scheme [57] with $U_{\text{eff}} = 4$ eV for x = 0.25 and 0.375. For all calculations a correction of $U = 10$ was added to the f-orbitals of La to push the energy states away from the Fermi level [64].

For all calculations, a 2x2x2 supercell has been used with a Γ-centered k-point mesh of 4x4x4. The initial structures were set up according to the experimentally determined structures for LMO [65] and LCMO [44] and allowed to fully relax (ISIF = 3) using vasp-5.3.5-noshear until all the forces acting on the ions converged below 0.01 eV/Å. The electronic loop convergence criterion (EDIFF) was set to 10^{-6} eV. For strain calculations, the ab-plane was fitted to a square substrate by imposing new lattice parameters $a' = b' = \sqrt{ab}$, corresponding to strain in the (001)-plane. Compressive and tensile strain was introduced by changing the lattice parameters $a' = b'$. Strain is here defined by equation 5.1. The ab-plane was kept fixed for these calculations, while the c-parameter and ionic positions were allowed to fully relax, using vasp-5.3.3bfix. For the calculations of the oxygen deficient cells, the volume was kept fixed, while the ions were allowed to relax (ISIF = 2). For density of states-calculations the electronic loop convergence criterion was increased to 10^{-8} eV and the k-point mesh was expanded to 8x8x8.

Calculations were done for the compositions $x = 0$, $x = 0.125$, $x = 0.25$ and $x = 0.375$, and are denoted LMO, LCMO 0.125, LCMO 0.25 and LCMO 0.375 respectively.

Choice of compositions, supercells and oxygen vacancies are descried below, along with descriptions of homoepitaxial strain calculations and the density of states calculations. Results from convergence testing is presented and a justification of choices of values of the Hubbard U-correction is also given.

5.1 Choice of compositions and supercells

In order to describe the orthorhombic *Pnma*-symmetry, a 2x2x2 pseudocubic supercell consisting of 40 atoms (8 [La,Ca], 8 Mn and 24 O) can be used (figure 2.1). As there are 8 La, this yields nine different possibilities of compositions ranging from pure LMO to pure CMO at intervals of $1/8^{th}$ substitution. As can be seen in the phase diagram in figure 2.3, there are exciting effects occurring at these compositions. For $x = 0.125$ ($1/8$), there is a maximum of charge ordering in the ferromagnetic insulating phase, at $x = 0.375$ ($3/8$) there is a maximum value of T_C, at $x = 0.5$ ($4/8$) there is a metal-insulator transition, at $x = 0.625$ ($5/8$) there is charge ordering again, and at $x = 0.875$ ($7/8$) there is a phase transition to a canted antiferromagnetic state.

Since the area of main technological interest is in the ferromagnetic metallic area ($0.175 < x < 0.50$), the focus will be on the compositions in the range $0 < x < 0.50$. $x = 0.50$ is excluded due to the CE-type AFM configuration, which requires a much larger supercell (4x4x4, 320 atoms) that requires a lot more computational power.

The composition of $x = 0.125$ is included, even though there is evidence for phase separation for this composition (see section 2.2.2), in which case the 2x2x2 supercell will be inadequate to properly describe the physics, as the periodic boundary conditions imply a homogeneous phase.

In addition calculations of the compositions $x = 0$, $x = 0.25$ and $x = 0.375$ will be performed. The chosen compositions will henceforth be denoted LMO, LCMO 0.125, LCMO 0.25 and LCMO 0.375 respectively.
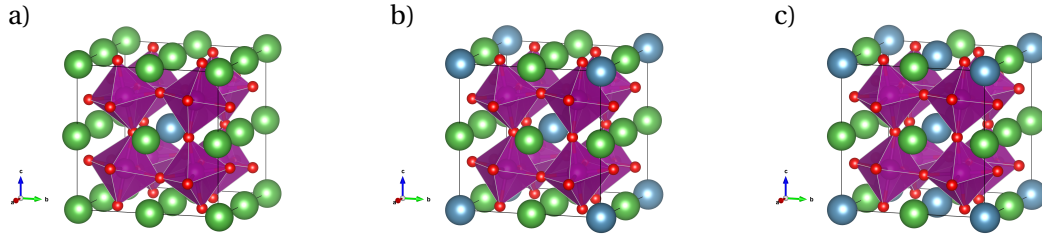
Figure 5.1: Ordering of the substituted Ca^{2+}-ions in a) LCMO 0.125, b) LCMO 0.25 and c) LCMO 0.375. Color codes: green (La), blue (Ca), purple (Mn) and red (O).

5.1.1   Cation ordering

VASP requires a starting geometry, where the cation positions are predetermined [1]. Each calculation has been performed with one fixed geometry in order to narrow the scope of the work, though this does impose an artificial ordering. In this work, each substituted cation has been placed as far away as possible from the next. The ordering is seen in figure 5.1. As pointed out in section 2.2, the cation ordering can have dramatic influence of the material properties. The cation ordering can therefore influence the results, and must be taken into consideration when interpreting the results.

5.2   Homoepitaxial strain calculations

There are two main approaches to simulate epitaxial strain: homo- and heteroepitaxial strain calculations. Homoepitaxial strain calculations confines the lattice parameters in the strained plane at a fixed deviation from the relaxed structure, thus simulating the effects of strain imposed by a substrate, while het-

---

[1]One way to circumvent this is by using the Virtual Crystal Approximation (VCA), where each cation position is weighted by the fractions of each cation present, effectively simulating a totally disordered crystal. Due to the chemical differences of La^{3+} and Ca^{2+}, there could be problems with this approach, and this has thus not been applied in this work. This is however something that could be further investigated.

eroepitaxial strain calculations explicitly includes the substrate material, thus including the chemical effects of the substrate. The former is used in this work, in order to isolate the effects that strain has on the physical properties of LCMO.

The unstrained reference structure has the same area of the strained *ab*-plane as the fully relaxed structure, but the parameters are changed so that $a = b$. That way isotropic biaxial strain can be applied, and simulate typical cubic substrates such as $SrTiO_3$. The strain is given as

$$\varepsilon = \frac{a' - a_0}{a_0}, \tag{5.1}$$

where a' is the strained lattice parameter and a_0 is the unstrained reference lattice parameter. Various degrees of strain in both the compressive ($a' < a_0$) and tensile ($a' > a_0$) regimes can then be applied, and simulated to calculate the total energy of the cell. While the strained lattice parameters are kept fixed, the c-lattice parameter is free to change, and so are the ions.

5.3   Oxygen vacancy calculations

In order to calculate the formation enthalpies for oxygen vacancies, a structure with an oxygen vacancy is compared to a stoichiometric reference structure. The reference structures for each value of strain is used to create the oxygen deficient cells, and in these calculations the unit cell volume is kept fixed, allowing only the internal coordinates to change. The formation enthalpy is calculated from

$$E_{\text{form}} = E_{\text{V}_\text{O}} - E_{\text{stoich}} + \mu_O, \tag{5.2}$$

where μ_O is the oxygen chemical potential, typically -5 eV at growth conditions under air [16].

The oxygen deficient cell can be described as $La_{1-x}Ca_xMnO_{3-\delta}$, where δ describes the deviation from stoichiometry. For a 40-atom supercell, the removal of one oxygen anion yields a very oxygen deficient cell, with $\delta = 0.125$. This large density of oxygen vacancies would make further vacancy formations unfavorable, and could artificially raise the formation enthalpy.

5.4   Choice of oxygen vacancies

During strain calculations, it makes a difference which oxygen anion is removed. Upon tensile (compressive) biaxial strain of the ab-plane, the c-parameter will decrease (increase). This means that the Mn-O-bonds in the strained plane will be elongated (compressed), while the opposite is true for the Mn-O-bonds perpendicular to the strained plane. This means the oxygen anions in the strained plane and out of the strained plane are chemically inequivalent. They are denoted in-plane oxygen vacancies (IP V_O) and out-of-plane oxygen vacancies (OP V_O), and shown in figure 5.2.

For different composition of LCMO, the picture is further complicated, as both the in-plane oxygen anions and out-of-plane oxygen anions can have different displacement towards La and Ca, as seen in figure 5.3. This displacement is due
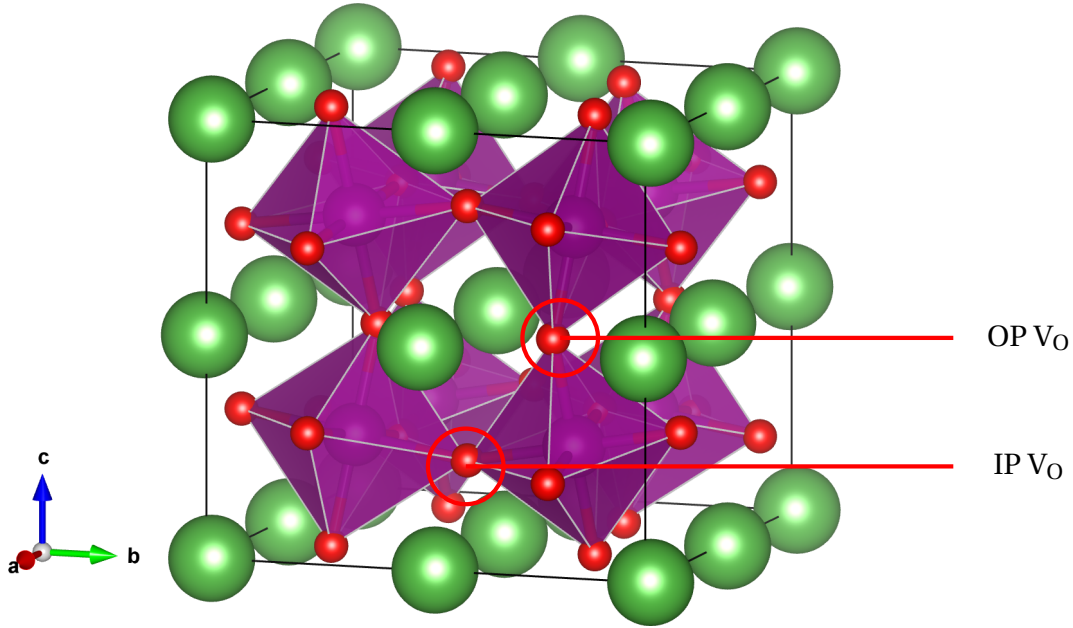
Figure 5.2: A 2x2x2 supercell of LMO showing the locations of the in-plane oxygen vacancy (IP V_O) and out-of-plane oxygen vacancy (OP V_O). The Mn-O-bonds of the in-plane oxygen lies in the strained *ab*-plane, while the the Mn-O-bonds of the out-of-plane oxygen lies out of the strained plane.

to the tilt and rotation of the MnO_6-octahedra.

Each oxygen anion has a square planar coordination of the A-cation. In the supercells of LCMO 0.25 (figure 5.1b), each oxygen anion are coordinated by 3 La-ions and 1 Ca-ion, however the bond lengths varies between the anions. For LCMO 0.125 (figure 5.1a), all out-of-plane oxygen anions are coordinated by 3 La and 1 Ca, while for the in-plane oxygen anions half are coordinated by 3 La and 1 Ca (IP-XX1) and the rest are coordinated by 4 La only (IP-La2). For LCMO 0.375 (figure 5.1c) all the out-of-plane oxygen anions are coordinated by 2 La-ions and 2 Ca-ions, while there are four in-plane oxygen anions coordinated by 3 La and 1 Ca (IP-XX1) and four that are coordinated by 2 La and 2 Ca (IP-XX2). This yields a total of five different choices for oxygen vacancies in LCMO 0.125 (IP-La1, IP-
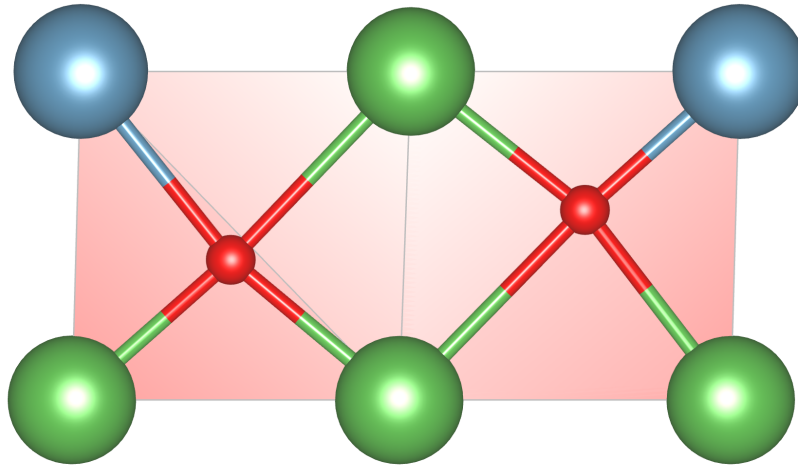
Figure 5.3: The oxygen anions are coordinated by Ca and La in a square planar configuration. The displacement of the oxygen anion towards one of the cations is clearly shown. Color codes: green (La), blue (Ca), red (O).

La2, IP-Ca2, OP-La, OP-Ca), four different choices in LCMO 0.25 (IP-Ca , IP-La, OP-Ca, OP-La) and six different choices in LCMO 0.375 (IP-Ca1, IP-Ca2, IP-La1, IP-La2, OP-Ca, OP-La).

A displacement index is here defined as a normalized sum of the weight of each of the bond lengths in the square planar configuration, where the average bond lengths of Ca-O is defined as 1, and the bond lengths of La-O is defined as the fraction of the La-O-bond length to the average Ca-O-bond length. This is given as

$$Z = \frac{1}{4}\sum_{i=1}^{4}\frac{d_i}{d_{\text{Ca,avg}}}, \tag{5.3}$$

where d_i is the (La,Ca)-O-bond length, and $d_{\text{Ca,avg}}$ is the average Ca-O bond length. Thus a value of 1 gives an oxygen anion an even displacement towards La- and Ca-cations, while a value higher (lower) than 1 means it is more dis-
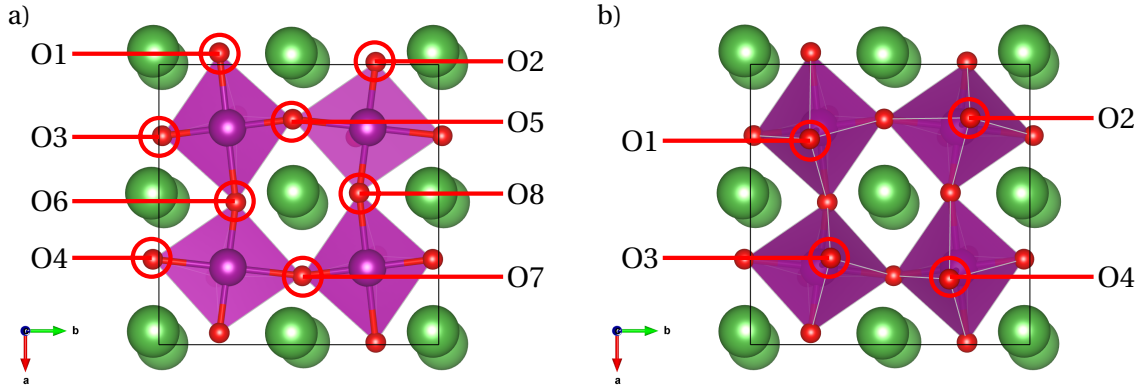
Figure 5.4: a) Labeling of the in-plane oxygen anions. The unlabeled anions are duplicates of already labeled anions. b) Labeling of the out-of-plane oxygen anions.

placed towards Ca (La). The oxygen anions are labeled according to figure 5.4.

From this, an absolute deviation from a non-displaced ion may also be defined as

$$\Delta = \sqrt{(1-Z)^2}. \tag{5.4}$$

5.5   Density of states calculations

The density of states (DOS) describes the number of available electronic states at each energy level, and describes the electronic structure. This is very important in understanding some of the physical properties, such as electronic conductivity or magnetism. The number of available states in an interval $E + \mathrm{d}E$ is given as $\rho(E)\mathrm{d}E$. Within plane-wave DFT (section 4.5), the wavefunction of the electrons are described as plane waves of the form $\psi(\vec{r}) = e^{i(\vec{k}\cdot\vec{r})}$, and these have an energy associated with them $E = \frac{\hbar^2 \vec{k}^2}{2m}$. Accurate description of the elec-

tronic structure thus requires integrals in k-space, and for accurate results this requires a more finely divided k-mesh than the ones used to calculate the total energy. By convention, the number of k-points in each direction is doubled to 8x8x8 resulting in a 8-fold increase in total number of k-points used. In addition the electronic loop convergence criterion is increased, from 10^{-6} to 10^{-8} eV.

In all calculations, a Gaussian smearing with the value of the ISMEAR-tag set to 0.01. Smearing refers to how the partial occupancies of the orbitals are calculated. There are several ways this can be done, and depending on the type of material, different smearing types are preferable. In general, for metals, the method of Methfessel-Paxton is recommended, while for insulating materials, the easy-to-use tetrahedron method with Blöchl-corrections is recommended [66]. The Gaussian method however, gives reasonable results both for metals and insulators, and since the LCMO-system shows both insulating and metallic phases, a method capable of describing both is desired.

All data from DOS-calculations has been extracted from the output files using scripts developed by the Henkelman group at the University of Texas at Austin [67].

5.6   Convergence testing

Convergence testing was carried out for 20-atom cells for LMO and LCMO 0.25 for varying k-point density and energy cutoff value, and was tested for A-AFM, G-AFM and FM configurations. The electronic (EDIFF) and ionic (EDIFFG) loop criteria were also tested for LMO and LCMO 0.25 for the experimentally deter-

mined magnetic ground states, A-AFM and FM respectively. For each parameter that was tested, the other parameters were kept constant according to table 5.1.

Table 5.1: Overview of parameters used for convergence testing of LMO and LCMO 0.25.

	k-point mesh	Energy cutoff	EDIFFG	EDIFF
k-point-test	Varied	650 eV	0.01	10^{-5} eV
Energy cutoff-test	6x6x4	Varied	0.01	10^{-5} eV
EDIFFG-test	6x6x4	650 eV	Varied	10^{-5} eV
EDIFF-test	6x6x4	650 eV	0.01	Varied

5.6.1 k-point density

Results from the k-point density test are shown in figure 5.5, where the differences between the expected ground states and the competing magnetic configurations are plotted. The results show good convergence between the different magnetic structures, with a change of less than 1 meV per formula unit when increasing the k-point mesh from 6x6x4 (144 k-points per cell) to 7x7x5 (245 k-points per cell). Going from a 20-atom cell to a 40-atom cell doubles the volume, which means the k-point density can be halved (see section 4.7). The choice for the k-mesh is thus set to 4x4x4 (64 k-points per cell) for the 2x2x2 supercell.

5.6.2   Energy cutoff

Results from the energy cutoff-test are shown in figure 5.6, where the differences between the expected ground states and the competing magnetic configurations are plotted. The results show good convergence between the different
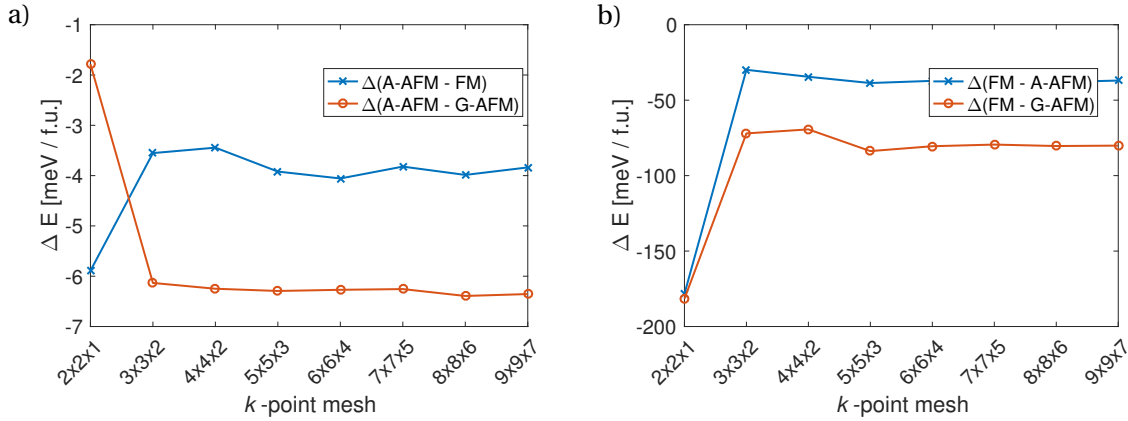
Figure 5.5: The difference in total energy per formula unit as the k-point mesh is varied between a) the A-AFM ground state of LMO and the competing FM and G-AFM states, and b) FM ground state of LCMO 0.25 and the competing A-AFM and G-AFM states.
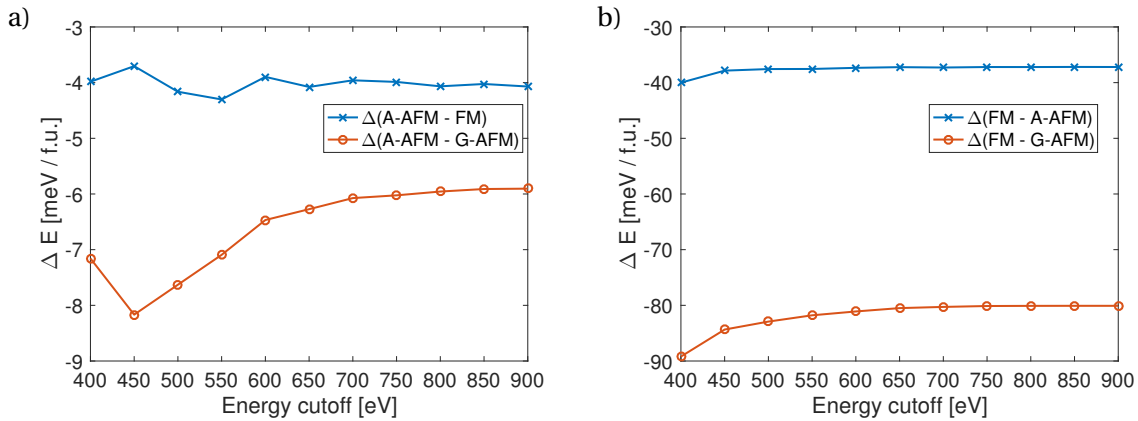
Figure 5.6: The difference in total energy per formula unit as the energy cutoff is varied between a) the A-AFM ground state of LMO and the competing FM and G-AFM states, and b) FM ground state of LCMO 0.25 and the competing A-AFM and G-AFM states.

magnetic structures, with a change of less than 1 meV per formula unit when increasing the energy cutoff beyond 550 eV for both structures, and this value is thus chosen.

5.6.3   Electronic loop convergence criterion

Results from testing the electronic loop criterion (EDIFF) are given in figure 5.7. Both structures show good convergence of the total energy of less than 1 meV

Figure 5.7: The total energy per formula unit as the electronic loop convergence criterion is varied for a) the A-AFM ground state of LMO, and b) the FM ground state of LCMO 0.25.

per formula unit for all values of EDIFF. There were however some problems achieving convergence of the ionic loop for the lower values. A value of 10^{-6} eV was chosen, as this was a well converged value that experienced no problems during the initial testing.

5.6.4 Ionic loop convergence criterion

Results from testing the ionic loop criterion (EDIFFG) are given in figure 5.8. For LMO, all values of EDIFFG yields a total energy per formula unit that lies within 1 meV of the result from the strictest criterion. For LCMO 0.25, the change in total energy per formula unit going from 0.05 eV/Å to 0.01 eV/Å was just above 1 meV. It was decided to use the value of 0.01 eV/Å, even though the total energy was well converged already for 0.05 eV/Å. This was done mainly because this stricter value has been used in previous calculations of similar materials [63, 59], allowing better comparison.
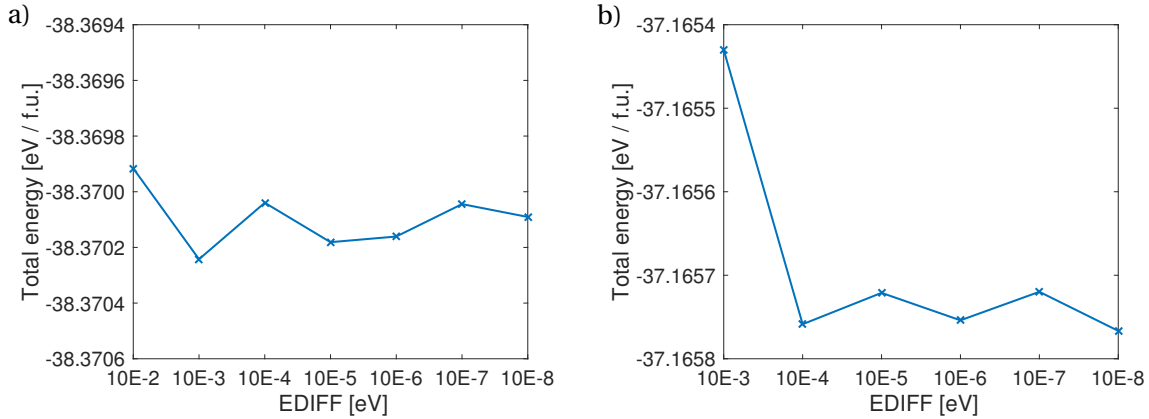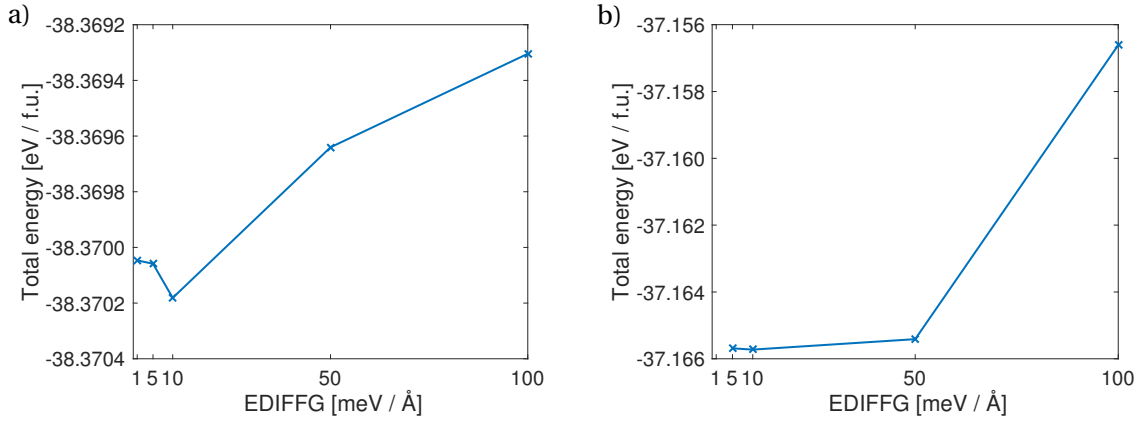
Figure 5.8: The total energy per formula unit as the ionic loop convergence criterion is varied for a) the A-AFM ground state of LMO, and b) the FM ground state of LCMO 0.25.

5.6.5   Summary of computational parameters

A summary of the computational parameters chosen from the convergence tests is given in table 5.2.

Table 5.2: A summary of the input parameters chosen for all calculations based on the convergence tests.

Parameter	Value
k-point mesh	4x4x4
Energy cut-off	550 eV
Electronic loop convergence criterion (EDIFF)	10^{-6} eV
Ionic loop convergence criterion (EDIFFG)	0.01 eV / Å

5.7   Hubbard U

5.7.1   LMO

In order to treat the highly correlated system more correctly, a Hubbard U-term (see section 4.6) was added to the Mn d-orbitals. For LMO, the choice was made

Figure 5.9: a) Total energies per formula unit for FM, A-AFM, G-AFM and C-AFM magnetic configurations for bulk LMO for $U|J = 8|1.9$ eV. b) Total energies per formula unit for FM and A-AFM as a function of strain.

based on work by Mellan *et al.* [59], where the Liechtenstein-scheme was used with values of $U = 8$ eV and $J = 1.9$ eV being the optimized values to best describe the magnetic ground state, transport properties and structural parameters. The total energies per formula unit of bulk relaxation for A-AFM, G-AFM, C-AFM and FM is given in figure 5.9a, while the stability of A-AFM and FM magnetic configurations as a function of strain is given in figure 5.9b. It can be seen that the given values of U and J stabilizes the correct A-AFM configuration for bulk and unstrained structures, and also into the tensile regime, however with a very small energy difference. In the compressive regime, the A-AFM and FM configurations both lie within 0.01 meV of each other, and can be considered degenerate within the limitations of the calculations. A band gap is correctly present in all ground state calculations, also for the FM. These results are given in chapter 6.

In addition, a value of $U = 10$ eV was added to the La f-orbitals to move them away from the Fermi-level [64, 63].

5.7.2   LCMO 0.125

An initial idea was to use the same values for the Hubbard U-correction across all compositions. Results from bulk relaxation using different magnetic configurations within the Liechtenstein-scheme with $U = 8$ eV and $J = 1.9$ eV yielded a correct magnetic ground state, but without a band gap. This is inconsistent with the reported insulating properties found in this range (see section 2.2). A range of tests were performed to find the optimized values, and these tests are summarized in table 5.3, with band gaps extracted directly from the bulk relaxation using the scripts developed by Henkelman *et al.* [67]. Values for calculations within the Liechtenstein-scheme with a value of $J = 4$ eV were not obtained, as the structures never converged. However, two candidates were found, both using the Liechtenstein-scheme, with $U|J = 10|2$ eV and $U|J = 14|2$ eV, with band gaps of 0.251 and 0.117 eV respectively. Results from bulk relaxation using these parameters for A-AFM, G-AFM, C-AFM and FM configurations are shown in figure 5.10.

Table 5.3: Band gaps obtained for LCMO 0.125 after bulk relaxation for different values of U_{eff} and $U|J$ within the Dudarev and Liechtenstein DFT+U schemes respectively.

U_{eff}	Band gap [eV]	$U|J$	Band gap [eV]
3	0.043	10|2	0.251
4	0.067	10|4	N/A
5	0.07	12|2	0.02
6	0.051	12|4	N/A
7	0.075	14|2	0.117
10	0.028	14|4	N/A

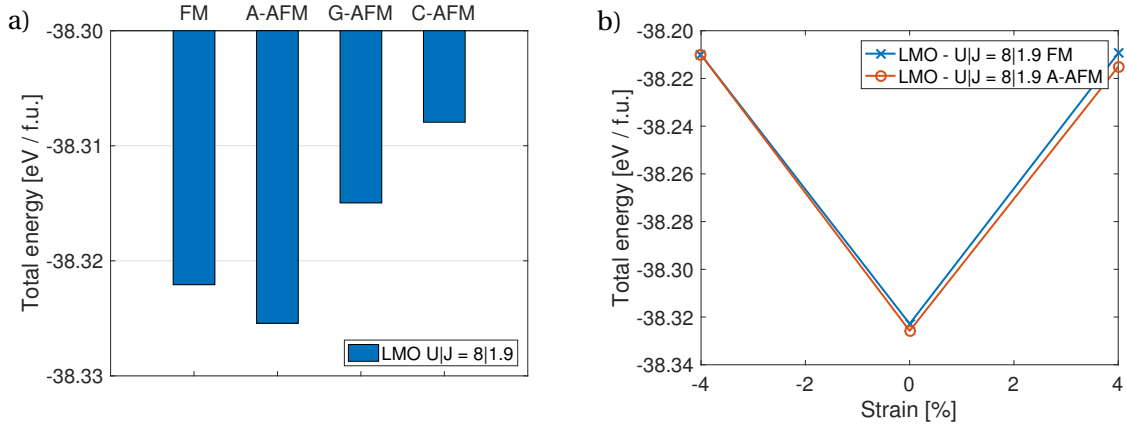The results from the magnetic configuration tests show that the experimentally

Figure 5.10: a) Total energies per formula unit for FM, A-AFM, G-AFM and C-AFM magnetic configurations for bulk LCMO 0.125 for $U|J = 10|2$ eV. b) Total energies per formula unit for FM, A-AFM, G-AFM and C-AFM magnetic configurations for bulk LCMO 0.125 for $U|J = 14|2$ eV.

determined FM ground state is not stabilized for either combination of U and J. For $U|J = 10|2$ eV it is found that an A-AFM configuration is the most stable, and for $U|J = 14|2$ eV it is found that a G-AFM configuration is the most stable. However, for $U|J = 10|2$ eV, the difference in total energies between the stabilized A-AFM configuration and FM configuration is small at around 1 meV per ion, while for $U|J = 14|2$ eV it is somewhat higher, at 5 meV per ion. Tests were performed to determine if this persisted when imposing strain, and the results are shown in figure 5.11. It was found that for $U|J = 10|2$ eV, FM configuration is stabilized with respect to A-AFM in both the tensile and compressive regime, though the energy difference is so small in the tensile regime (approximately 1 meV per ion), that it could well be a degenerate state. This is also true for G-AFM, however the change in total energies is for this case more dramatic.

Upon more accurate density of states-calculations, the band gap present in the initial calculations disappeared, resulting in a conducting FM state. For the strain calculations, the same DOS-calculations shows a small band gap of 0.085

Figure 5.11: Total energies per formula unit for FM and A-AFM magnetic configurations as a function of strain for bulk LCMO 0.125 with a) $U|J = 10|2$ eV, and b) $U|J = 14|2$ eV, also including G-AFM.

eV for the unstrained structure, but no band gap in the tensile and compressive regimes.

Of the tested values, $U|J = 10|2$ eV is deemed the most suitable parameter. The ferromagnetic state lies closer to the ground state for the bulk and unstrained structures and a lower value of U is more physical. Despite the failure in reproducing the correct insulating ground state, the results may still yield valuable insights into other physical properties. Thus all calculations shown in chapter 6 are done with these values. The failure of reproducing a FM-I phase is discussed in section 7.3.2 in light of phase separation.

5.7.3   LCMO 0.25

Bulk relaxation for different magnetic configurations using the Liechtenstein-scheme with $U = 8$ eV and $J = 1.9$ eV were performed. The correct magnetic ground state is stabilized, but upon imposing a square substrate and introducing strain, the FM ground state is destabilized with respect to an A-AFM configu-
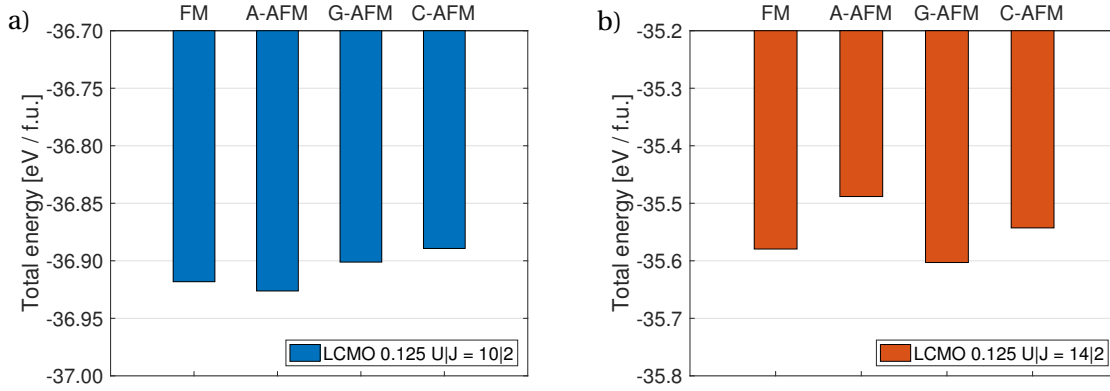
Figure 5.12: Total energies per formula unit for FM, A-AFM, G-AFM and C-AFM magnetic configurations for bulk LCMO 0.25 for $U_{\text{eff}} = 3$ and 4 eV.

ration. This is inconsistent with literature, where an FM ground state is reported to persist at least somewhere into the compressive and tensile strain regimes when grown epitaxially on a cubic substrate ($SrTiO_3$, $\epsilon \approx 1\%$) [39]. Thus, new tests had to be made to find a fitting value of the Hubbard U-correction that yields the correct magnetic ground state. This time, the Dudarev-scheme was tested for values of $U = 3$ eV and $U = 4$ eV. Results for bulk relaxation of A-AFM, G-AFM, C-AFM and FM are given in figure 5.12. The relative stability of the correct FM configuration was tested against strain, and the results are shown in figure 5.13.

For both cases the FM ground state is quite stabilized with respect to A-AFM, the energy difference lying between 10-20 meV per ion. The calculations with
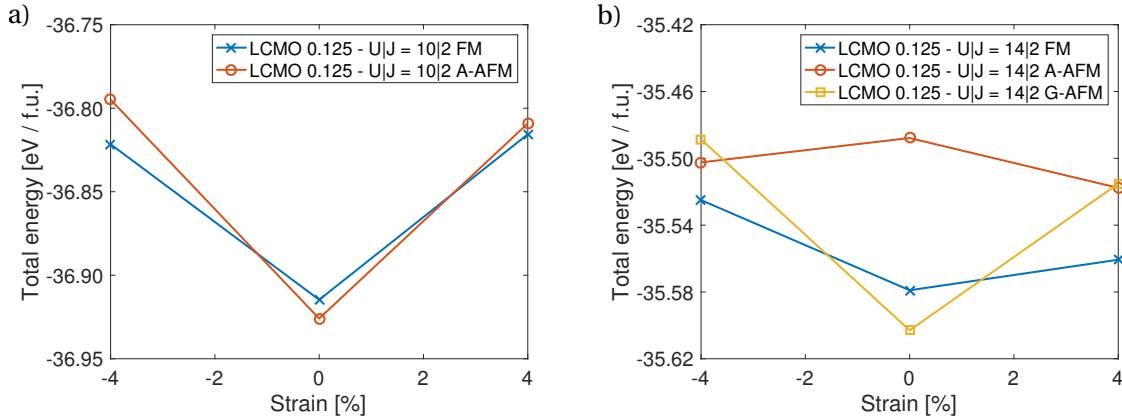
Figure 5.13: Total energies per formula unit for FM and A-AFM magnetic configurations as a function of strain for bulk LCMO 0.25 with a) $U_{\mathrm{eff}} = 3$ eV b) $U_{\mathrm{eff}} = 4$ eV.

$U_{\mathrm{eff}} = 3$ eV showed the opening of a small band gap for the tensile regime of 50 meV. While it is not unreasonable that tensile strain can destabilize the double exchange mechanism, and insulating properties have been found under tensile strain for similar compositions [39], the value of $U = 4$ eV is deemed the most suitable in order to isolate the effects of strain on the oxygen vacancy formation.

5.7.4   LCMO 0.375

Calculations of LCMO 0.375 using the Liechtenstein-scheme with values of $U|J = 8|1.9$ eV was performed. This resulted in the stabilization of the wrong magnetic ground state, and $U_{\mathrm{eff}} = 3$ eV and 4 eV within the Dudarev-scheme was tested instead. The results of the bulk relaxation with different magnetic ground states are given in figure 5.14. The FM magnetic configuration is found to be the most stable for both values of U_{eff}, and results for the strain dependence of the stabilization is shown in figure 5.15. The FM ground state stays the most stable for both values in both strain regimes. It is found that a small band gap opens up in
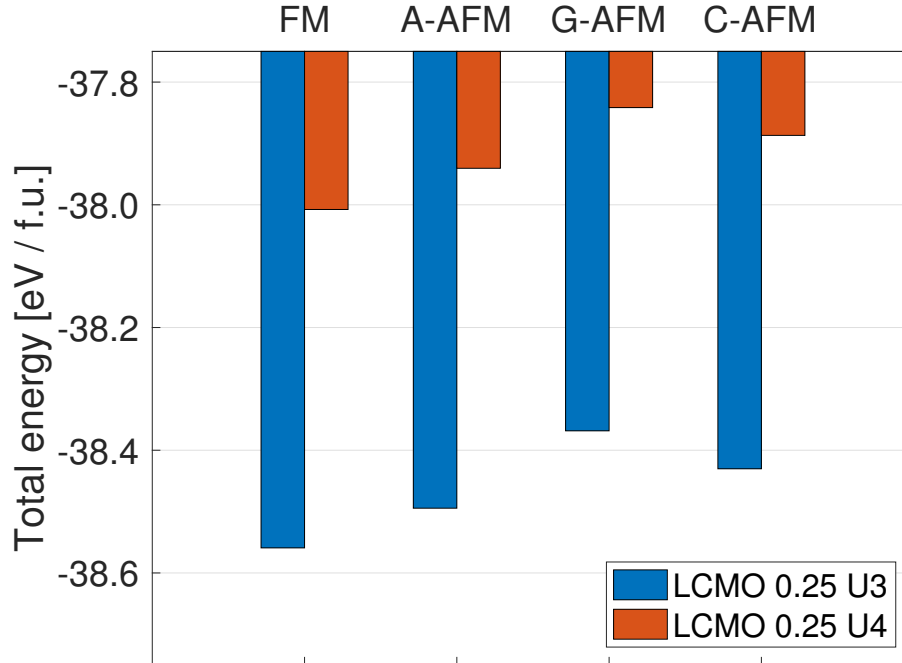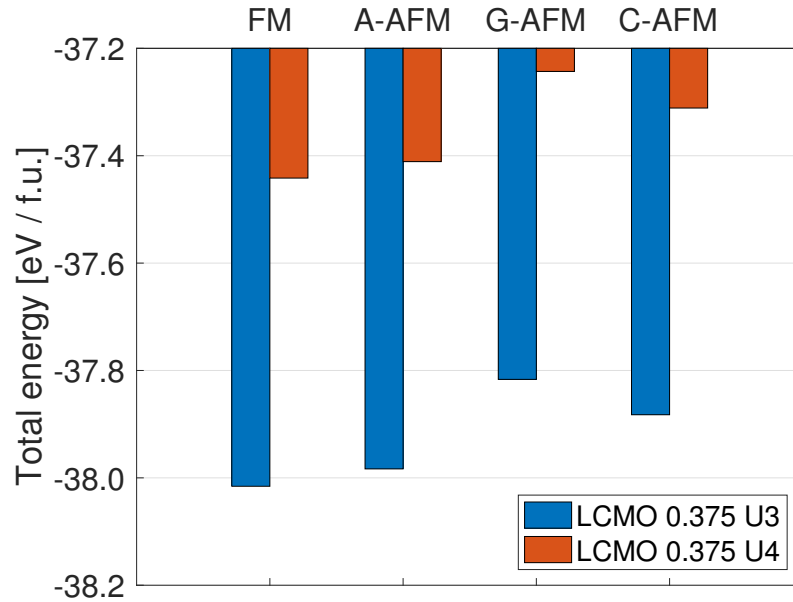
Figure 5.14: Total energies per formula unit for FM, A-AFM, G-AFM and C-AFM magnetic configurations for bulk LCMO 0.375 for $U_{\text{eff}} = 3$ and 4 eV.

the tensile regime for $U_{\text{eff}} = 3$ eV, and for the same reasons as stated above, the value of $U_{\text{eff}} = 4$ eV is chosen for all further calculations.
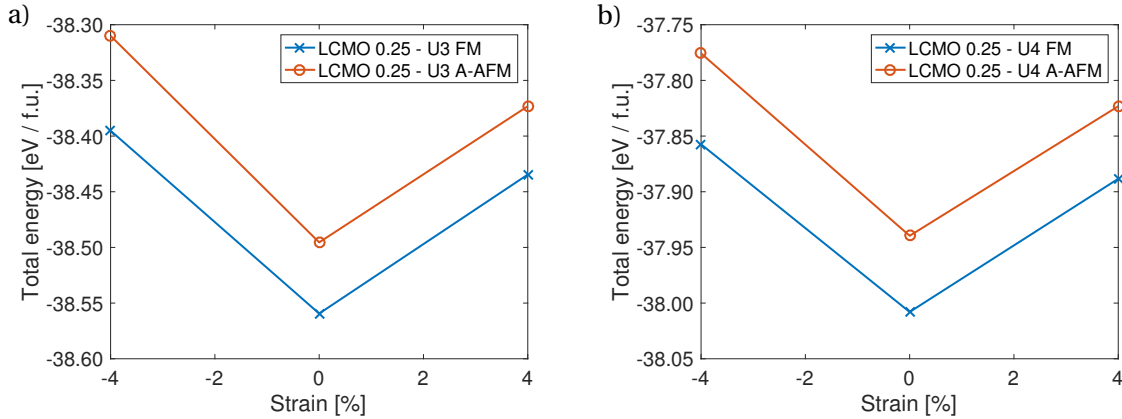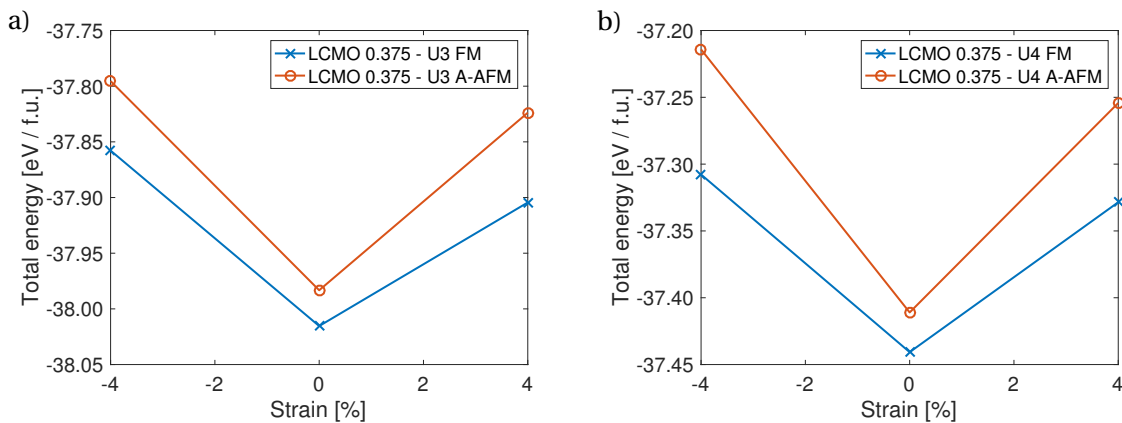

Figure 5.15: Total energies per formula unit for FM and A-AFM magnetic configurations as a function of strain for bulk LCMO 0.375 with a) $U_{\text{eff}} = 3$ eV b) $U_{\text{eff}} = 4$ eV.

5.7.5   Summary of Hubbard U-values

A summary of the DFT+U correction scheme used and the associated values for the different compositions is given in table 5.4.

Table 5.4: A summary of the DFT+U correction schemes and the associated values used in the calculations for LMO, LCMO 0.125, LCMO 0.25 and LCMO 0.375.

Composition	Correction scheme	U_{eff}/U	J
LMO	Liechtenstein	8 eV	1.9 eV
LCMO 0.125	Liechtenstein	10 eV	2 eV
LCMO 0.25	Dudarev	4 eV	N/A
LCMO 0.375	Dudarev	4 eV	N/A

Chapter 6

Results

Results from all the calculations are shown in this chapter. First structural data and results from density of states-calculations of the bulk relaxations of LMO, LCMO 0.125, LCMO 0.25 and LCMO 0.375 are presented and compared against experimental data. The results from the strained stoichiometric structures are then presented, before finally the results from the oxygen deficient cells are presented.

6.1   Bulk relaxation

Relaxation of the bulk structures is the first step in obtaining initial structures for the strained and non-stoichiometric structures, and the bulk structures are also important as references in order to understand the changes that occurs when introducing strain and oxygen vacancies. In this section, the structural data for each composition is presented, and compared to experimental data found in the literature. The electronic structure is subsequently presented and discussed,

before the compositions are compared.

6.1.1 LMO

Structural data for bulk relaxation of LMO is presented in table 6.1, and compared to the neutron diffraction study by Rodríguez-Carvajal *et al.* obtained at room temperature [65], and the neutron diffraction study by Sakai *et al.*, also at room temperature [68]. The experimental values are reported with orthorhombic symmetry (*Pnma* space group), and is transformed to the pseudocubic 2x2x2 supercell lattice parameters by multiplying the *a*- and *c*-parameters by $\sqrt{2}$.

The difference in *a* and *b*-lattice parameters seen in the neutron diffraction studies disappear in the calculations, but the error lies within 1.5-2% for both parameters, while the error in volume is negligible at less than 0.1% for both experimental reference structures. The Mn-O bond lengths are also very well described, while the octahedral tilt is underestimated by up to 4%.

Table 6.1: Lattice parameters, volume, octahedral tilt ($\angle$Mn-O-Mn) and the average Mn-O-bond lengths for the long (l), medium (m) and short (s) bond lengths for the 2x2x2 supercell of LMO, and the error compared to experimental values from Rodríguez-Carvajal [65] and Sakai[68].

	Calc.	Exp. [Ref [65]]	Δ [%]	Exp. [Ref [68]]	Δ [%]
a [Å]	7.979	7.830	+1.90	7.835	+1.84
b [Å]	7.978	8.128	-1.84	8.112	-1.64
c [Å]	7.687	7.693	-0.28	7.703	-0.41
Volume [Å^3]	489.4	489.6	-0.04	489.5	-0.02
$\angle$Mn-O-Mn [°]	24.0	24.7	-2.83	25.0	-4.00
Mn-O (l) [Å]	2.163	2.178(1)	-0.69	2.166	-0.14
Mn-O (m) [Å]	1.968	1.968(3)	+0.00	1.970	-0.10
Mn-O (s) [Å]	1.900	1.907(1)	-0.37	1.914	-0.73

In figure 6.1, the total density of states is shown. The antiferromagnetic configuration of spins can be seen from the symmetrical population of both spin channels. The A-AFM configuration is stabilized, as reported and discussed in section 5.7.1. A sizable band gap of 1.72 eV is present, which is in excellent agreement with experimental photoemission results of 1.7 eV reported by Saitoh *et al.* [69]. While there is no unambiguous value of the band gap in LMO[1], the band gap obtained from photoemission spectroscopy is considered the best comparison, since two-particle exciton effects are not included in DFT, meaning the optical gap cannot be explained by it [59].

The top of the valence band is constructed from Mn e_g- and O $2p$-orbitals, and the bottom of the conduction band is constructed from Mn e_g-orbitals. This could give rise to both a $p \rightarrow d$-transition or a $d \rightarrow d$-transition, indicating that it could be either a charge-transfer insulator or a Mott insulator.

Overall, the calculations are in good agreement with experimental results, and is considered a good basis for further work.

6.1.2 LCMO 0.125

Structural data for bulk relaxation of LCMO 0.125 is presented in table 6.2 and compared to a neutron diffraction study at 10 K by Huang *et al.* [73] and x-ray diffraction study at room temperature by Dabrowski *et al.* [74] Experimental structural data on the exact composition used in this work has been elusive,

---

[1]The size of the band gaps reported in the literature depend on the type of measurement that was done to obtain it. Band gaps based on optical absorption-measurements have been reported at 1.1 eV [70], optical conductivity at 1.9 eV [71] and Raman spectroscopy at 2 eV [72]
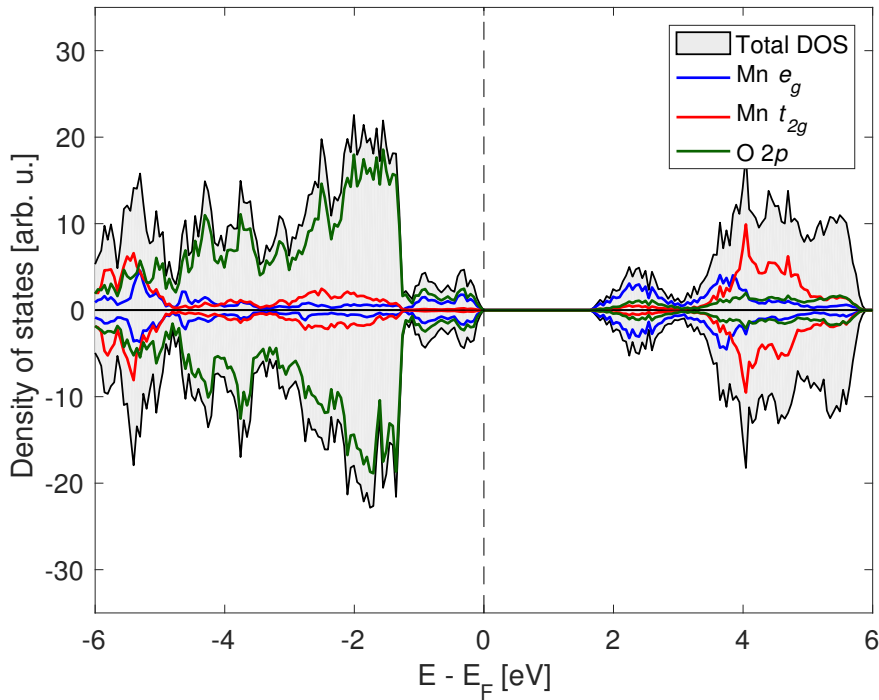
Figure 6.1: Density of states of bulk LMO. Gray area represents total density of states, while the red, blue and green lines represent the contributions from Mn e_g-, Mn t_{2g}- and O $2p$-orbitals respectively.

and the given parameters are interpolated from experimental data from compositions $x = 0.06$ and $x = 0.15$ in the study by Huang and from compositions $x = 0.10$ and $x = 0.14$ in the study by Dabrowski. This way of comparing results assumes that the change in lattice parameters is a linear function of dopant concentration. Based on the data given in Dabrowski, this is not an unreasonable assumption in the intervals $0 < x < 0.18$ and $0.18 < x < 0.38$, as seen in figure 6.2. The marked change at $x = 0.18$ corresponds to the metal-insulator transition, and can be associated with the loss of any prominent Jahn-Teller-distortion in the metallic phase. The lattice parameters have been transformed as described above. In the study by Huang, data for octahedral tilt angles and Mn-O-bond lengths were only reported from compositions $x \geq 0.15$. These results are there-
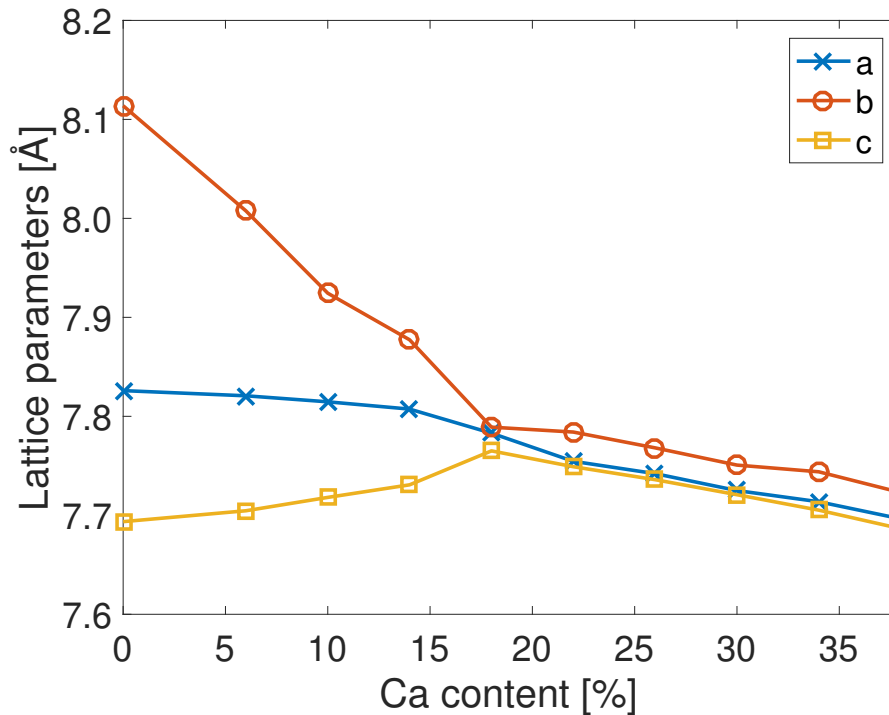
Figure 6.2: Evolution of the lattice parameters with increasing Ca-content, based on experimental data by Dabrowski [74].

fore not interpolated, but rather reported for the lowest composition of $x = 0.15$, and is not directly comparable. In the study by Dabrowski this data was not at all available.

The lattice parameters are in good agreement with the interpolated experimental results, but there are larger discrepancies in the values of the bond lengths and octahedral tilt, though it is expected that this will be larger compared to the tilt and bond lengths found in $x = 0.15$. The small difference in Mn-O-bond lengths in the study by Huang indicates the loss of Jahn-Teller distorted MnO_6-octahedra. A large Jahn-Teller distortion is characteristic of insulating properties, and the similar bond lengths in Huang's results is consistent with their reporting of a conducting phase, though inconsistent with the usual re-

ported metal-insulator transition composition of $x \approx 0.18$. A considerable Jahn-Teller distortion, as seen in the calculations, is very reasonable for this composition.

Table 6.2: Lattice parameters, volume, octahedral tilt ($\angle$Mn-O-Mn) and the average Mn-O-bond lengths for the long (l), medium (m) and short (s) bond lengths for the 2x2x2 supercell of LCMO 0.125, and the error compared with experimental values interpolated from data in Huang[73] and Dabrowski [74].

	Calc.	Exp. [Ref [73]]	Δ [%]	Exp. [Ref [74]]	Δ [%]
a [Å]^a	7.961	7.793	+2.16	7.797	+2.10
b [Å]^a	7.811	7.837	-0.33	7.895	-1.06
c [Å]^a	7.717	7.735	-0.23	7.726	-0.12
Volume [Å^3]	479.9	472.4	+1.59	475.6	+0.90
$\angle$Mn-O-Mn [°] ^{b}	22.2	20.7	+7.25	-	-
Mn-O (l) [Å] ^{b}	2.077	1.975	+5.16	-	-
Mn-O (m) [Å] ^{b}	1.970	1.972	-0.10	-	-
Mn-O (s) [Å] ^{b}	1.930	1.968	-1.93	-	-

^{a} The data have been interpolated from values given for La$_{1-x}$Ca$_x$MnO$_3$ (between $x = 0.06$ and $x = 0.15$) in Huang and (between $x = 0.10$ and $x = 0.14$) in Dabrowski.
^{b} Data for $x = 0.125$ was not available, so data for $x = 0.15$ is instead presented.

The total density of states for LCMO 0.125 is presented in figure 6.3. While an insulating phase is expected, the DOS show half-metallicity, with Mn e_g- and O $2p$-states giving rise to conduction in the majority spin-channel, while showing a large band gap in the insulating minority spin-channel. However, there seems to be very few states around the Fermi-level, which indicates that this is a very poor half-metal.

The calculations are unable to reproduce the experimentally determined FM-I bulk phase, but the structural data is still in quite good agreement with experimental results. Further investigations into strained structures and oxygen va-

Figure 6.3: Density of states of bulk LCMO 0.125. Gray area represents total density of states, while the red, blue and green lines represent the contributions from Mn e_g-, Mn t_{2g}- and O $2p$-orbitals respectively.

cancy formations were carried out despite the inability to predict the expected phase, and interpretation of those results should be approached with caution. The failure in describing this composition is further discussed in the following section.

6.1.3   LCMO 0.25

Structural data from the bulk relaxation of LCMO 0.25 is given in table 6.3, and is compared with experimental data from the neutron diffraction study by Huang, and with data from the x-ray diffraction study by Dabrowski interpolated between $x = 0.22$ and $x = 0.26$, again deemed as reasonable due to the linear evo-

lution of the lattice parameters in the given interval. The lattice parameters from the literature has been transformed as described above.

The calculations show excellent agreement with data, with deviations of less than 1% for all lattice parameters, and around 0.1% for the unit cell volume. Also the octahedral tilt and the Mn-O bond lengths show good agreement, even though the calculations exhibit a slightly distorted MnO_6-octahedra.

Table 6.3: Lattice parameters, volume, octahedral tilt ($\angle$Mn-O-Mn) and the average Mn-O-bond lengths for the long (l), medium (m) and short (s) bond lengths for the 2x2x2 supercell of LCMO 0.25, and the error compared with experimental values from Huang [73] and interpolated from data in Dabrowski [74].

	Calc.	Exp. [Ref [73]]	Δ [%]	Exp. [Ref [74]]	Δ [%]
a [Å]^a	7.797	7.754	+0.55	7.745	+0.67
b [Å]^a	7.739	7.732	+0.09	7.772	-0.42
c [Å]^a	7.712	7.754	-0.54	7.739	-0.35
Volume [Å^3]	465.4	464.8	+0.13	465.9	-0.11
$\angle$Mn-O-Mn [°]^b	20.0	20.4	-1.96	-	-
Mn-O (l) [Å]^b	1.985	1.977	+0.40	-	-
Mn-O (m) [Å]^b	1.958	1.972	-0.71	-	-
Mn-O (s) [Å]^b	1.945	1.959	-0.71	-	-

^{a} The data have been interpolated from values given for $La_{1-x}Ca_xMnO_3$ (between $x = 0.22$ and $x = 0.26$) in Dabrowski.
^{b} Octahedral tilt and bond length data not available in Dabrowski.

The total density of states is shown in figure 6.4. It is a half-metal, conducting only in one spin-channel while insulating in the other. The conducting band consists of Mn e_g and O $2p$-orbitals, which is consistent with the double exchange-mechanism. The insulating spin-channel shows a band gap of 3.4 eV. A larger density of states in the conducting spin-channel can be seen, indicating that it is a better conductor than what the results for LCMO 0.125 showed. A
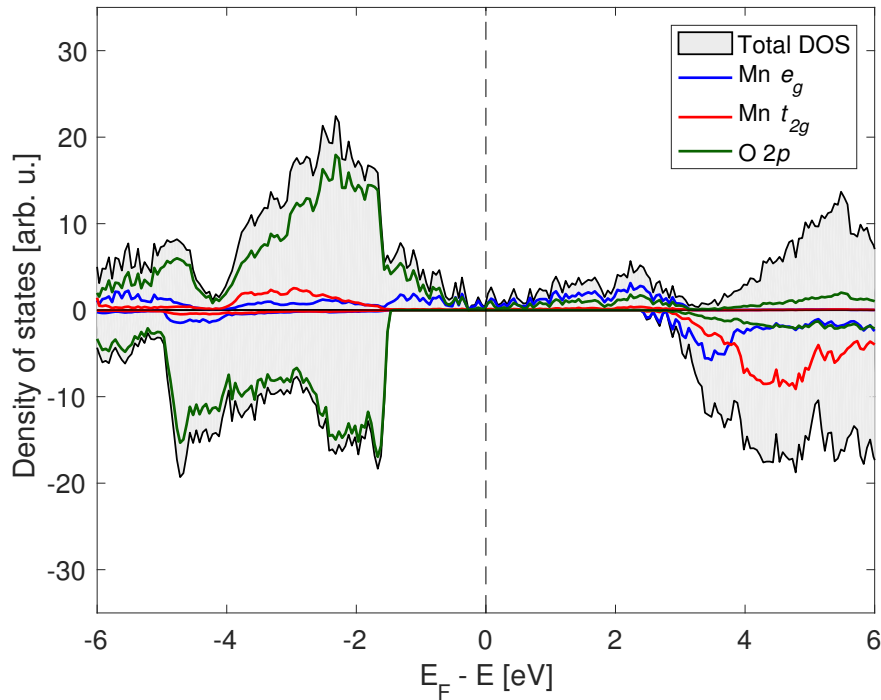
Figure 6.4: Density of states of bulk LCMO 0.25. Gray area represents total density of states, while the red, blue and green lines represent the contributions from Mn e_g-, Mn t_{2g}- and O $2p$-orbitals respectively.

conducting phase is expected for this composition. The occupied Mn t_{2g}-states are all majority spin, while the occupied states are minority spin, with some occupied Mn e_g-states as well. This indicates the high spin configuration that is expected. Some occupied Mn e_g-states are antiparallel, indicating that not all Mn^{3+} have ferromagnetic intraorbital Hund's exchange, though this is likely an artifact from the projection of the orbitals, as the peak coincides with a large O $2p$-peak.

The calculations are overall in great agreement with experimental data.

6.1.4   LCMO 0.375

The structural data from the bulk relaxation of LCMO 0.375 is given in table 6.4,
and is compared with experimental data from Huang and Dabrowski. Data for
$x = 0.375$ was not available, so the data extracted from Huang by extrapolation
of the data from the compositions $x = 0.25$ and $x = 0.33$, and interpolated be-
tween $x = 0.34$ and $x = 0.38$ in Dabrowski, which is assumed valid due to the
linear behavior discussed above. The lattice parameters have been transformed
as described above.

There is a good agreement of the lattice parameters and volume. Experimental
data for octahedral tilt and bond lengths are not available, but the slight dis-
tortion of the MnO_6-octahedra persists, while the tilt is slightly increased from
LCMO 0.25.

Table 6.4: Lattice parameters, volume, octahedral tilt ($\angle$Mn-O-Mn) and the average Mn-O-bond
lengths for the long (l), medium (m) and short (s) bond lengths for the 2x2x2 supercell of LCMO
0.375, and the error compared with experimental values extrapolated from data in Huang [73]
and interpolated from data in Dabrowski [74].

	Calc.	Exp. [Ref [73]]	Δ [%]	Exp. [Ref [74]]	Δ [%]
a [Å]^a	7.641	7.724	-1.07	7.696	-0.71
b [Å]^a	7.781	7.706	+0.97	7.724	+0.74
c [Å]^a	7.670	7.703	-0.43	7.688	-0.23
Volume [Å^3]	456.1	458.5	-0.52	457.1	-0.22
$\angle$Mn-O-Mn [°]^b	20.5	-	-	-	-
Mn-O (l) [Å]^b	1.967	-	-	-	-
Mn-O (m) [Å]^b	1.949	-	-	-	-
Mn-O (s) [Å]^b	1.933	-	-	-	-

^{a} The data have been extrapolated from values given for $La_{1-x}Ca_xMnO_3$ (from $x = 0.25$ and
$x = 0.33$) in Huang, and interpolated (between $x = 0.34$ and $x = 0.38$) in Dabrowski.
^{b} Octahedral tilt and bond length data not available for this composition.
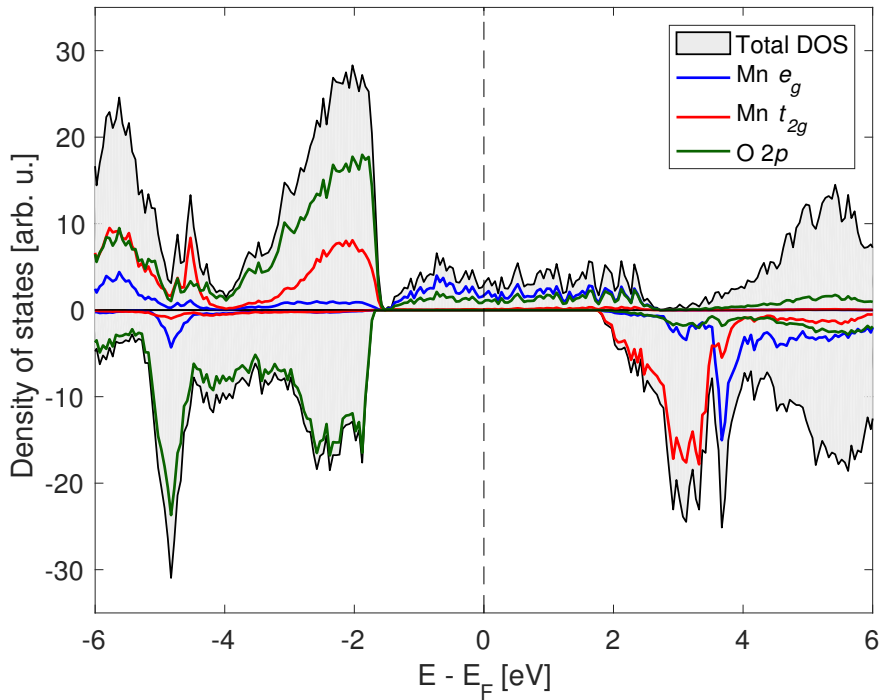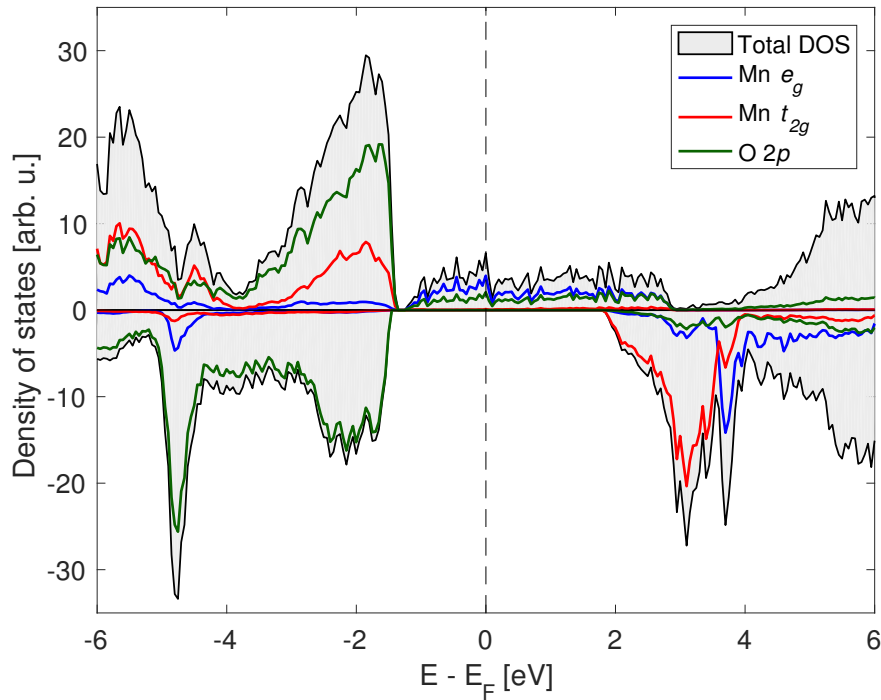
Figure 6.5: Density of states of bulk LCMO 0.375. Gray area represents total density of states, while the red, blue and green lines represent the contributions from Mn e_g-, Mn t_{2g}- and O $2p$-orbitals respectively.

The total density of states is given in figure 6.5, and as expected, it shows that LCMO 0.375 is a half-metal with conduction in Mn e_g- and O $2p$-states, characteristic of double exchange. The insulating spin-channel shows a band gap of 3.3 eV, slightly lower than for LCMO 0.25.

6.2 Strained, stoichiometric

In order to understand the effects induced by the strain, first the stoichiometric structures are investigated under compressive and tensile strain. The results are presented for each composition systematically and subsequently discussed.

6.2.1   LMO

The structural changes in stoichiometric LMO is presented in figure 6.6. The first thing to notice from figure 6.6a is that the volume increases from compressive to tensile strain, which means it has a non-ideal Poisson's ratio, and that it varies between the different regimes. This is calculated from equation 3.1 to be ν_c ~0.41 and ν_t ~0.27, with subscripts c and t denoting the compressive and tensile regimes respectively. The evolution of the lattice parameters shown in figure 6.6b, shows that the c-parameter increases as expected with compressive strain, but not enough to keep the volume constant (yellow, dashed line). With tensile strain it decreases as expected, but the rate of change is even smaller here than in the compressive regime. The a- and b-parameters are changed manually and are held fixed, and thus follows a perfect linear evolution.

In figure 6.6c, the average Mn-O-bond lengths within the strained plane, and perpendicular to it, are shown. The in-plane bond lengths follows the linear evolution of the a- and b-lattice parameters, and the out-of-plane Mn-O-bonds also follows the changes in the c-lattice parameter. The changes in the in-plane lattice Mn-O bond lengths (-0.079 Å from 0% to -4%, $+0.088$ Å from 0% to +4%), with four Mn-O-bonds in each direction, give changes of -0.317 Å in the compressive regime and $+0.351$ Å in the tensile regime. For compressive strain, this is almost equal to the change in a-lattice parameter, which means that the strain is mostly accommodated by this, and only a small increase in octahedral rotation with increasing compressive strain is expected. Instead, a small decrease is observed. For tensile strain, the total change in Mn-O-bond lengths

along one axis actually exceeds the increase in lattice parameter (+0.320 Å), and an increase of octahedral rotation will be expected to accommodate the increased bond lengths. This is also observed, as can be seen in figure 6.6d. The increase in octahedral rotation with tensile strain is contrary to what is expected when octahedral rotation itself accommodates strain, which is observed for CMO [16].

The changes in out-of-plane Mn-O-bond lengths (+0.091 Å from 0% to -4%, -0.03214 Å from 0% to +4%), give in total, with four bonds along the c-axis, a change of +0.365 Å in the compressive regime and -0.129 Å in the tensile regime. These changes are not alone enough to accommodate the changes in c-parameter (+0.428 Å for compressive, -0.223 Å for tensile), and along this axis the strain is accommodated primarily by an increase in octahedral tilt.

In figure 6.7, the change in density of Mn d-states is shown. The energy scales for the strained DOS have been aligned with the unstrained DOS by using the difference in absolute value of the Fermi energy from the output from VASP. Zero is defined as the Fermi level of the unstrained structure (dashed line), with the Fermi level of the strained structure plotted as well (dotted line). The valence band maximum (VBM) is constructed from the occupied Mn e_g-orbitals. With compressive strain, the VBM is pushed upwards in energy by 0.4 eV. At the same time, some of the unoccupied e_g-states are pushed upwards, but the conduction band minimum (CBM) stays put, leading to a decrease in band gap of 0.40 eV. For tensile strain, the VBM is pushed downwards by 0.95 eV, while the CBM is also pushed down by 0.55 eV. This leads to a net increase in band gap of 0.44 eV.

Figure 6.6: Evolution of structural parameters as a function of strain in stoichiometric LMO: a) Changes in volume per formula unit, b) changes in lattice parameters, c) changes in Mn-O bond lengths for bonds lying in the strained plane and out of it and d) changes in octahedral tilt and rotation.
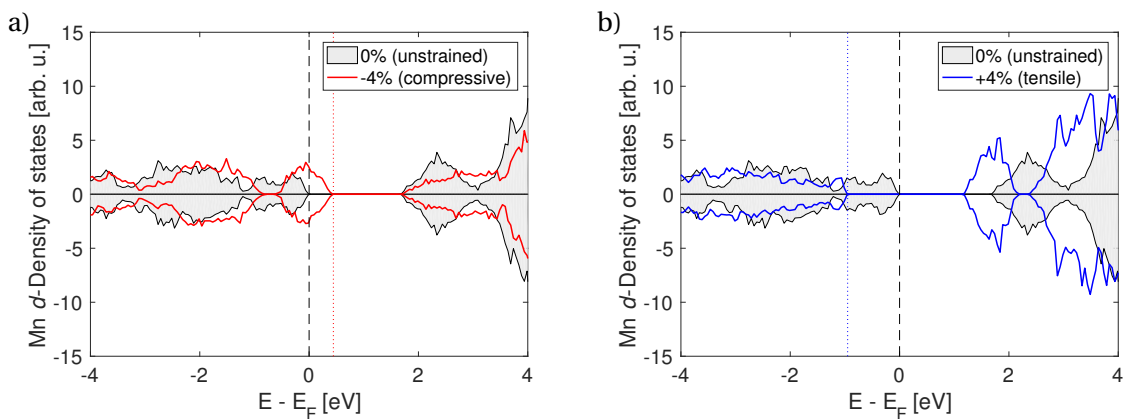
Figure 6.7: Density of Mn d-states for LMO shown for the stoichiometric cell with a) compressive strain and b) tensile strain. Gray area is unstrained, and colored lines represent the strained DOS. The dashed vertical line is the Fermi level of the unstrained cell, while the colored dotted line is the Fermi level of the strained cell.

6.2.2 LCMO 0.125

Changes in volume, octahedral tilt and rotation angles as a function of strain are given in figure 6.8. The volume increases as expected, yielding a Poisson's ratio of ν_c ~0.47 and ν_t ~0.25. The rate of change of the *c*-lattice parameter is for this compound also too small in both the tensile and compressive regimes to maintain a constant volume, though in the compressive regime it nearly has an ideal Poisson's ratio. The rate of change is smaller in the tensile regime as compared to the compressive regime. The changes in bond lengths follows this same trend.

A similar argument can be made for the behavior of the octahedral rotation in LCMO 0.125. In the compressive regime, it decreases slightly, which can be expected as the decrease in the in-plane lattice parameter (-0.315 Å) is not fully accommodated by the change in bond lengths (-0.072 Å, in total 0.289 Å along one axis). The octahedral rotation will therefore increase in the *ab*-plane. In the tensile regime, an increase in octahedral rotation is seen. Again it can be seen that the total increase in in-plane bond lengths ($+0.086$ Å, in total $+0.344$ Å along one axis) exceeds the change in lattice parameter ($+0.315$ Å).

The octahedral tilt angle increases from the compressive to the tensile regime, as expected. This is also consistent with that the changes in the out-of-plane bond lengths ($+0.501$ Å with compressive strain, -0.121 Å with tensile strain) are less compared to changes of the *c*-lattice parameter ($+0.550$ Å with compressive strain, -0.203 Å with tensile strain), requiring further strain accommodation.
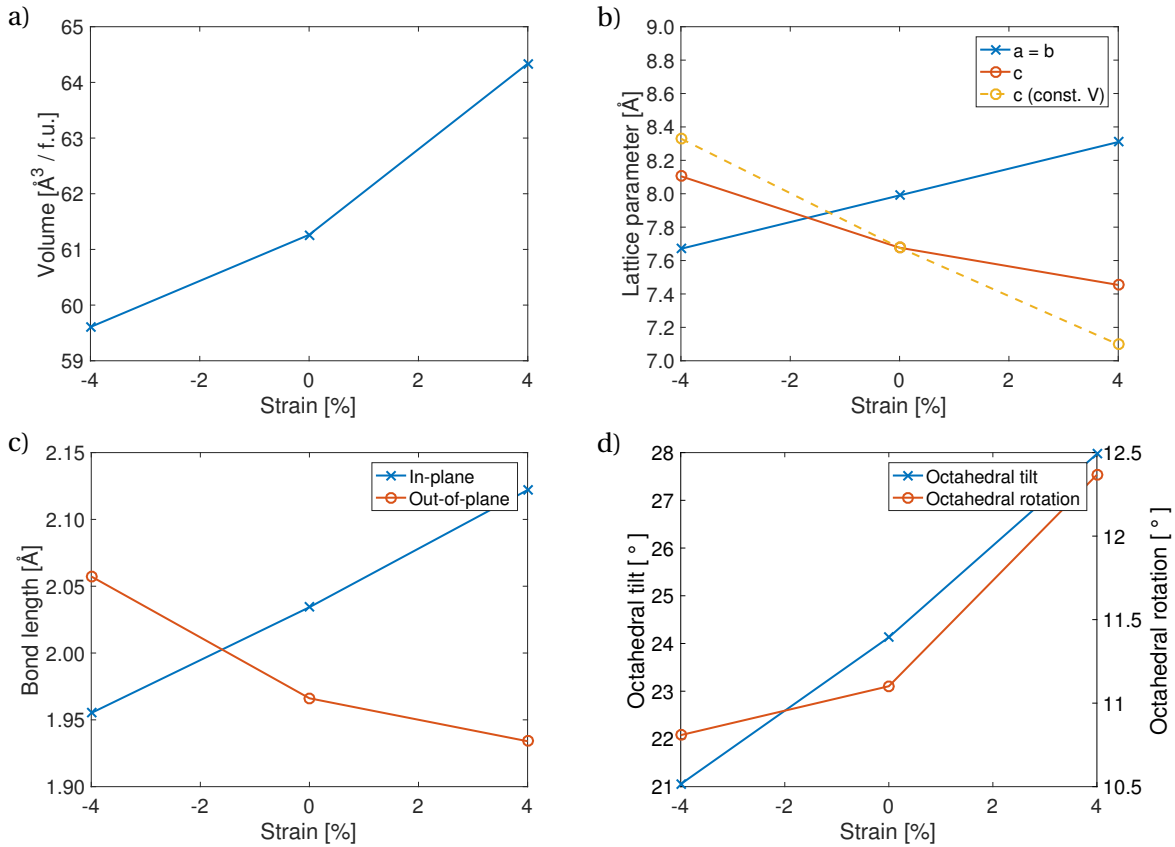
Figure 6.8: Evolution of structural parameters as a function of strain in stoichiometric LCMO 0.125: a) Changes in volume per formula unit, b) changes in lattice parameters, c) changes in Mn-O bond lengths for bonds lying in the strained plane and out of it and d) changes in octahedral tilt and rotation.

Description of the density of states has been omitted for this composition due to the failure of reproducing the expected phase.

6.2.3 LCMO 0.25

Also for LCMO 0.25, the volume increases with tensile strain (figure 6.9a), though a more linear increase is seen here. The calculated Poisson's ratio is for this composition ν_c ~0.38 and ν_t ~0.29. The rate of change of the c-parameter is still slower in the tensile regime than in the compressive regime, but the difference is smaller. The orbital ordering seen in LMO and LCMO 0.125 is gone in LCMO

0.25, which can be seen from the equal in-plane and out-of-plane bond lengths for the unstrained structure, as opposed to the two former compositions, where in-plane bonds have been longer due to a large Jahn-Teller distortion. It can be seen that the out-of-plane bond lengths increases and the in-plane bond lengths decreases with compressive strain, which is expected. There is no systematic difference between the in-plane bonds.

Tensile strain on the other hand induces a distortion of the MnO_6-octahedra, where there is a checkerboard pattern of octahedral orientation in the *ab*-plane of alternating bond lengths. The short bond lengths are the out-of-plane bonds. This orbital ordering is consistent with experimental findings of Ziese *et al.*, where LCMO 0.30 was grown on $SrTiO_3$, inducing tensile strain [39]. Here they observe orbital ordering and insulating properties.

There is still an increase in rotation in the tensile regime, due to the larger increase in the average in-plane bond lengths (+0.0819 Å, in total +0.328 Å along one axis). The decrease in the average in-plane bond lengths in the compressive regime (−0.0670 Å, in total −0.268 Å along one axis) is smaller than the change in lattice parameter (−0.328 Å), leading to the observed increase in octahedral rotation.

The changes in the *c*-lattice parameter (+0.384 Å with compressive strain, −0.254 Å with tensile strain) is also greater than the average out-of-plane bond length change (total +0.324 Å with compressive strain, −0.174 Å with tensile strain), which leads to increasing octahedral tilt going from the compressive to the tensile regime.
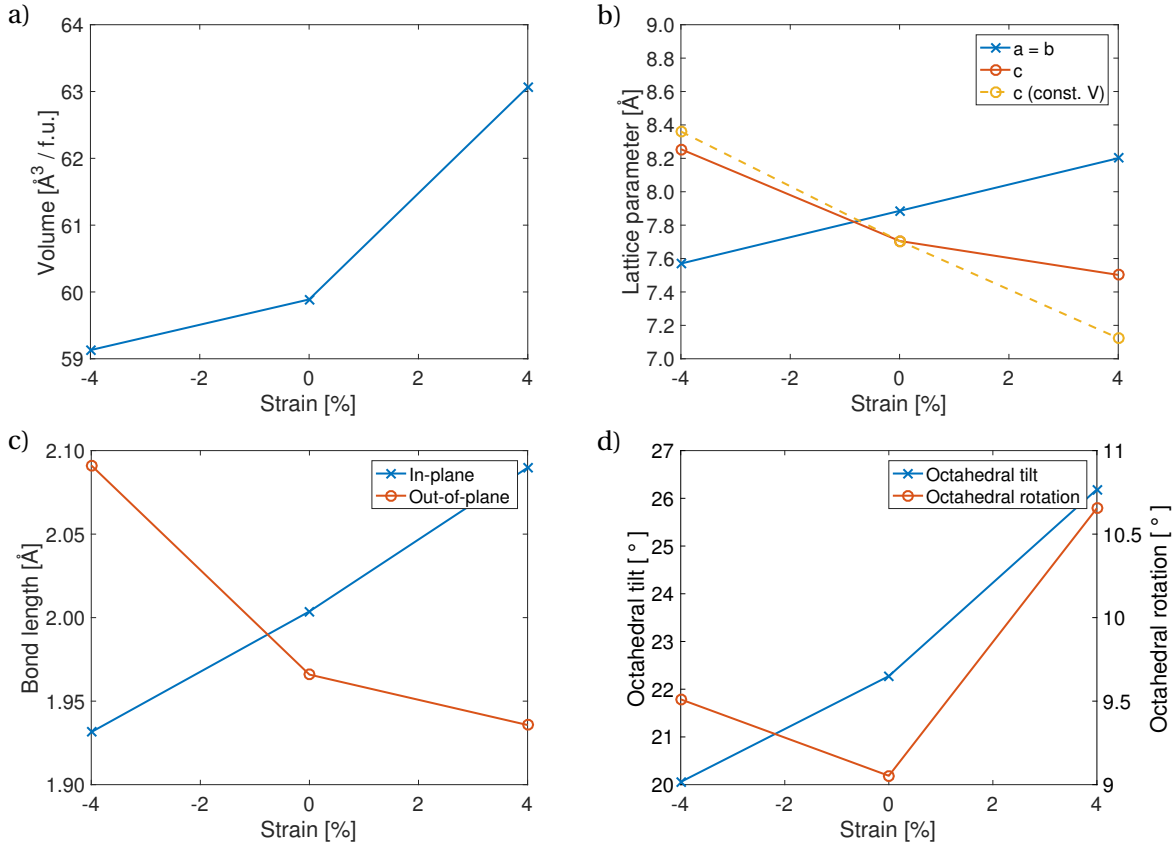
Figure 6.9: Evolution of structural parameters as a function of strain in stoichiometric LCMO 0.25: a) Changes in volume per formula unit, b) changes in lattice parameters, c) changes in Mn-O bond lengths for bonds lying in the strained plane and out of it and d) changes in octahedral tilt and rotation.

The density of Mn d-states is shown in figure 6.10. The energy scales are aligned as described above. For compressive strain, the Fermi level is pushed up by 0.58 eV, but there are no qualitative interesting differences. For tensile strain, the Fermi-level is lowered by about 0.85 eV, but also here there are no obvious qualitative differences.

6.2.4   LCMO 0.375

The volume of LCMO 0.375 is also found to increase from compressive to tensile strain, as seen in figure 6.11a, with a calculated Poisson's ratio of ν_c ~0.41

Figure 6.10: Density of Mn d-states for LCMO 0.25 shown for the stoichiometric cell with a) compressive strain and b) tensile strain. Gray area is unstrained, and colored lines represent the strained DOS. The dashed vertical line is the Fermi level of the unstrained cell, while the colored dotted line is the Fermi level of the strained cell.

and ν_t ~0.30. The same trends as in LCMO 0.25 is seen for the changes in lattice parameter, and the rate of change in the tensile regime is lower than in the compressive regime. There is no difference in in-plane and out-of-plane bond lengths for the unstrained structure, indicating no orbital ordering.

The same trends for octahedral rotation and tilt can be seen in figure 6.11d, with tilt following the expected increase due to the contraction of the c-axis, while the rotation increases in both the compressive and tensile regimes. The increase of octahedral rotation with compressive strain is consistent with that the change of total in-plane Mn-O bond lengths (-0.247 Å) is smaller than the change of the in-plane lattice parameters (-0.308 Å). The increase of rotation angle with tensile strain is in this case rather curious, as the change in in-plane Mn-O-bond lengths is the same as the change in in-plane lattice parameters (+0.308 Å). In such a case, the octahedral rotation would not be expected to change. This might instead be attributed to the extra distortion of the MnO_6-octahedra that is induced with tensile strain.
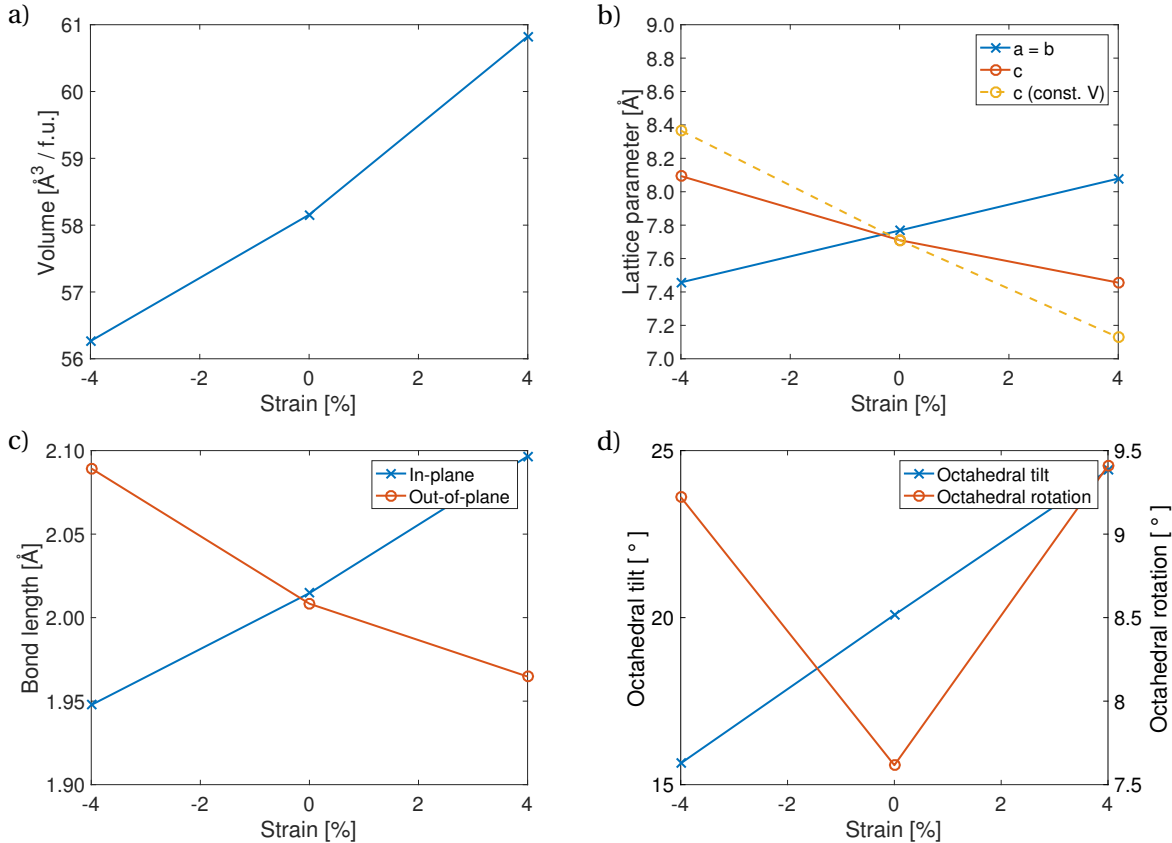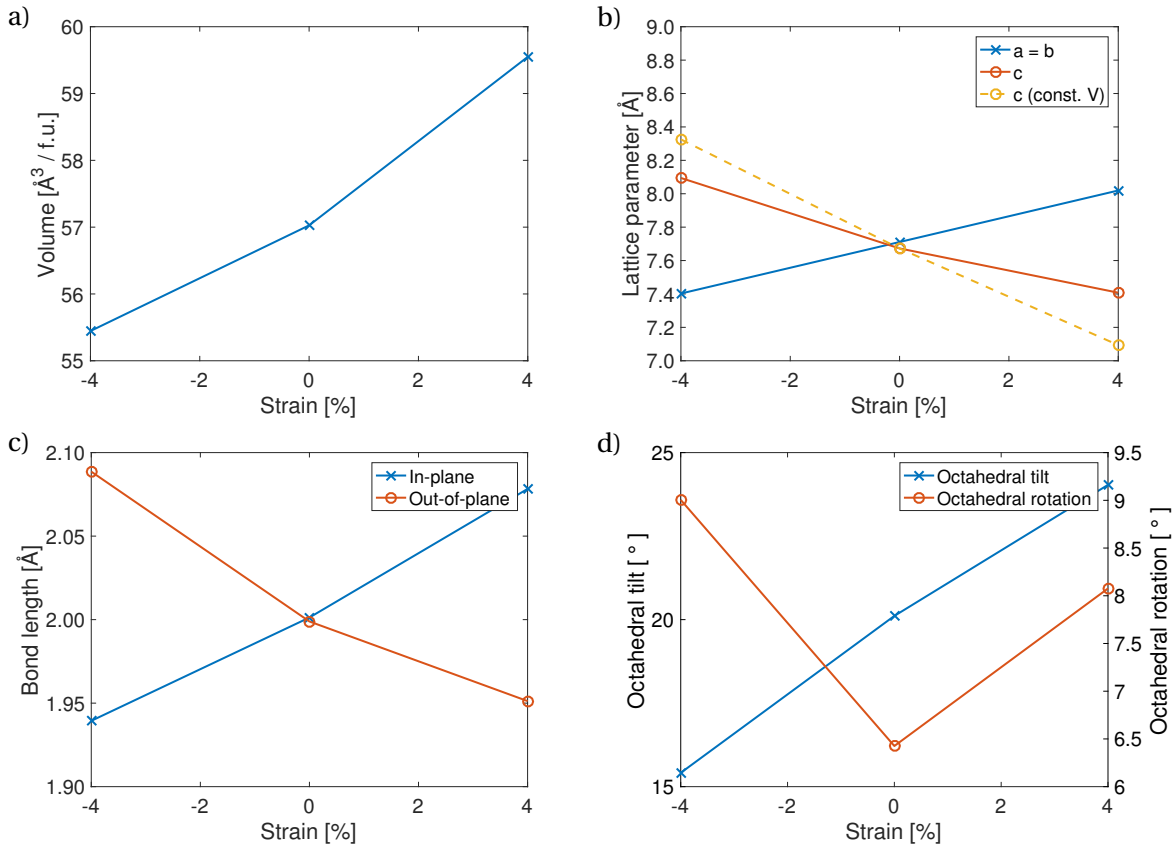
Figure 6.11: Evolution of structural parameters as a function of strain in stoichiometric LCMO 0.375: a) Changes in volume per formula unit, b) changes in lattice parameters, c) changes in Mn-O bond lengths for bonds lying in the strained plane and out of it and d) changes in octahedral tilt and rotation.

The decrease of octahedral tilt with compressive strain is consistent with that the total increase in Mn-O-bond lengths (+0.359 Å) is not enough to accommodate to change in c-lattice parameter (+0.422 Å), and the decrease of Mn-O bond lengths with tensile strain (-0.191 Å) is not enough to accommodate the decrease of the out-of-plane lattice parameter (-0.265 Å), resulting in additional accommodation from octahedral tilt angle.
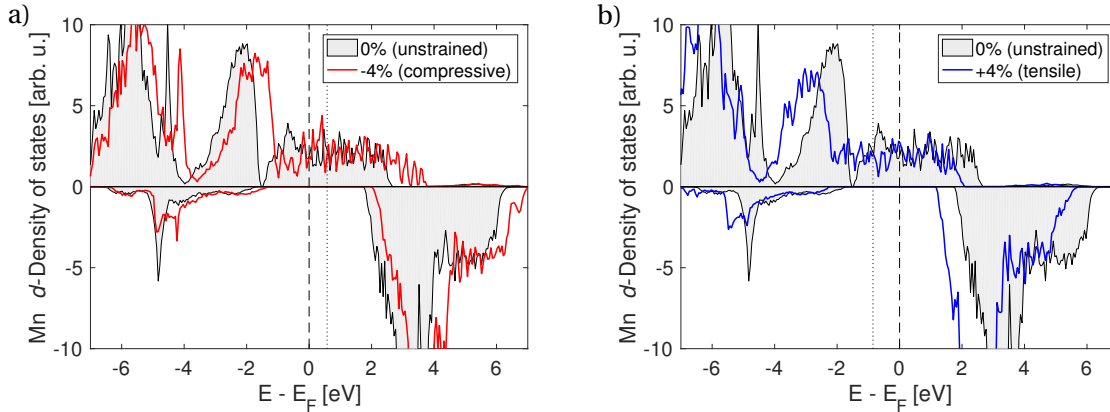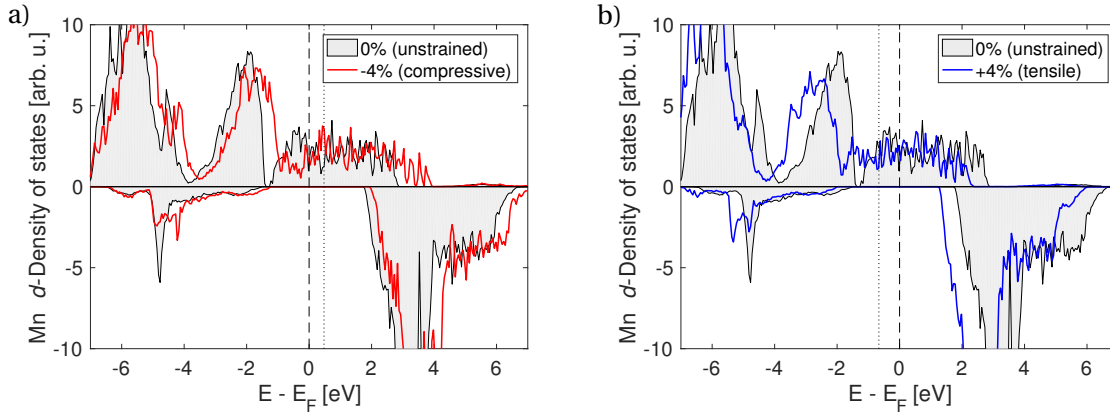
Figure 6.12: Density of Mn d-states for LCMO 0.375 shown for the stoichiometric cell with a) compressive strain and b) tensile strain. Gray area is unstrained, and colored lines represent the strained DOS. The dashed vertical line is the Fermi level of the unstrained cell, while the colored dotted line is the Fermi level of the strained cell.

6.3 Strained, oxygen deficient

6.3.1 LMO

Oxygen vacancy formation energies

The oxygen vacancy formation energies for LMO, calculated according to equation 5.2, are plotted in figure 6.13. The average formation energies for unstrained LMO is 3.95 eV, in excellent accord with the reports of 4.29 ± 0.66 eV by Nowotny *et al.* [46]. There is a large strain response for the different oxygen vacancies. Already for the unstrained structure there is a large difference (~0.17 eV) in formation energy for in-plane vacancies (IP V_O) and out-of-plane vacancies (OP V_O), the least stable being IP V_O. Further, an increase for the formation energy in the compressive regime for OP V_O by 0.18 eV, and a decrease for IP V_O by 0.20 eV is seen, making OP V_O the least stable. In the tensile regime the formation energy stays indifferent to tensile strain, while OP V_O shows a decrease of 0.24
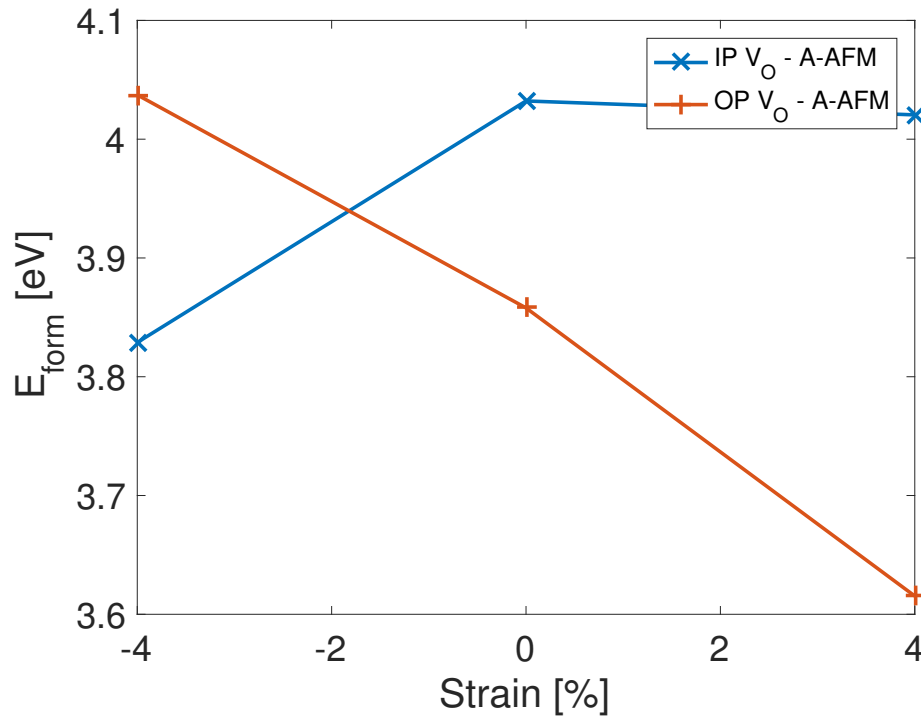
Figure 6.13: Oxygen vacancy formation energies as a function of strain in LMO.

eV. This indicates a large tendency for vacancy ordering in LMO, already for the unstrained structure.

6.3.2 LCMO 0.125

Oxygen Coordination

The displacement indices of the oxygen anions in LCMO 0.125, as defined in equation 5.3, are given in table 6.5. The oxygen anions are labeled according to figure 5.4. Oxygen anions labeled O1 through O4 are omitted, as they are all co-ordinated by 4 La. These oxygen anions also show displacement towards one of the La, which suggests that the effect is not dependent on the chemical proper-ties of the cation. This is further supported by the fact that the average effective

coordination number is 1.01, which indicates that there is no specific preference for the displacement, and that there is an equal displacement towards each cation. There is a slight increase in the average displacement towards Ca in the tensile regime for the out-of-plane oxygens (1.02), however this is quite small, and could be an effect of artificial cation ordering.

The displacements change from the compressive regime to the tensile regime. This is associated with the change in tilt and rotation of the MnO_6-octahedra, and the change in displacement indices can be seen in figure 6.14. There is no net change in displacement towards either cation, and the change in magnitude of displacement seems to be indifferent to the nature of the cation. Rather, the changes seems dependent on the ordering of the cations in the supercell, and the displacement indices might change differently with a different cation ordering. Looking at the absolute deviation from a non-displaced anion (figure 6.15), as defined by equation 5.4, it is found that there is a slight decrease in displacement of the in-plane oxygens going from compressive to tensile strain, and a relatively larger increase in the out-of-plane oxygen displacement. The increase for the out-of-plane oxygens is consistent with a higher octahedral tilt. The in-plane oxygens are harder to predict, as they are sensitive to both octahedral tilt and rotation. In total, there is a net increase in displacement going from compressive to tensile strain.

The oxygen anions chosen for the creation of vacancies are the ones that are most displaced towards either cation. From table 6.5, it can be seen that O7 for the in-plane oxygens and O2 for the out-of-plane oxygens are most displaced towards La, while O8 for the in-plane oxygens and O3 for the out-of-plane oxy-

gens are most displaced towards Ca. In addition, one of the oxygen anions only coordinated by La was chosen, and in this case O4 in figure 5.4a was arbitrarily chosen. These oxygen vacancies are labeled IP-La1, OP-La, IP-Ca1, OP-Ca and IP-La2 respectively.

Table 6.5: Overview of the displacement indices (Z) of each oxygen anion in LCMO 0.125.

IP	La1-O [Å]	La2-O [Å]	La3-O [Å]	Ca1-O [Å]	Z
O5	2.70634	2.49932	3.19478	2.68762	1.03
O6	2.57509	2.5123	3.20326	2.8316	0.98
O7	2.59187	2.8063	2.44679	3.23618	0.86
O8	3.27917	2.60911	2.78043	2.39382	1.16
OP	**La1-O [Å]**	**La2-O [Å]**	**La3-O [Å]**	**Ca1-O [Å]**	**Z**
O1	3.09452	2.53854	3.02067	2.61973	1.08
O2	2.97529	2.62493	2.44692	3.13371	0.89
O3	2.62042	3.08551	3.21892	2.38055	1.19
O4	2.40457	3.16313	2.53211	3.10222	0.90
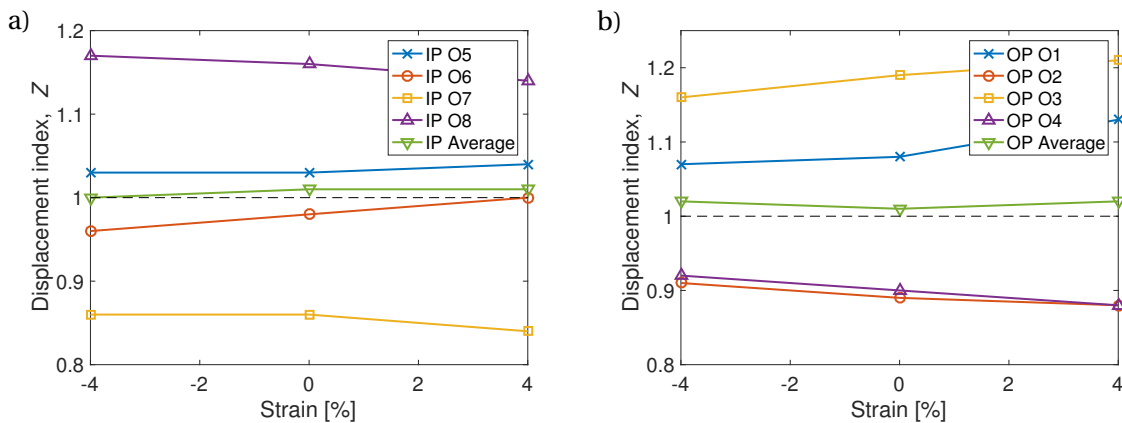
Figure 6.14: Displacement indicies in LCMO 0.125 as a function of strain for a) in-plane oxygens and b) out-of-plane oxygens.
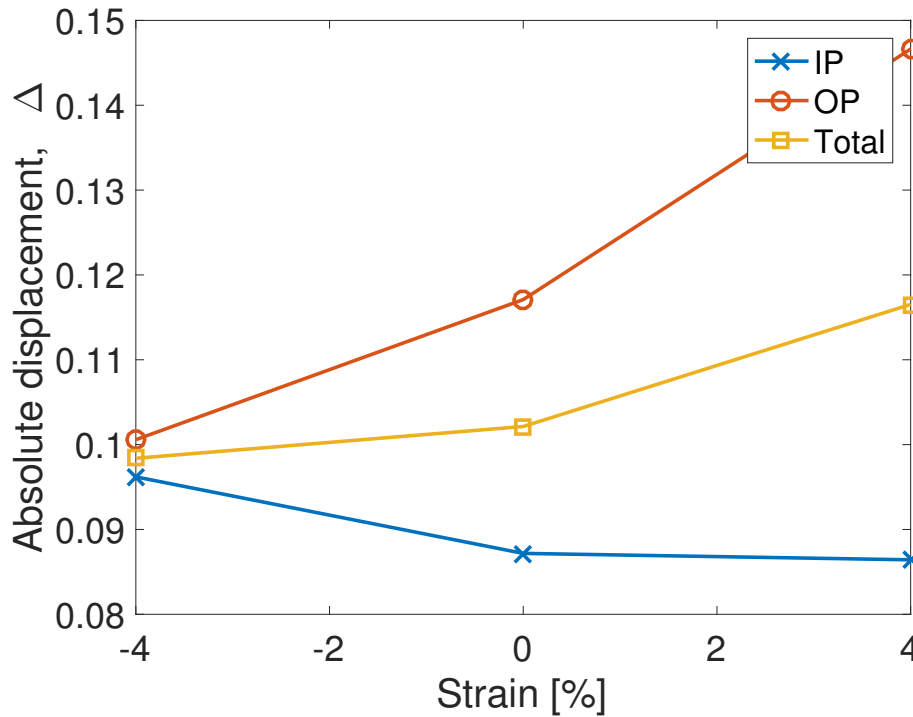
Figure 6.15: The average absolute value of displacement towards cations of in-plane (IP) and out-of-plane (OP) oxygen anions, and the average total displacement for all oxygen anions in LCMO 0.125 as a function of strain.

Oxygen Vacancy Formation Energies

The oxygen vacancy formation energies for LCMO 0.125, calculated according to equation 5.2, are plotted in figure 6.16. The formation energies (average 1.73 eV) are much lower here compared to LMO, as well as for LCMO 0.25 (section 6.3.3) and LCMO 0.375 (section 6.3.4). It is expected that these values should lie in between LMO and LCMO 0.25, though direct comparisons should be taken lightly as the values of the Hubbard U-correction is higher for this composition (see section 5.7).

All vacancies are destabilized by compressive strain. In this region, there are differences in formation energies depending on the type of vacancies, where
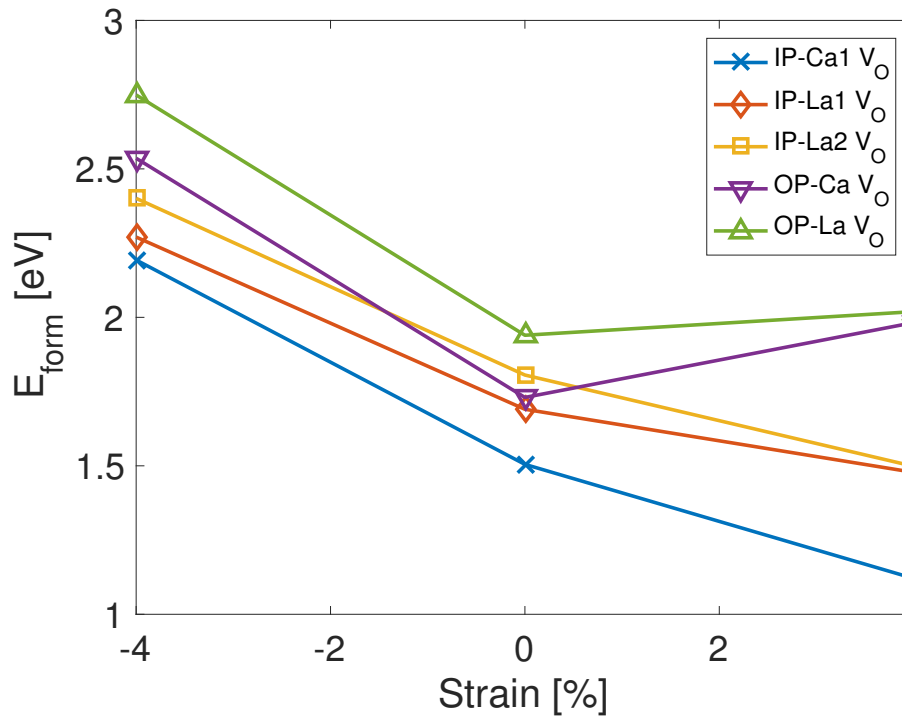
Figure 6.16: Oxygen vacancy formation energies as a function of strain in LCMO 0.125.

the OP V_O are the most unstable, and depending on the coordination of and displacement towards Ca. The OP V_O displaced towards Ca is relatively more stable, and for the IP V_O, the vacancies coordinated by four La are the least stable, followed by the ones coordinated by one Ca.

In the unstrained cells, the order is the same, except for that the Ca-displaced OP V_O is now more stable relative to the IP V_O only coordinated by La. In the tensile regime, the OP V_O are again destabilized, while the IP V_O are slightly stabilized. The two OP V_O are now grouped together and are almost degenerate, and the same is true for IP-La1 and IP-La2.

6.3.3   LCMO 0.25

Oxygen Coordination

The displacement indices of the oxygen anions in LCMO 0.25, as defined in equation 5.3, are given in table 6.6. The oxygen anions are labeled according to figure 5.4. The average displacement index for the in-plane oxygen anions is 1.00, while for the out-of-plane oxygen anions is 1.01. This again indicates that the oxygen anions exhibit no preference for either cation, and is only dependent on the tilt and rotation of the MnO_6-octahedra. For compressive strain, there is a slight change in the average displacement index for the out-of-plane oxygens (1.02), but this could be an effect of cation ordering.

The evolution of the displacements with strain is seen in figure 6.17. Looking at the absolute deviation from equal bond distances (figure 6.18), there is an increase for in-plane oxygens with both compressive and tensile strain, while there is an increase going from compressive to tensile strain for out-of-plane oxygens. The latter is expected from the increase in octahedral tilt, while the in-plane oxygens are sensitive to changes in both tilt and rotation, and are harder to predict. The total absolute displacement shows a slight increase with compressive strain, and a larger increase with tensile strain.

Oxygen Vacancy Formation Energies

The oxygen vacancy formation energies for LCMO 0.25, calculated according to equation 5.2, are plotted in figure 6.19. The average formation energy for the unstrained cell is 3.04 eV, almost 1 eV less than for LMO. There are several inter-

Table 6.6: Overview of the displacement indices (Z) of each oxygen anion in LCMO 0.25.

IP	La1-O [Å]	La2-O [Å]	La3-O [Å]	Ca1-O [Å]	Z
O1	3.07324	2.49906	2.56687	2.83607	0.97
O2	2.60162	3.12993	2.81993	2.45071	1.12
O3	2.53884	3.02291	2.70457	2.64679	1.03
O4	2.7949	2.49592	2.62145	3.12186	0.88
O5	2.70476	3.02309	2.53898	2.64637	1.03
O6	2.56703	2.49925	3.07324	2.83604	0.97
O7	2.49578	2.6214	2.79469	3.12223	0.88
O8	3.12981	2.81974	2.60164	2.45075	1.12
OP	**La1-O [Å]**	**La2-O [Å]**	**La3-O [Å]**	**Ca1-O [Å]**	Z_{eff}
O1	2.93257	2.99972	2.4832	2.55606	1.07
O2	2.79273	2.44324	2.72169	3.02884	0.91
O3	2.4423	3.0885	2.56366	3.02225	0.92
O4	3.11048	2.67947	2.89636	2.4104	1.15
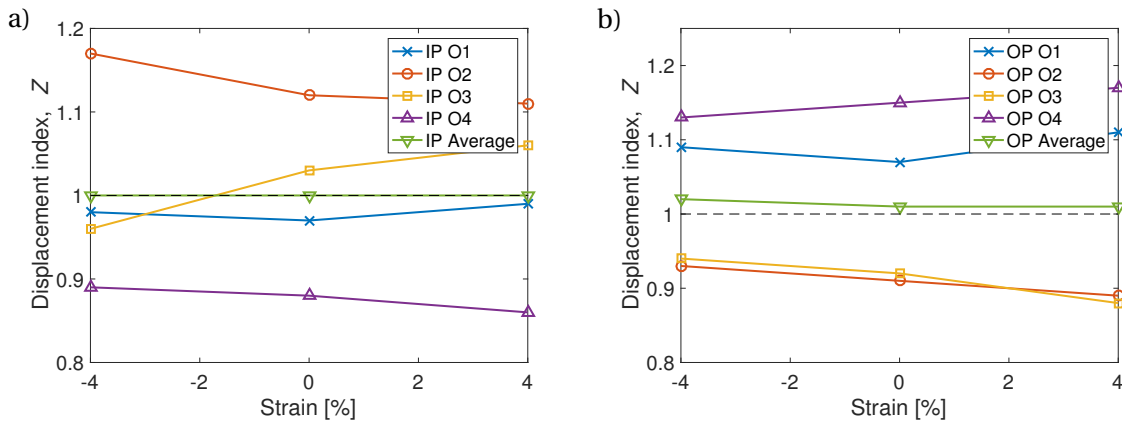
Figure 6.17: Displacement indices in LCMO 0.25 as a function of strain for a) in-plane oxygens and b) out-of-plane oxygens.
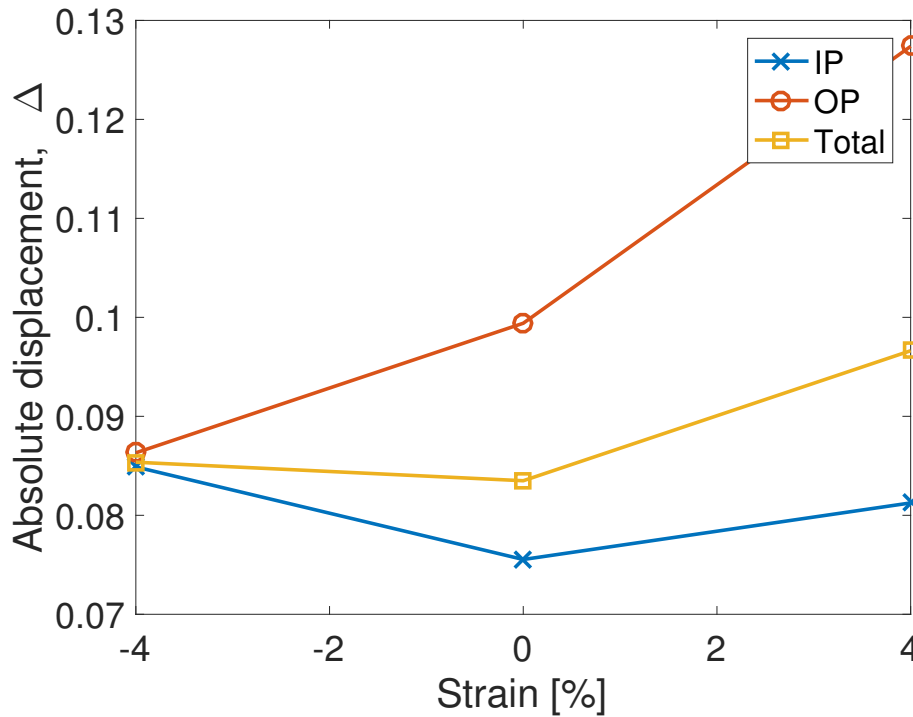
Figure 6.18: The average absolute value of displacement towards cations of in-plane (IP) and out-of-plane (OP) oxygen anions, and the average total displacement for all oxygen anions in LCMO 0.25 as a function of strain.

esting trends to notice. The first is that the formation energies of OP V_O follow the same trend as for pure LMO, by decreasing continuously from compressive to tensile strain. The second is that the formation energies for IP V_O do not, and instead follow a trend that is more similar to that of CMO, in that it is fairly indifferent to compressive strain and is stabilized by tensile strain.

The next interesting trend to notice is a shift in the grouping of the different vacancies. In the compressive regimes, the vacancies are grouped by type of vacancies. The IP V_O both have formation energies of 2.98 and 2.99 eV, and the OP V_O have formation energies of 3.39 and 3.49 eV. For the unstrained structure on the other hand, they are instead grouped by the displacement. The vacancies most displaced towards Ca are the most stable at 2.91 eV for OP-Ca V_O and 2.96
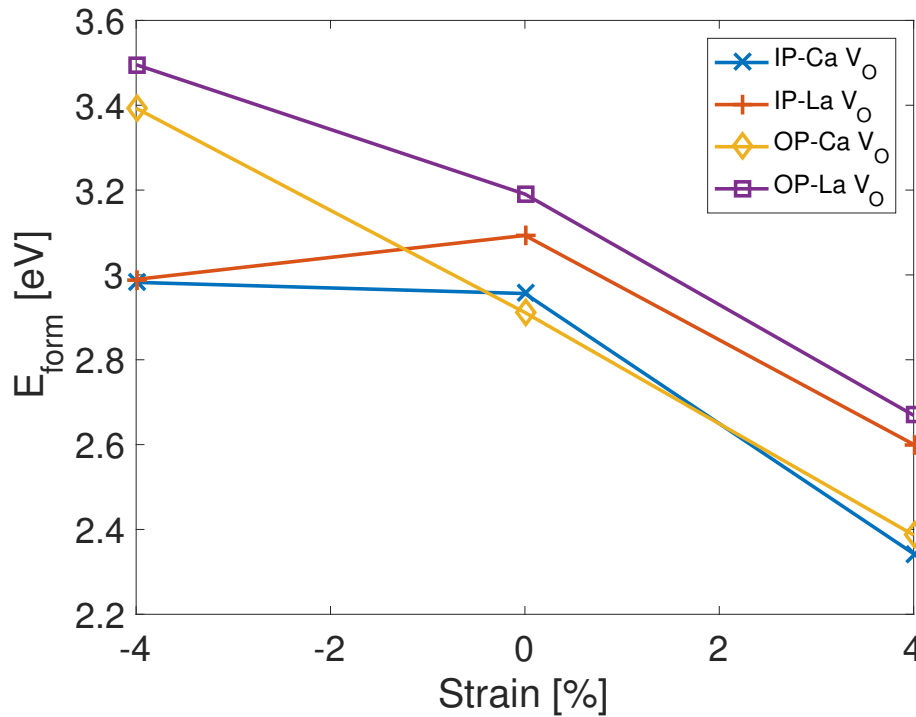
Figure 6.19: Oxygen vacancy formation energies as a function of strain in LCMO 0.25.

for IP-Ca V_O, while the vacancies displaced towards La have higher formation energies of 3.09 eV for IP-La V_O and 3.19 for OP-La V_O. This trend continues in the tensile regime, where all vacancies are stabilized with respect to the unstrained structures. All vacancies are in this case stabilized by a large amount, 0.61 eV for IP-Ca V_O, 0.52 eV for OP-Ca V_O, 0.49 eV for IP-La V_O and 0.52 eV for OP-La V_O. The difference in formation energies between the different coordination types is ~0.25-0.28 eV.

6.3.4   LCMO 0.375

Oxygen Coordination

The displacement indices of the oxygen anions in LCMO 0.375, as defined in equation 5.3, are given in table 6.7. The oxygen anions are labeled according to figure 5.4. IP1 refers to oxygens coordinated by 3 La and 1 Ca, while IP2 refers to oxygens coordinated by 2 Ca and 2 La.

The changes in displacement is seen in figure 6.20. The average displacement is more or less insensitive to strain, while there are changes in individual displacement due to the changes in octahedral tilt and rotation. From calculation of absolute deviation from a non-displaced oxygen, there is seen an increase in displacement with tensile strain for out-of-plane oxygens. For in-plane oxygens, the displacement increases both ways.

Oxygen Vacancy Formation Energies

The oxygen vacancy formation energies for LCMO 0.375, calculated according to equation 5.2, are plotted in figure 6.21. The average formation energy in the unstrained structures is 2.83 eV, 0.21 eV lower than LCMO 0.25. The same trend that is seen for LCMO 0.25 is also observed here: for compressive strain, the type of vacancy determines the formation energy while for unstrained and tensile strain, the effective coordination determines it.

For the unstrained structures, the formation energies are grouped by effective coordination, with OP and IP-XX1 V_O being degenerate and IP-XX2 V_O being rel-

Table 6.7: Overview of the displacement indices (Z) of each oxygen anion in LCMO 0.375.

IP1	La1-O [Å]	La2-O [Å]	La3-O [Å]	Ca1-O [Å]	Z
O1	3.0474	2.47802	2.56323	2.81533	0.97
O2	2.60113	2.80108	3.10836	2.42812	1.13
O3	2.53686	2.66463	2.96948	2.685	1.01
O4	2.73995	2.49984	2.65963	3.048	0.90
IP2	**La1-O [Å]**	**La2-O [Å]**	**Ca1-O [Å]**	**Ca2-O [Å]**	**Z**
O5	2.66386	2.51177	3.0697	2.65708	0.95
O6	2.55762	3.1194	2.43872	2.8233	1.04
O7	2.49572	2.72124	2.60505	3.08653	0.96
O8	3.12667	2.56534	2.81392	2.42411	1.04
OP	**La1-O [Å]**	**La2-O [Å]**	**La3-O [Å]**	**Ca1-O [Å]**	**Z**
O1	2.92355	2.9849	2.48765	2.50619	1.09
O2	2.74037	2.73899	2.44131	2.97174	0.92
O3	2.45233	3.01358	2.53451	3.01284	0.91
O4	3.08957	2.70614	2.81053	2.40479	1.14

atively stabilized by ~0.2 eV. This persists with tensile strain, though all vacancies are stabilized. IP-La2 V_O is less so, and is here destabilized compared with all Ca-displaced vacancies.

With compressive strain, the OP V_O are destabilized (0.33 eV for OP-La, 0.45 eV for OP-Ca), the IP V_O with the largest displacements towards La are slightly stabilized (0.18 eV for IP-La1, 0.22 eV for IP-La2), while the IP V_O with the largest displacement towards Ca (IP-Ca1, IP-Ca2) are insensitive to compressive strain.

This leads to the OP V_O having the highest formation energies (~3.3 eV), followed by IP-XX1 V_O (~2.8 eV) and then the IP-XX2 V_O (~2.5-2.6 eV).
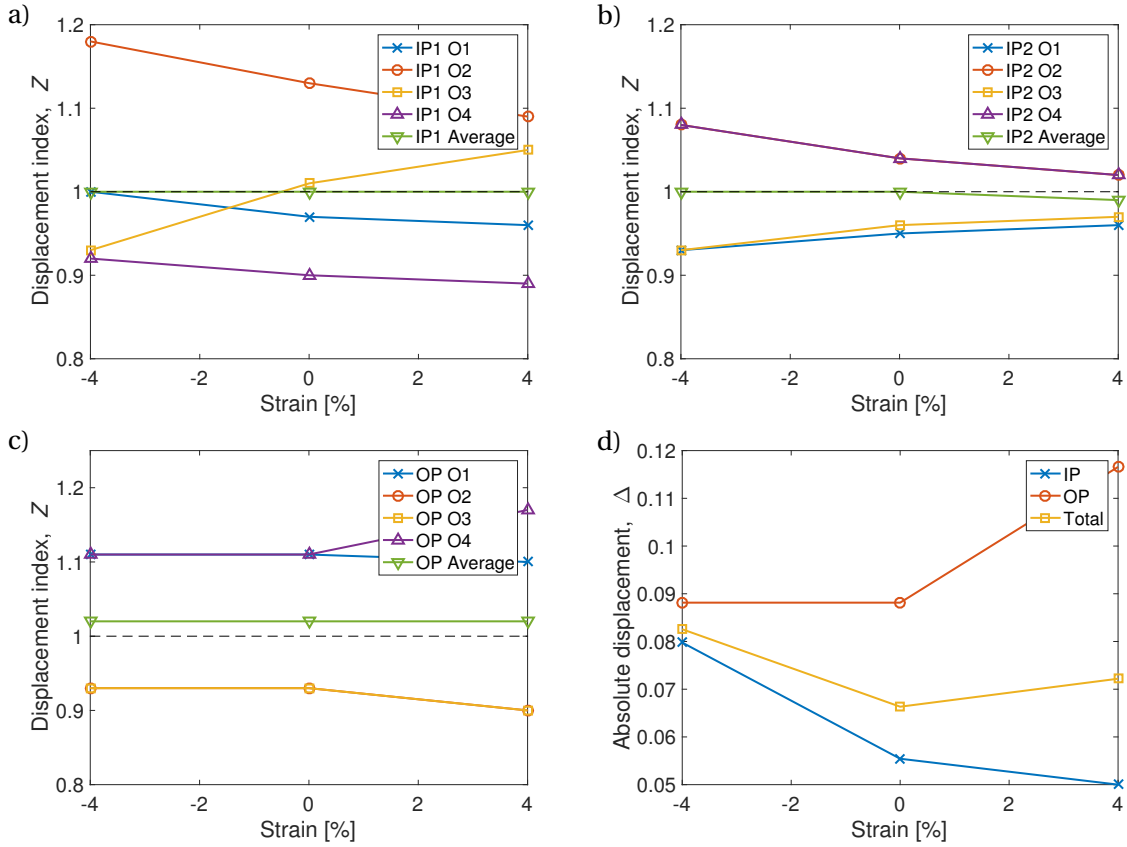
Figure 6.20: Displacement indicies in LCMO 0.375 as a function of strain for a) in-plane oxygens coordinated by 3 La and 1 Ca (IP1), b) in-plane oxygens coordinated by 2 La and 2 Ca (IP2) and c) out-of-plane oxygens (OP). d) Average absolute displacements for all in-plane oxygens (IP), out-of-plane (OP) and the average absolute displacement for all anions as a function of strain.
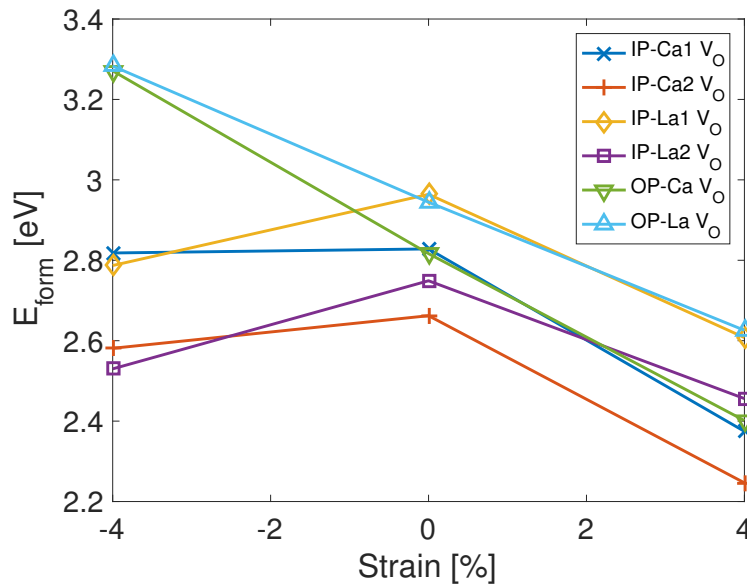
Figure 6.21: Oxygen vacancy formation energies as a function of strain in LCMO 0.375.

Chapter 7

Discussion

7.1 Structural changes

7.1.1 Evolution of structural parameters with increasing Ca-content

The evolution of the Mn-O bond lengths, octahedral tilt, octahedral rotation, lattice parameters and volume is shown in figure 7.1. The linear behavior seen in the experimental data of Dabrowski (figure 6.2) is not entirely captured in figure 7.1b, however there is a reduction of lattice parameters with increasing Ca-content. The lowering of lattice parameters is consistent with the smaller sizes of Mn^{4+} (0.53 Å) compared with Mn^{3+} (0.645 Å), and also a smaller contribution from the smaller size of Ca^{2+} (1.34 Å) compared to La^{3+} (1.36 Å) [75].

The bond lengths undergo a transition between $x = 0.125$ and 0.25, again consistent with the metal-insulator transition expected in this interval. The MnO_6-octahedra exhibit a large Jahn-Teller distortion in the insulating phase, which disappears for $x = 0.25$ and 0.375. The average bond-lengths also decrease, con-
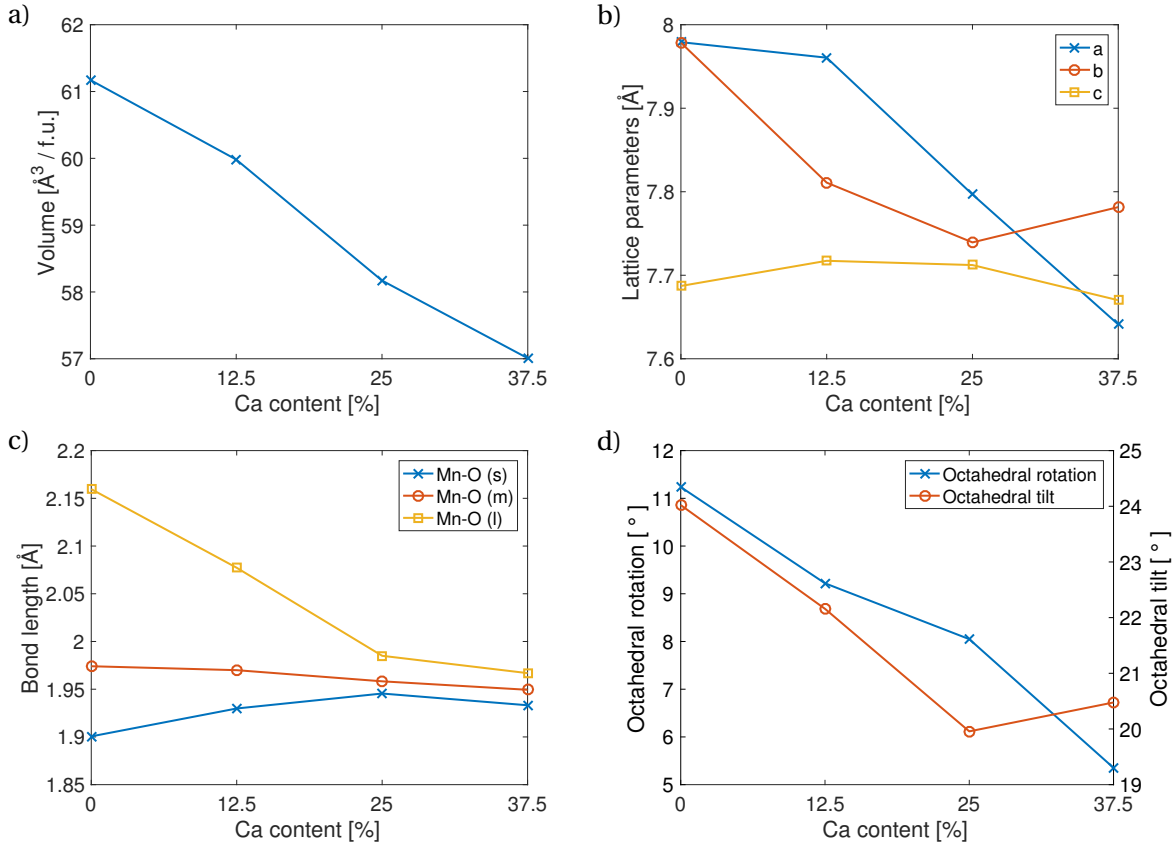
Figure 7.1: Changes in a) volume per formula unit, b) lattice parameters, c) the long, medium and short Mn-O bond lengths and d) octahedral tilt and rotation as a function of Ca-content.

sistent with a spherical model using Shannon radii [75]. While such a spherical model predicts a lowering of the bond lengths, it is too simple, and overestimates the bond lengths compared with what is found in the calculations and experiments, as can be seen in table 7.1.

In table 7.1, the tolerance factor (equation 2.2) has been calculated for the different compositions based on Shannon radii, weighting the cation sizes by Ca-content. The closer the tolerance factor is to the ideal perovskite ($t = 1$), the closer to cubic symmetry is expected, while smaller values will tend towards orthorhombic and rhombohedral symmetry. While this is not entirely determined by the ion sizes, the increasing trend seen in the tolerance factor with increas-

ing Ca-content indicates that the deviation from ideal Mn-O bond angles of 180°
could be expected to decrease. A general decrease in octahedral tilt and rotation
is seen in figure 7.1d, though there is a slight increase in tilt from LCMO 0.25 to
0.375.

Table 7.1: Average calculated Mn-O bond lengths, theoretical Mn-O bond lengths predicted
from a spherical model and tolerance factor of LMO, LCMO 0.125, LCMO 0.25 and LCMO 0.375.

Composition	Average Mn-O bond length [Å]	Theoretical Mn-O bond length [Å]	Tolerance factor
LMO	2.01	2.07	0.952
LCMO 0.125	1.99	2.05	0.958
LCMO 0.25	1.96	2.04	0.964
LCMO 0.375	1.95	2.02	0.970

7.1.2   Counterintuitive increase in octahedral rotation with tensile strain

It is expected, when octahedral rotation changes to accommodate strain, that
the rotation will decrease when biaxial tensile strain is applied. Instead it was
found for all compositions that octahedral rotation in the ab-plane counterin-
tuitively increase with tensile strain.

A possible explanation of this lies with the Jahn-Teller-distortion of the MnO_6-
octahedra (see section 2.2). With tensile strain, the distance between the ions
increase, and the electrostatic repulsion between electron clouds from neigh-
boring ions decrease. This can allow the increase in Jahn-Teller distortion of
the octahedra, further enhancing the energy gain from the Jahn-Teller energy
splitting. The bond lengths increases to such an extent that octahedral rotation
must increase in order to accommodate the increased bond lengths, rather than

decrease to accommodate the strain. For compressive strain, or no strain at all, part of this distortion is quenched due to the increased electrostatic repulsion. The standard deviation, σ_ϵ, of the Mn-O-bond lengths in the strained plane can be used as a measure of the magnitude of the Jahn-Teller distortion, and this is given in table 7.2. It is seen that this in all cases increases with tensile strain, and decreases with compressive strain. It is also seen that the magnitude of the Jahn-Teller distortion decreases with increasing Ca-content for the unstrained structures, which is expected as there are more Jahn-Teller inactive Mn^{4+}-ions in these compounds.

The larger increase in bond length compared to increase in lattice parameter is found for LMO, LCMO 0.125 and LCMO 0.25, while for LCMO 0.375 the bond length increase was found to be the same as the increase in lattice parameter, indicating that the aforementioned explanation cannot fully explain the observation. The changes are summarized in table 7.3.

Table 7.2: Standard deviation, σ_ϵ, of the in-plane Mn-O bond lengths, as an indication of the magnitude of the Jahn-Teller distortion. The subscript denotes the magnitude of the strain.

Composition	$\sigma_{-4\%}$ [Å]	$\sigma_{0\%}$ [Å]	$\sigma_{+4\%}$ [Å]
LMO	0.1229	0.1876	0.2636
LCMO 0.125	0.0489	0.0885	0.1360
LCMO 0.25	0.0096	0.0191	0.0644
LCMO 0.375	0.0159	0.0173	0.0219

Table 7.3: Changes of in-plane Mn-O-bond lengths and in-plane lattice parameters with strain for LMO, LCMO 0.125, LCMO 0.25 and LCMO 0.375.

Composition	Δab [Å]	ΔMn-O [Å] Compressive	ΔMn-O [Å] Tensile
LMO	∓ 0.320	-0.318	$+0.351$
LCMO 0.125	∓ 0.315	-0.289	$+0.344$
LCMO 0.25	∓ 0.311	-0.268	$+0.328$
LCMO 0.375	∓ 0.308	-0.247	$+0.308$

7.2 Oxygen vacancy formation energies

There are many interesting features of the oxygen vacancy formation in LCMO. A displacement of oxygen anions towards the A-cation in the stoichiometric compound leads to more inequivalent oxygens in the mixed compounds than in the parent compounds LMO and CMO. A fundamentally different response to strain is also observed in LMO compared to CMO, and a different grouping of vacancy formation energies in LCMO depending on whether compressive or tensile strain is applied.

7.2.1 Vacancy formation energies

As discussed in section 3.2.2, the oxygen non-stoichiometry is very different from LMO than CMO. For LMO, there is a tendency towards oxygen hyperstoichiometry due to cation deficiency, while for CMO there is a tendency towards oxygen deficiency. The vacancy formation energies for LMO have been reported to be 4.29 ± 0.66 eV [46], and 1.89 ± 0.04 eV for CMO [45]. The formation energy for LMO is in this work calculated to be 3.95 eV, in excellent accord with the

findings of Nowotny. The average vacancy formation for unstrained LCMO 0.25 is 3.04 eV and 2.83 eV for LCMO 0.375, consistent with the expectation that the vacancy formation energies lowers until a plateau is reached at x ~0.4, and falls again closer to pure CMO [44].

7.2.2   Displacement of oxygen anions

For all compounds, the oxygen anions were found to be displaced towards one of the cations in the square planar coordination of (La,Ca). This displacement was quantified with a displacement index, defined by equation 5.3. The average displacement was found to be 1 for oxygens with in-plane Mn-O-bonds, and slightly above 1 for oxygens with out-of-plane Mn-O-bonds. However, the individual oxygen anions are found to be displaced quite a lot. Due to this, and that the displacements also occur in unsubstituted LMO and for the oxygen anions only coordinated by La in LCMO 0.125, the effect is not chemical in nature. If it was, one would expect a general tendency of displacement towards one type of cation and no displacement in pure LMO.

The displacement also changes with strain, and this is coupled with the change of octahedral tilt and rotation. The average displacement index does not change with strain either, but the absolute value of the displacement does increase with tensile strain. This is consistent with larger values of both octahedral tilt and rotation in this regime. As the displacement of in-plane oxygens is sensitive to changes in both rotation and tilt, it is generally hard to predict the increase or decrease of these displacements.

While the displacements seems to be unaffected by the chemical nature of the cation, the displacement has a large effect on the vacancy formation energy.

7.2.3 Strain response of oxygen vacancies

From arguments of chemical expansion, it is expected that the oxygen vacancies are stabilized by tensile strain and destabilized by compressive strain. This behavior is however counteracted by other effects, making the picture a lot more complicated. In this work, LMO is found to have a strain response fundamentally different from what can be expected from simple chemical expansion arguments, and also from what is seen in CMO [16]. LCMO exhibits changes that more resemble what is found in CMO, though there are fundamental differences here as well. In addition, it is found an interesting effect of the oxygen displacement on the formation energies that is very different in the compressive and tensile regimes.

LCMO 0.125 is not considered in this part of the discussion, due to the large deviation of formation energies for this composition, that is believed to be induced by the high values of the Hubbard U-correction.

LMO

For LMO, a complete reversal of this behavior is seen for the in-plane oxygen vacancies. These vacancies are instead insensitive to tensile strain, but are stabilized by compressive strain. As there is a correlation between the value of strain and the Jahn-Teller-distortion of the MnO_6-octahedra, it can be hypoth-

esized that the increasing distortion destabilizes the vacancies. The destabilization of the in-plane vacancy by Jahn-Teller distortion is supported by the relatively large difference of ~0.17 eV between the in-plane and out-of-plane vacancy without strain. This is not surprising, as there is considerable orbital ordering in the ab-plane, in which the broken Mn-O-Mn-bonds lie. This could explain the stabilization in the compressive regime, where the distortion is lower. The formation energy is close to the formation energy for out-of-plane vacancies with no strain. At the same time it could explain why there is no observed change with tensile strain, as the expected stabilization associated with chemical expansion is counteracted by the more distorted octahedra.

For out-of-plane vacancies, there is a continuous stabilization of the vacancies with increasing strain. This behavior is what can be expected from simple chemical expansion arguments.

LCMO 0.25 and LCMO 0.375

In LCMO 0.25 and LCMO 0.375, the most interesting trend is the different grouping of oxygen vacancies for compressive and tensile strain. In the compressive region, the vacancies form with three distinct energies, depending solely on the type of vacancy. The out-of-plane vacancies are more unstable than the in-plane vacancies. For LCMO 0.375, the in-plane vacancies coordinated by 2 La and 2 Ca are further stabilized. For tensile strain, the vacancies are no longer grouped by type of vacancy, but by the displacement.

The out-of-plane vacancies behave the same way as they do in LMO, being desta-

bilized by compressive strain and stabilized by tensile. The in-plane vacancies behave more like what is seen in CMO, though there are some differences. Compressive strain tends to stabilize the in-plane vacancies slightly.

7.2.4   Effect of displacement and coordination on oxygen vacancy formation

The displacement of the oxygen anions towards one of the cations in the square planar configurations has a significant impact on the vacancy formation energies in the tensile regime. Anions more displaced towards La are higher in energy by ~0.2 - 0.3 eV for both LCMO 0.25 and LCMO 0.375. The in-plane vacancies in LCMO 0.375 that are coordinated by two Ca instead of only one, are also stabilized by ~0.15 eV relative to the other vacancies with the same type of displacement. This suggests that the bonding between La^{3+} and O^{2-} is stronger than between Ca^{2+} and O^{2-}, consistent with the higher formation energies in LMO compared to CMO. As the differences in radii (1.36 Å for La^{3+} and 1.34 Å for Ca^{2+} [75]) and electronegativity (1.1 for La^{3+} and 1.0 for Ca^{2+}) are small, the difference in formation energies can be expected from electrostatic arguments, due to the difference in formal charge.

7.2.5   Exploiting strain response of oxygen vacancy formation for novel device design

Such a distinct difference in vacancy preference in the compressive and tensile regimes, suggest that it could be possible to tune the vacancy concentrations with strain. Vacancy ordering effects can be induced with compressive

strain, and the equilibrium vacancy concentration could be controlled by varying the magnitude of strain. In the tensile regime, one can expect higher oxygen vacancy concentrations in the vicinity of Ca-ions. Combined with the experimental findings of a tendency towards cation segregation in mixed-valence manganites [76], the possibility of designing thin films with an oxygen vacancy concentration gradient opens up. This could potentially be exploited in next-generation device design.

7.3   Computational Challenges

The modelling of LCMO has proven to be non-trivial, which mainly can be attributed to the strong electron correlation, the d^4-electron configuration of Mn^{3+} which leads to anisotropic octahedral distortion, and to the phenomena of nanoscale phase separation in these materials, that is not captured in plane-wave DFT.

7.3.1   Hubbard U

The strong electron correlation is poorly described by DFT, and must be corrected for by the addition of an on-site Coulomb repulsion and exchange interaction. In an ideal case, the same value of this correction could be used for all compositions, but the extensive testing of these parameters reported in section 5.7 showed that this was not possible.

This can mainly be attributed to the anisotropic effect the exchange parameter, J, has on the Jahn-Teller-distorted structures. In the widely adopted correction

scheme developed by Dudarev, the Coulombic and exchange terms are both included in one effective parameter, $U_{\text{eff}} = U - J$. This is shown not to work in describing LMO in an extensive study by Mellan, as the effect of the exchange is highly dependent on the polarization of occupancies in the e_g-orbitals [59]. This resulted in either underestimated band gaps for low values of U_{eff} or stabilization of the wrong magnetic ground state for higher values. Their work concluded that it was optimal to use the method developed by Liechtenstein instead, where the exchange term is explicitly included, with values $U = 8$ and $J = 1.9$ eV.

The same parameters were used to test the other compositions, but found to fail to describe the magnetic ordering correctly for LCMO 0.25 and LCMO 0.375, while for LCMO 0.125 there was no band gap present. The latter can however be attributed to phase separation, discussed below.

Instead, the Dudarev-scheme had to be used to describe the ferromagnetic metallic compositions LCMO 0.25 and LCMO 0.375. This variation of parameters across compositions makes direct comparisons between them much more dubious.

7.3.2   Phase separation

The failure to properly describe LCMO 0.125 could be due to the non-existence of a homogeneous insulating ferromagnetic phase. Several researches have reported strong evidence for phase separation in this compositional regime. When using a 2x2x2 supercell with periodic boundary conditions, it is assumed that

the phase is homogeneous. In the case when it is not homogeneous, the real physics of the material cannot be captured, and the resulting simulated structure will not be able to explain experimental values. The structural parameters were however adequately described.

It is also experimentally observed that tensile strain induces an insulating phase in compounds of LCMO in the FM-M region [39, 38]. A small band gap was produced in the tensile regime for LCMO 0.25 for a Hubbard U-value of $U = 3$, though a higher value, with which there was no band gap present, was chosen to isolate the effect of strain.

7.4 Further work

7.4.1 Density of states and charge compensation analysis

In order to further investigate the effects strain has on the vacancy formation energies, it can be fruitful to do a thorough analysis of the changes in density of states induced by introducing vacancies. This could help elucidate the effects of changes in the crystal field on the vacancy formations. In addition, a full analysis of charge compensation using Bader charge analysis can be performed. In Bader charge analysis, an electron density minimum around each ion is found in order to more accurately ascribe a correct charge for each ion.

7.4.2 Disorder simulation using the Virtual Crystal Approximation

As discussed in 5.1.1, the structures used have had a fixed ordering of the substituted cations. There are many ways the substituted cations can order, and the assumption that there is any ordering at all is not substantiated, and according to the theory of semicovalence it is assumed to be fully disordered in the FM-M phase [21]. Explicitly treating disorder is however extremely resource demanding, but using the Virtual Crystal Approximation (VCA) is one possibility to treat it. The idea was initially discarded, as it was thought that treating two atoms of different formal charge would not be possible, but other studies have used this approximation to simulate the very similar compound $La_{1-x}Sr_xMnO_3$, though using different software than VASP [77, 78]. To the author's knowledge, VCA has not been applied to these compounds using VASP.

7.4.3 Strain application in the (111)-plane

This work is limited to strain applied in the (001)-plane. While there is still much to be understood of the strain response for this orientation, further studies can be performed by applying strain in the (111)-plane. As the strain response shown in this work is very sensitive to the directions of the Mn-O-Mn-bonds and to orbital order, different strain response can be expected for strain in this plane. In (001), two axes are parallel to the biaxial strain, while one is perpendicular. For strain applied in the (111)-plane, there are no axes that are parallel or perpendicular, and the strain response can be expected to be quite different.

7.4.4   Cation vacancies

Aschauer *et al.* hypothesized that cation vacancies in LMO under compressive strain would show a similar response as oxygen vacancies shows in CMO under tensile strain [16]. This is not necessarily quite as simple, due to the effects of Jahn-Teller distortion in LMO. Especially vacancies of the Jahn-Teller active Mn^{3+}-ions could be expected to show a complex behavior depending on strain, as the magnitude of the distortion has been shown to be highly dependent on the strain. The cation vacancies are also more readily formed in pure LMO than oxygen vacancies, so this should indeed be further investigated.

Chapter 8

Conclusion

In this work, first-principles calculations were performed to investigate the effects of biaxial epitaxial strain on oxygen vacancy formation in different composition of $La_{1-x}Ca_xMnO_3$ ($x = 0, 0.125, 0.25$ and 0.375). Calculations on the bulk phase was first performed, followed by simulation of both compressive and tensile strain for the stoichiometric and the oxygen deficient cells. Inequivalent oxygen anions were removed based on in-plane or out-of-plane orientation relative to the biaxial strain, and based on oxygen anion displacement.

In order to describe the vacancy formations, a model system was developed by tweaking parameters to reproduce experimental results. It was found that the same values of the Hubbard-like on-site repulsion could not be used to describe all compositions. This is attributed to the anisotropic effect of the exchange parameter J induced by Jahn-Teller distortion of the MnO_6-octahedra. Difficulties in describing the composition $x = 0.125$ were also encountered, which is likely due to that the insulating ferromagnetic phase observed experimentally is the result of a nanoscale phase separation, and cannot be properly described with

a small supercell within plane-wave DFT, as the use of periodic boundary conditions assumes a homogeneous phase.

The structural response of the stoichiometric cells were found to be consistent with predictions, with the notable exception of the rotation angles of the MnO_6-octahedra in the *ab*-plane. The rotation angles showed a counterintuitive increase with tensile strain. This has been rationalized with a strain induced Jahn-Teller distortion of the MnO_6-octahedra, leading to a greater increase of in-plane bond lengths than the increase of the in-plane lattice parameters, such that the octahedral rotation increases to accommodate the increase in bond lengths rather than decrease to accommodate the tensile strain. The induced Jahn-Teller distortion is consistent with experimental findings in the literature.

The oxygen vacancy formation energies were found to be consistent with the literature, with the exception of $x = 0.125$. This is attributed to the failure of the model system. The high formation energies of pure $LaMnO_3$ are consistent with the tendency towards oxygen hyperstoichiometry and difference in formal charge, and the decrease in formation energy with higher Ca-content is expected.

A displacement of oxygen anions towards one of the A-cations in the square planar configuration was found for all compositions. The displacement has been quantified by a displacement index, Z, where 1 is defined as no net displacement towards the surrounding cations. The average displacement index is close to 1, meaning there is no preference towards either cation, and the displace-

ment is thus not effected by the type of cation. The displacement is related to the changes in octahedral rotation and tilt, and thus changes with strain. The total average displacement is largely unaffected by strain.

The strain induced changes in vacancy formation is fundamentally different from what is observed in $CaMnO_3$ ($x = 1$) [16]. For pure $LaMnO_3$, a stabilization of the in-plane vacancies is seen for compressive strain values, while the formation energy is insensitive to tensile strain. The out-of-plane vacancies are destabilized by compressive strain and stabilized by tensile. For intermediate compounds ($x = 0.25$ and 0.375), the behavior of the in-plane vacancies follows the same trend as $CaMnO_3$, while the out-of-plane vacancies are more $LaMnO_3$-like in nature.

The effect of oxygen displacement is found to be different for compressive strain than for tensile strain (for $x = 0.25$ and $x = 0.375$). In the compressive regime, the formation energies group according to the type of vacancy (in-plane or out-of-plane). For unstrained and tensilely strained structures, the formation energies are grouped by the oxygen displacement. Oxygen vacancies more displaced towards Ca are found to be more stable in this regime, and a higher actual coordination of Ca is also seen to stabilize the formation energies across all values of strain.

The interesting strain response of oxygen vacancies opens up possibilities to take advantage of epitaxial strain in designing novel next-generation devices in the future. The stabilization of vacancies in the vicinity of Ca-ions, combined with observed cation segregation [76], means it could be possible to create oxy-

gen vacancy concentration gradients in thin films of $La_{1-x}Ca_xMnO_3$ and similar materials.

Bibliography

[1] G. Kresse and J. Hafner. Ab initio molecular dynamics for liquid metals. *Physical Review B*, 47(1):558–561, 1993.

[2] G. Kresse and J. Hafner. Ab initio molecular-dynamics simulation of the liquid-metal–amorphous-semiconductor transition in germanium. *Physical Review B*, 49(20):14251–14269, 1994.

[3] G. Kresse and J. Furthmüller. Efficiency of ab-initio total energy calculations for metals and semiconductors using a plane-wave basis set. *Computational Materials Science*, 6(1):15–50, 1996.

[4] G. Kresse and J. Furthmüller. Efficient iterative schemes for ab initio total-energy calculations using a plane-wave basis set. *Physical Review B*, 54(16):11169–11186, 1996.

[5] K. Momma and F. Izumi. VESTA 3 for three-dimensional visualization of crystal, volumetric and morphology data. *Journal of Applied Crystallography*, 44(6):1272–1276, oct 2011.

[6] J. M. Rondinelli and N. A. Spaldin. Structure and properties of functional

oxide thin films: Insights from electronic-structure calculations. *Advanced Materials*, 23(30):3363–3381, 2011.

[7] J. H. Van Santen and G. H. Jonker. Ferromagnetic compounds of manganese with perovskite structure. *Physica*, 16(7-8):599–600, 1950.

[8] J. H. Van Santen and G. H. Jonker. Electrical conductivity of ferromagnetic compounds of manganese with perovskite structure. *Physica*, 16(7-8):599–600, 1950.

[9] S. Jin, T. H. Tiefel, M. McCormack, R. A. Fastnacht, R. Ramesh, and L. H. Chen. Thousandfold change in resistivity in magnetoresistive La-Ca-Mn-O films. *Science (New York, N.Y.)*, 264(5157):413–415, 1994.

[10] S. A. Wolf, D. D. Awschalom, R. A. Buhrman, J. M. Daughton, S. von Molnár, L. Roukes, A. Y. Chtchelkanova, and D. M. Treger. Spintronics : A Spin-Based Electronics Vision for the Future. 294(5546):1488–1495, 2001.

[11] S. V. Kalinin and N. A. Spaldin. Functional Ion Defects in Transition Metal Oxides. *Science*, 341(6148):858–859, 2013.

[12] A. Ourmazd and J. C. H. Spence. Detection of oxygen ordering in superconducting cuprates. *Nature*, 329:425–427, 1987.

[13] D. J. Werder, C. H. Chen, R. J. Cava, and B. Batlogg. Oxygen-vacancy ordering and microstructure in annealed $Ba_2YCu_3O_{7-\delta}$. *Physical Review B*, 38(7):5130–5133, 1988.

[14] C. Sun, R. Hui, and J. Roller. Cathode materials for solid oxide fuel cells: A review. *Journal of Solid State Electrochemistry*, 14(7):1125–1144, 2010.

[15] R. Ramamoorthy, P. K. Dutta, and S. A. Akbar. Oxygen sensors : Materials , methods , designs. *J. Mater. Sci.*, 38:4271–4282, 2003.

[16] U. Aschauer, R. Pfenninger, S. M. Selbach, T. Grande, and N. A. Spaldin. Strain-controlled oxygen vacancy formation and ordering in $CaMnO_3$. *Physical Review B - Condensed Matter and Materials Physics*, 88(5):1–7, 2013.

[17] C. Zener. Interaction between the d-shells in the transition metals. *Physical Review*, 81(3):440–444, 1951.

[18] C. Zener. Interaction between the d-shells in the transition metals. II. Ferromagnetic compounds of manganese with Perovskite structure. *Physical Review*, 82(3):403–405, 1951.

[19] J. Volger. Further experimental investigations on some ferromagnetic oxidic compounds of manganese with perovskite structure. *Physica*, 20(1):49–66, 1954.

[20] E. O. Wollan and W. C. Koehler. Neutron Diffraction Study of the Magnetic Properties of the Series of Perovskite-Type Compounds $[(1 − x)La, xCa]MnO_3$. *Physical Review*, 100(2):545–563, 1955.

[21] J. B. Goodenough. Theory of the role of covalence in the perovskite-type manganites $[La,M(II)]MnO_3$. *Physical Review*, 100(2):564–573, 1955.

[22] R. von Helmolt, J. Wecker, B. Holzapfel, L. Schultz, and K. Samwer. Giant negative magnetoresistance in perovskitelike $La_{2/3}Ba_{1/3}MnO_x$ ferromagnetic films. *Physical Review Letters*, 71(14):2331–2333, 1993.

[23] K. Chahara, T. Ohno, M. Kasai, and Y. Kozono. Magnetoresistance anti-ferromagnetic in magnetic manganese spin structure. *Appl. Phys. Lett.*, 63(14):1990–1992, 1993.

[24] H. A. Jahn and E. Teller. Stability of Polyatomic Molecules in Degenerate Electronic States. I. Orbital Degeneracy. *Proceedings of the Royal Society A: Mathematical, Physical and Engineering Sciences*, 161(905):220–235, 1937.

[25] E. Dagotto, T. Hotta, and A. Moreo. Colossal magnetoresistant materials: the key role of phase separation. *Physics Reports*, 344(1-3):1–153, 2001.

[26] S.-W. Cheong and H. Y. Hwang. Ferromagnetism vs. charge/orbital ordering in mixedvalent manganites. In Y. Tokura, editor, *Colossal Magnetoresistance Oxides*. Gordon & Breach, London, 1999.

[27] H. A. Kramers. L'interaction Entre les Atomes Magnétogènes dans un Cristal Paramagnétique. *Physica*, 1(1-6):182–192, 1934.

[28] P. W. Anderson and H. Hasegawa. Considerations on double exchange. *Physical Review*, 100(2):675–681, 1955.

[29] V. M. Goldschmidt. Die Gesetze der Krystallochemie. *Die Naturwissenschaften*, 14(21):477–485, 1926.

[30] A. P. Ramirez. Colossal magnetoresistance. *Journal of Physics: Condensed Matter*, 9(39):8171, 1997.

[31] C.N.R. Rao and R. Mahesh. Giant magnetoresistance in manganese oxides. *Current Opinion in Solid State and Materials Science*, 2(1):32–39, 1997.

[32] J. M. D. Coey, M. Viret, and S. von Molnár. Mixed-valence manganites. *Adv. Phys.*, 58(6):571–697, 2009.

[33] M. B. Salamon and M. Jaime. The physics of manganites: Structure and transport. *Reviews of Modern Physics*, 73(3):583–628, 2001.

[34] Y. Tokura. Critical features of colossal magnetoresistive manganites. *Reports on Progress in Physics*, 69(3):797–851, 2006.

[35] M. Fäth, S. Freisem, A. A. Menovsky, Y. Tomioka, J. Aarts, and J. A. Mydosh. Spatially Inhomogeneous Metal-Insulator Transition in Doped Manganites. *Science*, 285(5433):1540–1542, 1999.

[36] J. M. D. Coey, M. Viret, and S. von Molnár. Mixed-valence manganites - ten years on. *Adv. Phys.*, 58(6):567–569, 2009.

[37] R. J. D. Tilley. *Understanding Solids*. Chichester, 2nd edition, 2013.

[38] A. Llobet, L. Ranno, and J. Pierre. Tuning Magnetotransport and Magnetic Properties of $La_{2/3}Ca_{1/3}MnO_3$ Thin Films using Epitaxial Strain. *Materials Science Forum*, 373-376:517–520, 2001.

[39] M. Ziese, H. C. Semmelhack, and K. H. Han. Strain induced orbital ordering in thin $La_{0.7}Ca_{0.3}MnO_3$ films on $SrTiO_3$. *Physical Review B*, 68(14):134444, 2003.

[40] J. Dvorak, Y. U. Idzerda, S. B. Ogale, S. Shinde, T. Wu, T. Venkatesan, R. Godfrey, and R. Ramesh. Are strain-induced effects truly strain induced? A comprehensive study of strained LCMO thin films. *Journal of Applied Physics*, 97(10), 2005.

[41] S. V. Kalinin, A. Borisevich, and D. Fong. Beyond condensed matter physics on the nanoscale: The role of ionic and electrochemical phenomena in the physical functionalities of oxide materials. *ACS Nano*, 6(12):10423–10437, 2012.

[42] H. J. M. Bouwmeester. Dense ceramic membranes for methane conversion. *Catalysis Today*, 82(1-4):141–150, 2003.

[43] X. K. Wei, T. Zou, F. Wang, Q. H. Zhang, Y. Sun, L. Gu, A. Hirata, M. W. Chen, Y. Yao, C. Q. Jin, and R. C. Yu. Origin of ferromagnetism and oxygen-vacancy ordering induced cross-controlled magnetoelectric effects at room temperature. *Journal of Applied Physics*, 111(7):0–7, 2012.

[44] L. Rørmark, K. Wiik, S. Stølen, and T. Grande. Oxygen stoichiometry and structural properties of $La_{1-x}A_xMnO_{3\pm\delta}$ (A = Ca or Sr and $0 \leq x \leq 1$). *Journal of Materials Chemistry*, 12:1058–1067, 2002.

[45] L. Rørmark, A. B. Mørch, K. Wiik, and S. Stølen. Enthalpies of Oxidation of $CaMnO_{3-\delta}$, $Ca_2MnO_{4-\delta}$ and $SrMnO_{3-\delta}$ - Deduced Redox Properties. *Chemistry of Materials*, 13(15):4005–4013, 2001.

[46] J. Nowotny and M. Rekas. Defect Chemistry of $(La,Sr)MnO_3$. *J. Am. Ceram. Soc.*, 81(191914):67–80, 1998.

[47] S. B. Adler. Chemical Expansivity of Electrochemical Ceramics. *Journal of the American Ceramic Society*, 84(9):2117–2119, 2001.

[48] E. Schrödinger. Quantisierung als Eigenwertproblem. *Annalen der Physik*, 384(4):361–376, 1926.

[49] W. Kohn. Nobel Lecture : Electronic structure of matter — wave functions and density functionals. *Reviews of Modern Physics*, 71(5):1253–1266, 1999.

[50] P. Hohenberg and W. Kohn. Inhomogeneous Electron Gas. *Phys. Rev.*, 136(3B):B864–B871, 1964.

[51] D. S. Scholl and J. A. Steckel. *Density Functional Theory - A Practical Introduction.* John Wiley & Sons, Inc., Hoboken, New Jersey, 1st edition, 2009.

[52] M Born and R Oppenheimer. Zur Quantentheorie der Molekeln. *Annalen der Physik*, 20(84):457–484, 1927.

[53] W. Kohn and L. J. Sham. Self-Consistent Equations Including Exchange and Correlation Effects. *Physical Review B*, 140(1951), 1965.

[54] J. P. Perdew, A. Ruzsinszky, G. I. Csonka, O. A. Vydrov, G. E. Scuseria, L. A. Constantin, X. Zhou, and K. Burke. Restoring the Density-Gradient Expansion for Exchange in Solids and Surfaces. *Physical Review Letters*, 100(13):136406, 2008.

[55] F. Bloch. Über die Quantenmechanik der Elektronen in Kristallgittern. *Zeitschrift für Physik*, 52(7-8):555–600, 1929.

[56] P. E. Blöchl. Projector augmented-wave method. *Physical Review B*, 50(24):17953–17979, 1994.

[57] S. L. Dudarev, S. Y. Savrasov, C. J. Humphreys, and A. P. Sutton. Electron-energy-loss spectra and the structural stability of nickel oxide: An LSDA+U study. *Physical Review B*, 57(3):1505–1509, 1998.

[58] A. I. Liechtenstein, V. I. Anisimov, and J. Zaanen. Density-functional the-
ory and strong interactions: Orbital ordering in Mott-Hubbard insulators.
Physical Review B, 52(8):5467–5471, 1995.

[59] T. A. Mellan, F. Corà, R. Grau-Crespo, and S. Ismail-Beigi. Importance of
anisotropic Coulomb interaction in LaMnO$_3$. *Physical Review B - Con-
densed Matter and Materials Physics*, 92(8):085151, 2015.

[60] R. P. Feynman. Forces in molecules. *Physical Review*, 56(4):340–343, 1939.

[61] A. J. Cohen, P. Mori-Sánchez, and W. T. Yang. Insights into current limita-
tions of density functional theory. *Science*, 321(5890):792, 2008.

[62] G. Kresse. From ultrasoft pseudopotentials to the projector augmented-
wave method. *Physical Review B*, 59(3):1758–1775, 1999.

[63] M. Nord, P. E. Vullum, M. Moreau, J. E. Boschker, S. M. Selbach,
R. Holmestad, and T. Tybell. Structural phases driven by oxygen vacan-
cies at the La$_{0.7}$Sr$_{0.3}$MnO$_3$/SrTiO$_3$ hetero-interface. *Applied Physics Letters*,
106(4):041604, 2015.

[64] R. L. Johnson-Wilke, D. Marincel, S. Zhu, M. P. Warusawithana, A. Hatt,
J. Sayre, K. T. Delaney, R. Engel-Herbert, C. M. Schlepütz, J. W. Kim,
V. Gopalan, N. a. Spaldin, D. G. Schlom, P. J. Ryan, and S. Trolier-Mckinstry.
Quantification of octahedral rotations in strained LaAlO$_3$ films via syn-
chrotron x-ray diffraction. *Physical Review B - Condensed Matter and Ma-
terials Physics*, 88:1–8, 2013.

[65] J. Rodríguez-Carvajal, M. Hennion, F. Moussa, A. H. Moudden, L. Pinsard,

and A. Revcolevschi. Neutron-diffraction study of the Jahn-Teller transition in stoichiometric LaMnO$_3$. *Physical Review B*, 57(6):R3189–R3192, 1998.

[66] G. Kresse, M. Marsman, and J. Furthmüller. VASP the Manual - http://cms.mpi.univie.ac.at/vasp/vasp/vasp.html, 2016.

[67] G. Henkelman. VTST-scripts - http://theory.cm.utexas.edu/vtsttools/index.html.

[68] N. Sakai, H. Fjellvag, and B. Lebech. Effect of Non-Stoichometry on Properties of La$_{1-t}$MnO$_{3+\delta}$. Part II. Crystal Structure, 1997.

[69] T. Saitoh, A. E. Bocquet, T. Mizokawa, H. Namatame, A. Fujimori, M. Abbate, Y. Takeda, and M. Takano. Electronic structure of La$_{1-x}$Sr$_x$MnO$_3$ studied by photoemission and x-ray-absorption spectroscopy. *Physical Review B*, 51(20):13942–13951, 1995.

[70] T. Arima, Y. Tokura, and J. B. Torrance. Variation of optical gaps in perovskite-type 3d transition-metal oxides. *Physical Review B*, 48(23):17006–17009, 1993.

[71] J. H. Jung, K. H. Kim, D. J. Eom, T. W. Noh, E. J. Choi, J. Yu, Y. S. Kwon, and Y. Chung. Determination of electronic band structures of CaMnO$_3$ and LaMnO$_3$ using optical-conductivity analyses. *Physical Review B*, 55(23):15489–15493, 1997.

[72] R. Krüger, B. Schulz, S. Naler, R. Rauer, D. Budelmann, J. Bäckström, K. H. Kim, S. W. Cheong, V. Perebeinos, and M. Rübhausen. Orbital ordering in LaMnO$_3$ investigated by resonance raman spectroscopy. *Physical Review Letters*, 92(9):097203–1, 2004.

[73] Q. Huang, A. Santoro, J. W. Lynn, R. W. Erwin, J. A. Borchers, J. L. Peng, K. Ghosh, and R. L. Greene. Structure and magnetic order in $La_{1-x}Ca_xMnO_3$. *Physical Review B*, 58(5):2684–2691, 1998.

[74] B. Dabrowski, R. Dybzinski, Z. Bukowski, and O. Chmaissem. Oxygen Content and Structure of $La_{1-x}Ca_xMnO_{3+\delta}$ as a Function of Synthesis Conditions. *Journal of Solid State Chemistry*, 146:448–457, 1999.

[75] R. D. Shannon. Revised Effective Ionic Radii and Systematic Studies of Interatomie Distances in Halides and Chaleogenides. *Acta Crystallography*, A32:751–767, 1976.

[76] W. Lee, J. W. Han, Y. Chen, Z. Cai, and B. Yildiz. Cation size mismatch and charge interactions drive dopant segregation at the surfaces of manganite perovskites. *Journal of the American Chemical Society*, 135(21):7909–7925, 2013.

[77] Z. Fang and K. Terakura. Surface Magnetic Phase Diagram of Tetragonal Manganites. *Journal of the Physical Society of Japan*, 70(11):3356–3361, 2001.

[78] H. Chen and S. Ismail-Beigi. Ferroelectric control of magnetization in $La_{1-x}Sr_xMnO_3$ manganites: A first-principles study. *Physical Review B - Condensed Matter and Materials Physics*, 86(2):1–13, 2012.

Appendix A

Acronyms

AFM Antiferromagnetic

CAFM Canted antiferromagnetic

CMO $CaMnO_3$

CMR Colossal Magnetoresistance

DFT Density Functional Theory

FM Ferromagnetic

FM-I Ferromagnetic insulator

FM-M Ferromagnetic metal

GGA Generalized Gradient Approximation

GMR Giant Magnetoresistance

IP V_O In-plane oxygen vacancy

LAO $LaAlO_3$

LCAO Linearilized Combination of Atomic Orbitals

LCMO $La_{1-x}Ca_xMnO_3$

LCMO 0.125 $La_{0.875}Ca_{0.125}MnO_3$

LCMO 0.25 $La_{0.75}Ca_{0.25}MnO_3$

LCMO 0.375 $La_{0.625}Ca_{0.375}MnO_3$

LMO $LaMnO_3$

LSMO $La_{1-x}Ca_xMnO_3$

L(S)DA Local (Spin) Density Approximation

NGO $NdGaO_3$

OP V_O Out-of-plane oxygen vacancy

PM-I Paramagnetic insulator

STO $SrTiO_3$

VASP Vienna ab initio Simulation Package

X-AFM X-type antiferromagnetic (X = A, G, C, E, CE)

Appendix B

VASP

B.1 Input files

B.1.1 INCAR

Below a typical INCAR-file is given. The MAGMOM-tag is changed depending on which magnetic ordering is induced. The value corresponds to the magnitude of the magnetic moment, and a minus sign would indicate an antiparallel magnetic moment on the specified ion. The order of magnetic moment corresponds to the ions as they are specified in the POSCAR-file. The LDAUTYPE is in this example set to 2, which specifies the method by Dudarev. A value of 1 would set it to the method of Liechtenstein instead. The LDAUU and LDAUJ specifies the values of U (U_{eff} for Dudarev) and J respectively, and the values corresponds to the Hubbard U-correction in eV. The order of the corrections are set according to atom type, as the order is specified in the POSCAR-file.

Listing B.1: INCAR-file

```
system    = LCMO 0.25 (FM)


% Cut-off energy
PREC       =  Normal
ENCUT      =  550


% Convergence criteria
NSW        =  50
NELMIN     =  4
NELM       =  120
EDIFFG     = -0.01
EDIFF      =  1E-06


% Relaxation
ISIF       =  3
IBRION     =  2



% Input and output-files
ICHARG     = 0
LCHARG     = .FALSE.
LORBIT     =  11



% Spin polarization
ISPIN      =  2
MAGMOM     =  8*0 4 4 4 4 4 4 4 4 24*0


% Hubbard U-correction
LDAU       =  .TRUE.
LDAUTYPE   =  2
LDAUL      =  3 -1 2 -1
LDAUU      =  10 0 4 0
LDAUJ      =  0 0 0 0
```

```
LDAUPRINT =   2



% Calculation parameters
GGA        =   PS
LREAL      =   .FALSE.


ISMEAR     =   0
SIGMA      =   0.01


LASPH      =  .TRUE.
LMAXMIX    =   4


NPAR       =   4
NSIM       =   4
```

B.1.2 KPOINTS

The KPOINTS-file used for relaxation is given below. The number of k-points is increased for density of states-calculations.

Listing B.2: KPOINTS-file

```
Automatic mesh
0
Gamma
4   4   4
0   0   0
```

B.1.3 POSCAR

A typical POSCAR-file used in this work. The first line specifies the name of the structure, and is not used by VASP. The second line contains a scaling factor, and

the following three lines specifies the lattice vectors *a*, *b* and *c* in Cartesian coordinates. The lines below specifies the number of each atom. Note that the type of atom is determined by the POTCAR-file, and the names in this file is only for the researchers own convenience. The order of the atoms must be the same as in the POTCAR-file for this reason. The next line specifies that the atom positions are given in fractional coordinates of the lattice vectors, and the following lines specifies each atom position. This continues until the positions of all atoms in the supercell is stated.

Listing B.3: POSCAR-file

```
(La,Ca)MnO3
1.0
       7.7679867744        0.0000000000        0.0000000000
       0.0000000000        7.7679901123        0.0000000000
       0.0000000000        0.0000000000        7.7122240067
   La   Ca   Mn    O
    6    2    8   24
Direct
    0.996286988        0.509387016        0.000000000
    0.491824001        0.009176000        0.000000000
    0.980910003        0.486667991        0.500000000
```

B.1.4 POTCAR

The POTCAR-file is constructed from individual pseudopotential files, concatenated into one single file. The order of the files must correspond to the order of the files given in the POSCAR-file. These pseudopotentials are available from a vast library included with the VASP-software. The pseudopotentials used in this work are the *PAW_PBE La* (06Sep2000), *PAW_PBE Ca_sv* (06Sep2000), *PAW_PBE*

Mn_sv (23Jul2007) and *PAW_PBE O* (08Apr2002). Information in the file includes mass and valence, among other atom specific quantities.

B.1.5   Job script

In order to submit the calculations to Abel, the supercomputer cluster at the University of Oslo, a job script must be executed. This is given below. In this file, the amount of time, number of nodes and cores requested for the specific calculation, and the version of VASP to be used is specified. In this work vasp-5.3.3bfix (for strain calculations) and vasp-5.3.5-noshear (for bulk relaxation) has been used.

```
        #!/bin/sh
## Jobname
#SBATCH --job-name=Name of job
## Project
#SBATCH --account=nn9264k
## Walltime
#SBATCH --time=16:00:00
## Memory needed
#SBATCH --mem-per-cpu=3920M

## Number of tasks (cores):
#SBATCH --nodes=1
#SBATCH --ntasks-per-node=16
##SBATCH --constraint=amd
##SBATCH --constraint=ib
##SBATCH --tmp=2G

## Set up job environment
source /cluster/bin/jobsetup
module load vasp/5.3.3bfix/
```

```
#module load openmpi.intel/1.7.3


## Set up input and output files
infile="INCAR KPOINTS POSCAR POTCAR"
outfile="CHG CHGCAR CONTCAR DOSCAR EIGENVAL IBZKPT OSZICAR OUTCAR* PCDAT
    WAVECAR XDATCAR vasprun.xml POSCAR* progress* repeat*"
cp $infile $SCRATCH
chkfile $outfile


## Run command
cd $SCRATCH


mpirun /usit/abel/u1/moreau/vasp-abfix/vasp.5.3.3/vasp-abfix
cp -r $SCRATCH/* $SUBMITDIR


## end of script
```

B.2   Density of states-calculations

For density of states-calculations, certain changes are made in the INCAR- and
KPOINTS-files. First a static self-consistent run is done to generate a charge
density (CHGCAR) that is used in a non-self consistent run to calculate the den-
sity of states. The changes are listed below, and the parameters that are un-
changed from the relaxations are omitted for clarity.

Listing B.4: INCAR-file for the static self-consistent run during density of states-calculations.

```
system   = LCMO 0.25 (FM)


% Convergence criteria
NSW       =   0
```

```
% Relaxation
ISIF        =   -1



% Input  and  output-files
LCHARG     = .TRUE.
LORBIT     =   11
```

Listing B.5: INCAR-file for the non self-consistent run during density of states-calculations.

```
system   = LCMO 0.25 (FM)

% Convergence criteria
NSW        =   0
EDIFF      =   1E-08

% Relaxation
ISIF        =   -1



% Input  and  output-files
ICHARG     = 11
LCHARG     = .TRUE.
LORBIT     =   11


EMIN = -2
EMAX = 18
NEDOS = 401
```

Listing B.6: KPOINTS-file for the non self-consistent run during density of states-calculations.

```
Automatic mesh
0
Gamma
8   8   8
0   0   0
```